Annual Report
2017

HI JENA
HELMHOLTZ
Helmholtz Institute Jena

Helmholtz Institute Jena
Fröbelstieg 3
07743 Jena
www.hi-jena.de

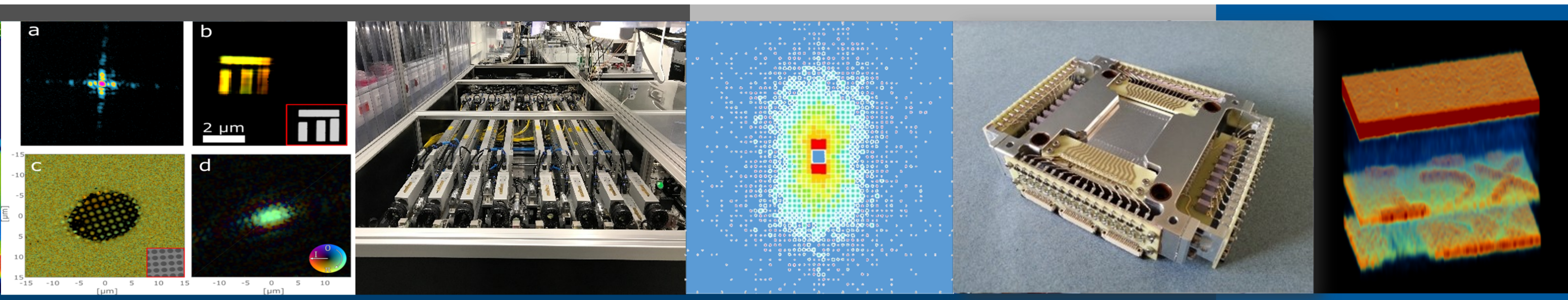

seit 1558

GSI

HZDR
HELMHOLTZ
ZENTRUM DRESDEN
ROSSENDORF

DESY.

Helmholtz Institute Jena

Annual Report 2017

Imprint

Publisher: Helmholtz-Institut Jena, Fröbelstieg 3, 07743 Jena, Germany
(`http://www.hi-jena.de`)
@ GSI Helmholtzzentrum für Schwerionenforschung GmbH
Darmstadt, Germany (`http://www.gsi.de`)
GSI is member of the Helmholtz association of national research centers (`http://www.helmholtz.de`).

Editors: Marc M. Günther and Andrey Volotka

DOI: 10.15120/GSI-2018-00628 (`http://dx.doi.org/10.15120/GSI-2018-00628`)

Publication date: June 2018

Contents

Foreword

Laser Particle Acceleration 27

Foreword

The Helmholtz Institute Jena (HI-Jena) was founded in 2009 as a branch of the GSI Helmholtz Center for Heavy Ion Research on the campus of the Friedrich-Schiller-University (FSU) in Jena. The institute combines established scientific expertise of the FSU with the strategic mission of the GSI and the Helmholtz Association. The HI-Jena has the added value of close and easy access to students and, hence, it strongly supports the education of the next generation of researchers for the future Facility for Antiproton and Ion Research (FAIR). The aim of the HI-Jena is excellence in fundamental and applied research, in particular, research on the structure of matter based on high-power lasers, accelerated particles (ions and electrons), and x-ray science embedded within the programs "From Matter to Materials and Life" (MML) and "Matter and Technologies" (MT) of the Helmholtz Research Field "Matter". Emphasis is placed in investigating the interface of particle accelerators and lasers for harvesting well established and yet to discovered synergies. The institute operates two high-power laser systems as major research infrastructures: the fully-diode pumped laser system POLARIS as well as the Titanium Sapphire laser system JETI. The expertise of the HI-Jena is particularly valuable for planning and developing research in the realm of extreme electromagnetic fields at the international FAIR project and also at the European X-ray Free-electron Laser (XFEL) facility.

The Annual Report for 2017 documents excellence of the institute here in Jena and its ongoing scientific progress. In particular, it has been demonstrated that for broad bandwidth few-cycle light pulses the optical phase behaves very different from the well-known and commonly used Gouy phase [*Nature Physics* **13**, 947 (2017)]. From these findings, conclusions can be drawn about how to manipulate the focal phase in order to steer and control the ultrafast interactions between light and matter and will make it possible to control electron dynamics and chemical reactions by facilitating novel spatial phase distributions [*Journal of Optics* **19**, 124007 (2017)]. These insights into fundamental physics will further advance the development of new radiation sources and the field of light wave electronics. Another example is the development of highly accurate sensors for non-contact measuring of tiniest currents. Researchers of the Helmholtz Institute together with the Friedrich-Schiller-University have completed a new cryogenic current comparator with extended dimensions, which is required for the FAIR experiments. Measurements show that the sensor white noise is below 3 pA / $\sqrt{\mathrm{Hz}}$ and, therefore, singular pulses of 1 nA are traceable [*IEEE Transactions on Applied Superconductivity* **28**, 1 (2018)]. Consequently, the required parameters are realized for the unique cryogenic current comparator dimensions.

Furthermore, the HI-Jena is now a member of the newly established Max Planck School of Photonics (MPSP), an excellence network for photonic science. Starting from 2018 the German Federal Ministry of Education and Research supports a total of three Max Planck Schools for the upcoming five years. The nationwide networks are supposed to strengthen and bundle the competences and expertise of a science research field. Following this mission, the MPSP focuses on investigations in the field of photonics, for example attosecond physics or quantum optics. Within these research schools, scientists and students from institutes of the four large German research organizations and seven universities will collaborate and study in an interdisciplinary environment.

Much of the effort in 2017 was focused, however, on the Center Evaluation of the Helmholtz Association and the scientific achievements and performance during the last years. This evaluation took place in November 2017, for which the HI-Jena teamed up with the research divisions of atomic physics, plasma physics, and materials research of GSI Campus Darmstadt, forming one common research unit and with a dedicated on-site visit of the Institute by the referee board. Indeed, the scientific performance during the last years was evaluated as outstanding, a great success for the institute that played a prominent role in the overall evaluation process since the Campus GSI at Darmstadt was exempted from POF (due to its strong focus on the construction of FAIR). This success will help strengthen the mission of the institute and will lead to new exciting results as we report here for the last year.

News from the Research School of Advanced Photon Science of the Helmholtz Institute Jena

R. Märtin[1]*, Ch. Spielmann*[1,2] *, G. Weber*[1]*, and Th. Stöhlker*[1,2,3]

[1]HI-Jena, Jena, Germany; [2]University Jena, Jena, Germany; [3]GSI, Darmstadt, Germany

The Research School of Advanced Photon Science of the Helmholtz Institute Jena exists since 2012 and provides a structured PhD program for young scientists working at the institute in Jena and/or at the associated Helmholtz centres (GSI/FAIR, DESY and HZDR). Over recent years the number of doctoral students supported by RS-APS steadily increased up to 47 students in the year 2017. This great success can be mainly attributed to large number of PhD students which are third party funded. At the same time the RS-APS supports a maximum of 25 students financially via scholarships or working contracts. Moreover, RS-APS provides additional financial support for e.g. travel or events for all doctoral candidates. In 2017 about half of the number of students took advantage of the annual travel budget provided by the RS-APS. This money is foreseen to finance the travel to international conferences and workshops in order to present their own research results.

It is also to note that the HI Jena established an enhanced exchange of students and researchers with China. In 2017 two new PhD students from the Chinese Scholarship Council (CSC) program started their research activities at the Helmholtz Institute Jena. RS-APS provides for these exchange students an additional scholarship on top to the CSC rates to cover tuition fees and other costs. For the upcoming year already new students from China hand in their applications for the CSC program in order to join the Helmholtz Institute Jena for their PhD study.

In collaboration with the FSU Jena and the Helmholtz Graduate School for Hadron and Ion Research (HGS-HIRe) the graduate school RS-APS offers doctoral training activities, such as lecture weeks and soft skill courses as well as travel grants to its members.

Moreover the RS-APS organizes once a year its own Lecture Week addressing a scientific topic of the research scope of the Helmholtz Institute Jena. This event is always a good opportunity to get to know other research activities belonging to the HI Jena and to get in contact to students from other working groups of the institute.

In 2017 the fifth joint Lecture Week of HGS-HIRe and RS-APS was held at “Seminarhaus Lieb`Lommerke” in Willingen from September 17 to September 22 this year. This year topic was “Laser-Particle Acceleration for Basic Research and Ion Therapy” presented by the lecturers Malte Kaluza (University Jena), Sergey Rykovanov (HI Jena) and Michael Scholz (GSI). The Lecture Week was completed by a lecture (Claude Krantz/University Heidelberg) at the Marburg Ion Therapy Center MIT and a guided tour of the therapy accelerator facility (Uwe Scheeler/ University Heidelberg).

Finally it is worth to mentioning that in 2017 seven members of the Graduate School successfully completed their doctoral studies.

Figure 1: Group picture of the participants of the fifth joint Lecture Week of HGS-HIRe and RS-APS in Willingen.

High Power Laser Development

POLARIS - current status and experimental results

S. Keppler[1,2]*, M. Hornung*[1,2]*, G. A. Becker*[2]*, I. Tamer*[1,2]*, A. Massinger*[2]*, F. Irshad*[2]*, M. Hellwing*[2]*,*
F. Schorcht[1]*, A. Kessler*[1]*, J. Hein*[1,2]*, and M. C. Kaluza*[1,2]

[1]Helmholtz-Institute Jena, Germany; [2]Institute of Optics and Quantum Electronics, Jena, Germany

Over the last years, the performance of the POLARIS laser system has been continuously increased up to a maximum laser energy of $E_\mathrm{L} = 54$ J, where the maximum on-target energy is currently limited to 16,9 J by the size of the final compressor gratings. The pulse duration was successfully shortened down to $t_\mathrm{L} = 98$ fs by an optimization of the spectral bandwidth, which leads to a current maximum intensity of $3.5 \times 10^{20}\ \mathrm{W/cm^2}$ on target available for experiments [1]. In addition, we have made extensive efforts to optimize the temporal intensity contrast with regard to intensive prepulses.

During the last year, we have performed several experimental campaigns on order to investigate the influence of the temporal intensity contrast on the acceleration process of protons under different laser pulse conditions. First, we characterized in a four-month campaign the influence of artificial short prepulses with different intensity levels and time delays with respect to the main pulse. Here, we reached an increase of the maximum proton energy up to a factor of 2 under optimized prepulse conditions. The results are discussed separately within the annual report of Georg A. Becker.

Furthermore, we have determined the current laser performance in a benchmark experiment, in which protons are accelerated in the so-called Target-Normal-Sheath-Acceleration (TNSA) regime. To compare the results with those obtained during an earlier laser status, we irradiated 6.5 µm thick aluminium foils under 20° with p-polarized laser pulses, which is a standard experimental configuration and has been repeatedly tested during laser development. Here, we reached a maximum proton energy of 24 MeV, which is almost twice that of previous experiments (see HI-Jena annual report 2012). Thus, the performance improvement of POLARIS with regard to its energy, pulse duration and the temporal intensity contrast could also be demonstrated in proton experiments.

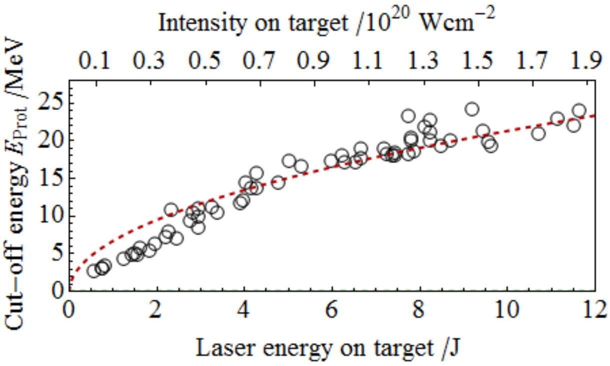

Figure 1: Energy scaling of the maximum proton cut-off energy of a 6,5 µm thick aluminium foil irradiated at 20° with p-polarized laser pulses. The proton spectra were recorded using a Thomson parabola aligned in target-normal direction. The red dashed line shows a root-shaped scaling as expected in TNSA-experiments [2].

In spite of the contrast optimizations with regard to intensive prepulses, the temporal slope of the main pulse itself prevents the experimental use of ultra-thin targets up to the ~10 nm range. Electrons, which are accelerated in the preplasma by the rising slope, propagate through the target and lead to a plasma expansion on the back side prior to the acceleration process, which counteracts the proton acceleration via the TNSA-process. In order to facilitate the use of ultra-thin targets, a plasma mirror (PM) was developed for the use within the POLARIS laser system. The PM consists of a f/7 focusing parabola with an off-axis angle of 6°. Near the focus, an anti-reflective coated substrate with a residual reflectivity of 0.06% is positioned. After the plasma reflection, the laser pulse is first re-collimated then and redirected to the final f/3 focusing parabola. The PM provides a maximum reflectivity of $R > 70\%$, which is depicted in Fig. 2 with respect to the lateral position of the PM-substrate. Further measurements of the temporal intensity contrast improvement as well as extended benchmark experiments with nm-thin foils will be carried out in a current experimental campaign.

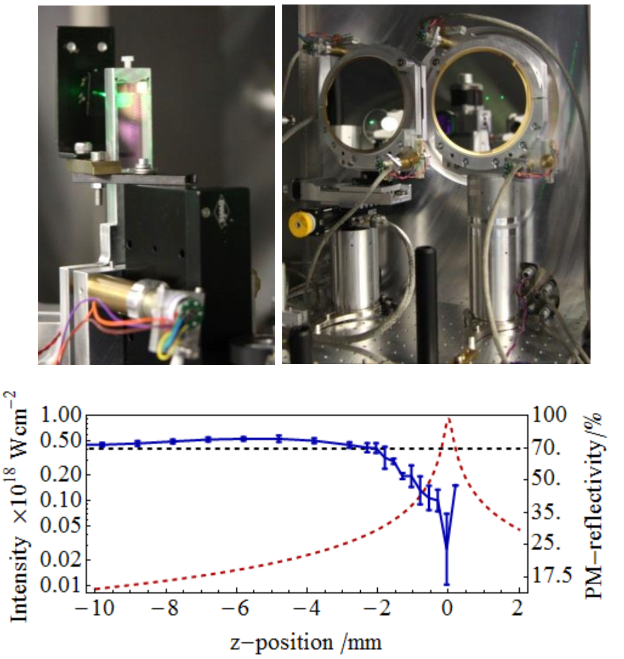

Figure 2: Upper row: PM-substrate (left picture) and the f/7 focusing parabolas (right picture) of the plasma mirror setup. Lower row: logarithmic plot of the estimated intensity (red, dashed line) and measured reflectivity (blue) vs. the z-position of the PM-substrate. z < 0 indicates positions behind the focus, which is located at $z = 0$ mm.

References

[1] M. Hornung et al., Opt. Lett., 41, 5413 (2016).
[2] A. Macchi, Rev. Mod. Phys. 85, 751 (2013).

POLARIS-Seeded Non-Collinear Optical Parametric Amplifier as an Optical Probe for Relativistic Laser-driven Interactions

I. Tamer[1,2], *S. Keppler*[1,2], *M. Hornung*[1,2], *M. Hellwing*[2], *F. Schorcht*[1], *M.C. Kaluza*[1,2]

[1]Helmholtz-Institute Jena, Germany; [2]Institute of Optics and Quantum Electronics, Jena, Germany.

Equipped with the POLARIS laser at the Helmholtz-Institut Jena, laser-based ion acceleration processes such as Target Normal Sheath Acceleration (TNSA) and Radiation Pressure Acceleration (RPA) are currently under investigation. Improving our comprehension of these processes requires advanced diagnostic methods to adequately resolve the miniscule spatial and temporal scales of the interactions. Here, optical probing is a powerful method through which a direct imaging of significant events – such as the temporal evolution of the plasma density [1] – is possible.

An optimal design of the optical probing setup must address important concerns regarding sufficient pulse energy, short pulse duration, high shot-to-shot power stability, proper synchronization with the POLARIS main pulse, and a center wavelength outside of POLARIS or its harmonics. To overcome these issues, a POLARIS-seeded laser system based on non-collinear optical parametric amplification (NOPA) was designed and is currently under construction. In this configuration, energy from a frequency doubled (1030 nm → 515 nm) “pump” pulse is transferred to a white light “signal” pulse within a thin nonlinear crystal – cut at a specific angle to fulfill the non-collinear phase-matching condition – resulting in a total gain factor exceeding 10^4 after two passes through the crystal. Along with the amplified signal pulse, a mid-infrared “idler” pulse is generated, which can be utilized as an additional probe pulse if necessary.

To model the NOPA process and optimize the crystal lengths and cut angles, a python-based 2-D simulation was constructed that solved the coupled wave equations [2] via the RK4IP method [3] for the signal, idler, and pump pulses

$$\begin{aligned}
&\frac{\partial A_{\mathrm{S}}}{\partial z}+\delta_{\mathrm{SP}}\cdot\frac{\partial A_{\mathrm{S}}}{\partial \tau}+\frac{GVD_{\mathrm{S}}}{2}\cdot\frac{\partial^2 A_{\mathrm{S}}}{\partial \tau^2}=i\,\frac{d_{\mathrm{eff}}\cdot\omega_{\mathrm{S}}}{c_0\cdot n_{\mathrm{S}}}\cdot A_{\mathrm{I}}^{*}A_{\mathrm{P}}e^{i\Delta kz},\\
&\frac{\partial A_{\mathrm{I}}}{\partial z}+\delta_{\mathrm{IP}}\cdot\frac{\partial A_{\mathrm{I}}}{\partial \tau}+\frac{GVD_{\mathrm{I}}}{2}\cdot\frac{\partial^2 A_{\mathrm{I}}}{\partial \tau^2}=i\,\frac{d_{\mathrm{eff}}\cdot\omega_{\mathrm{I}}}{c_0\cdot n_{\mathrm{I}}}\cdot A_{\mathrm{S}}^{*}A_{\mathrm{P}}e^{i\Delta kz}, \quad (1)\\
&\frac{\partial A_{\mathrm{P}}}{\partial z}+\frac{GVD_{\mathrm{P}}}{2}\cdot\frac{\partial^2 A_{\mathrm{P}}}{\partial \tau^2}=i\,\frac{d_{\mathrm{eff}}\cdot\omega_{\mathrm{P}}}{c_0\cdot n_{\mathrm{P}}}\cdot A_{\mathrm{S}}A_{\mathrm{I}}e^{-i\Delta kz},
\end{aligned}$$

with the slowly-varying electric field amplitude denoted as A_{j} (j = S, I, P for signal, idler, and pump, respectively), group velocity mismatch (with respect to the pump) δ, group velocity dispersion GVD_{j}, effective nonlinearity d_{eff}, central frequency ω_{j}, speed of light c_0, refractive index n_{j}, and phase-mismatch Δk.

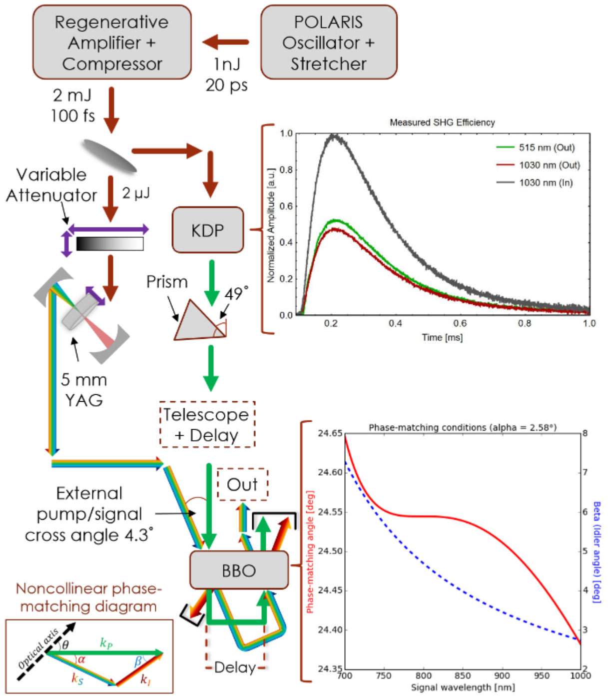

- NOPA center wavelength: 800 nm
- Phase-matching angle: 24.5°
- Internal pump/signal angle α: 2.6°
- Idler angle β: 4.7°
- BBO crystal length: 2 mm
- 2-pass conversion efficiency: 37%
- Design final energy: 150 µJ
- Design final bandwidth: 200 nm

Figure 1: Schematic of the NOPA optical probing system with simulation results for the SHG and NOPA processes.

In the realized setup, depicted in Figure 1, a single pulse from the 76 MHz pulse train of the POLARIS oscillator is selected using a Pockels cell and polarizing beamsplitter combination as the source for the optical probe. The pulse enters a chirped-pulse amplification (CPA) system – consisting of a stretcher, regenerative amplifier, and compressor – with a total gain factor exceeding 10^6. The pulse is then directed into the NOPA setup, with 1 mJ reserved for the second harmonic generation (SHG) within a KDP crystal and 2 µJ for white light generation (WLG) within a YAG crystal. Thus far, preliminary measurements reveal an SHG efficiency of over 50% and a white light bandwidth over 300 nm. Next steps include optimization of the stability of the white light spectrum, a modification of the pulse front tilt of the SHG pulse, and the temporal alignment of the SHG and WLG pulses. The two pulses will then meet at the BBO crystal under a specified angle for broadband amplification of the white light. The completed CPA + NOPA system is designed to be compact, portable, and optimized for use as an optical probe for laser-based particle acceleration experiments at POLARIS.

References

[1] M.B. Schwab, A. Sävert, O. Jäckel, J. Polz, M. Schnell, T. Rinck, L Veisz, M. Möller, P. Hansinger, G.G. Paulus, and M.C. Kaluza, Appl. Phys. Lett. 103, 19111 (2013).

[2] C. Manzoni and G. Cerullo, J. Opt. 18, 103501 (2016).

[3] J. Hult, J. Lightwave Technol. 25, 12 (2007).

Spatio-Temporal Characterization of Pump-Induced Wavefront Aberrations in Yb^{3+}-Doped Materials

I. Tamer[1,2], S. Keppler[1,2], M. Hornung[1,2], J. Körner[2], J. Hein[1,2], M.C. Kaluza[1,2]

[1]Helmholtz-Institute Jena, Germany; [2]Institute of Optics and Quantum Electronics, Jena, Germany.

State-of-the-art petawatt-class laser systems, such as the POLARIS laser at the Helmholtz-Institut Jena, are capable of generating focused laser intensities in excess of 10^{20} W/cm^{2}, empowering progress on research involving laser-plasma wakefield acceleration of electrons and laser-based ion acceleration. A further increase in the laser intensity can be achieved by amplifying the laser pulses to higher energies, but must be accompanied by an expansion in the beam diameter to reduce the fluence below the laser-induced damage threshold of the laser-active materials. Consequently, the near field homogeneity and the final focusability of the large diameter beam can be significantly degraded due to spatially inhomogeneous pump profiles and pump-induced wavefront aberrations, thereby reducing the achievable intensities and hence the efficiency of the desired laser-plasma interactions. The wavefront aberrations are the result of transverse optical path difference (OPD) profiles, arising from pump-induced thermal [1] and electronic [2] refractive index changes of the laser-active material, which are directly imprinted onto the wavefront of the laser pulse during amplification. In an effort to mitigate the influence of these pump-induced wavefront aberrations, we have conducted a comprehensive investigation [3] on Yb:YAG, Yb:CaF2, and Yb:FP15, which are employed in a variety of high power laser systems.

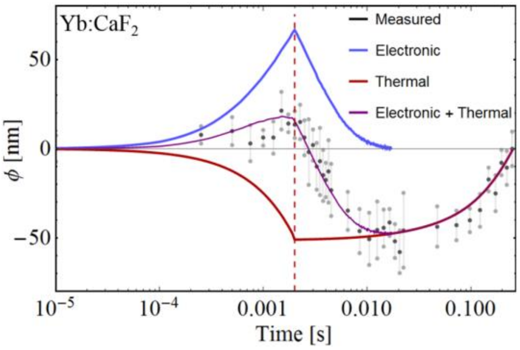

Figure 1: Temporal profiles of the measured (grey) and superposition (purple) of the thermal (red) and electronic (blue) OPDs.

The thermal and electronic contributions for each material were characterized independently and compared to measurements of the complete spatio-temporal pump-induced OPD profiles using a time-resolved Mach-Zehnder interferometer. As seen in the temporal profiles of the OPDs in Fig. 1, the thermal and electronic contributions can be distinguished from each other according to their temporal relaxation, and for the case of Yb:CaF$_2$, can cancel each other out during the time frame of laser amplification. For the case of Yb:YAG in Fig. 2, the spatial OPD profiles reveal a positive superposition of the thermal and electronic contributions, indicating a stronger influence of the wavefront aberrations in comparison to Yb:CaF$_2$.

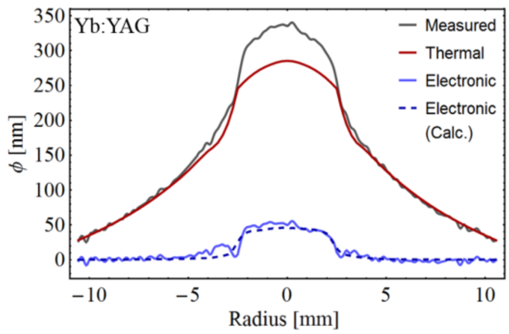

Figure 2: Spatial profiles of the measured (grey) and superposition (purple) of the thermal (red) and electronic (blue) OPDs.

To determine the effect on the spatial quality of the beam, the total pump-induced OPD profile can be further separated into a defocus component and the remaining high frequency spatial phase distortions. As seen in Fig. 3 for Yb:FP15, these distortions imprint an oscillatory structure with opposite signs of the phase delay in the center and near the edges of the pumped region that add up with each material pass, significantly deteriorating the spatial intensity profile upon propagation.

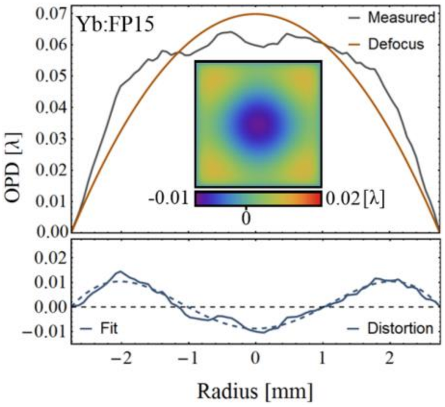

Figure 3: Spatial phase distortions (dark blue) from a single material pass after defocus (brown) correction.

With the material parameters and properties of the pump-induced wavefront aberrations revealed during this investigation, the designs of Yb-based laser systems worldwide, such as the POLARIS laser, can be optimized to achieve higher maximum pulse energies.

References

[1] S. Chénais, F. Druon, S. Forget, F. Balembois, and P. Georges, Prog. Quant. Electron. 30, 89 (2006).

[2] O.L. Antipov, D.V. Bredikhin, O.N. Eremeykin, A. P. Savikin, E.V. Ivakin, and A.V. Sukhadolau, Opt. Lett. 31, 763 (2006).

[3] I. Tamer, S. Keppler, M. Hornung, J. Körner, J. Hein, and M.C. Kaluza, Laser Photonics Rev. 12, 2 (2018).

Spectroscopic investigations of thulium doped YAG and YAP crystals between 77 K and 300 K for short-wavelength infrared lasers

Jürgen Reiter[1,2], Jörg Körner[1,2], Joachim Hein[1,2] and Malte C. Kaluza[1,2]

[1]Institute of Optics and Quantum Electronics, Friedrich-Schiller-University, Germany;
[2]Helmholtz Institute Jena, Germany;

Lasers operating in the short-wavelength infrared (SWIR) are very desirable for various applications, as these are widely regarded as eye-safe and therefore easier to use in medical or also military applications, like surgery or light detection and ranging (LIDAR). Furthermore, lasers emitting between 1800 nm and 1900 nm can be ideally used as pump sources for ultra-short pulse lasers based on chromium doped materials [1]. One promising candidate is the threefold positive rare earth thulium ion Tm^{3+} which exhibits some special features. Due to the so called cross relaxation process Tm^{3+}-doped media emit in the range between 1800 nm and 2050 nm even though they can be excited near 800 nm. Additionally, the quantum defect is still in the range of about 20 %, because each photon absorbed in the 800 nm band can generate two photons in the SWIR emission band.

So far, such laser sources were mainly developed in the context of high power fiber lasers [2], where continuous wave (CW) pumping is applied. There are, however, much fewer developments towards pulse pumped operation with bulk media for high energy lasers in the multi-Joule range. Moreover, the fluorescence lifetime of these materials is about ten times longer than that for ytterbium doped media. Hence, such media are ideally suited to build a pump for mid-infrared ultra high power lasers.

	Tm:YAG	Tm:YAP
τ_f @295 K	9.42±0.14 ms	3.81±0.15 ms
τ_f @77 K	15.22±0.30 ms	4.93±0.28 ms
η_Q @295 K	<1.23	<1.54
η_Q @77 K	<2	<2

Table 1: Measured fluorescence lifetimes (τ_f) and quantum efficiencies (η_Q) for two selected temperatures.

Since the design of such laser systems is a demanding task, its successful realization strongly depends on the availability of accurate data of the active medium. Reliable spectroscopic data are not available, even for the two most commonly used materials, thulium doped yttrium-aluminum-garnet (Tm:YAG) and yttrium-aluminum-perovskite (Tm:YAP). Therefore we measured the temperature dependent cross sections and re-absorption free fluorescence lifetimes for these materials in the temperature range of 80 K to 300 K. Table (1) shows the results for the lifetime measurements. We observed a significant enhancement of the fluorescence lifetime when cooling from room temperature to 77 K. This indicates that lifetime quenching, present at room temperature, can be overcome partially by cryogenic cooling. This is also supported by the measured emission and absorption cross sections [3].

As an example for the results of the absorption cross sections the calculated product of material thickness d and doping concentration c_a to achieve a total absorption of 90% is shown in Figure (1). The pump source is assumed to have a Gaussian spectral distribution of given full $1/e^2$-width $\Delta\lambda_p$ and center wavelength λ_p. For Tm:YAG two pump bands can be utilized around 765 nm and 784 nm. In practice the latter one should be of higher interest as it is better matched to the emission spectra of available high power laser diodes.

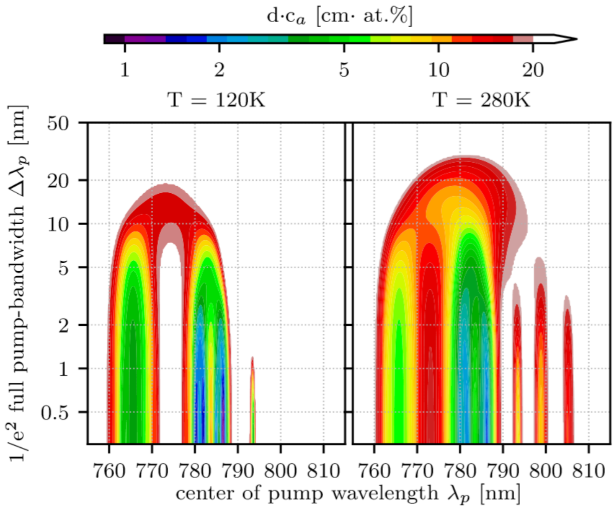

Figure 1: Material length times concentration for 90% absorption $d \cdot c_a$ as a function of the full $1/e^2$-bandwidth and the center wavelength of the pump radiation, with assumed Gaussian spectral distribution for Tm:YAG at 120 K (left) and 280 K (right). Smaller absorption lengths correspond to higher absorption.

References

[1] L. D. DeLoach, R. H. Page, G. D. Wilke, S. A. Payne, W. F. Krupke, Transition metal-doped zinc chalcogenides: spectroscopy and laser demonstration of a new class of gain media, IEEE Journal of Quantum Electronics 32 (6) (1996) 885–895.

[2] F. Jansen, F. Stutzki, C. Jauregui, J. Limpert, A. Tünnermann, High-power very large mode-area thulium-doped fiber laser, Opt. Lett. 37 (21) (2012) 4546–4548.

[3] J. Körner, et.al., to be published

Design of serrated aperture for JETI 200 laser system

M.Y. Shi[1,2], *A.Saevert*[2], *G.Schaefer*[2], *M.Kaluza*[2], *M.Zepf*[2]

[1] Friedrich-Schiller-Universität Jena, Germany; 2 Helmholtz-Institute Jena, Germany.

The laser beam edge modification is a critical part for laser system, especially for high intensity laser system. Along the propagation of the pulse, elements or hard aperture will cut the beam and lead to diffraction on the edges of the mirrors. A serrated aperture system is used to avoid this diffraction. This system can produce beams with gaussian edge profiles. We present the principle of serrated aperture system and simulation results and want to apply it to JETI200 laser system.

Principle of operation

The beam shape is determined by the amount of transmitted energy and a serrated aperture is used to control transmitted energy [1,2]. The principle of the serrated aperture is that the edge shape of the aperture is the shape of the filtered beam edge profile. A serrated aperture system includes two parts, namely a serrated aperture and a spatial filter. The beam pass through a serrated aperture and the edge of beam is imprinted by serrated aperture, and then the beam pass through a spatial filter. The function of spatial filter is to remove the serrated beam pattern.

Because the propagation of light from spatial filter input plane to output plane corresponds to a net propagation distance of zero [2]. In simulation, as shown in Figure 1, the serrated aperture system models with the following calculation [1,2]:

1.The beam is imprinted by the serrated aperture.

2.The shaped beam is transformed from real space into Fourier space.

3.The diffraction pattern is obtained by multiplying the Fourier transformed beam by the pinhole function.

4.The inverse Fourier transform is performed to calculate the filtered beam at the output relay plane.

These four steps can determinate the connection between the serrated system and output beam profile.

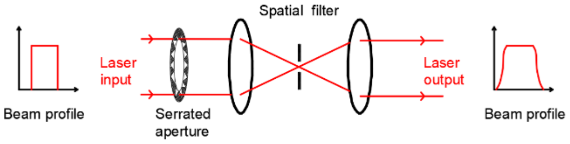

Figure 1: The operation of a serrated aperture system.

Serrated aperture design

The serrated aperture type design

We design three different serrated apertures, "Single ring","2-D" and "2-rings", as shown in Figure 2. The "2-D" and "2-rings" aperture separate the beam into two parts with the smooth edge. The two separated beams can be used to SPIDER measurement, pump-probe measurement and so on.

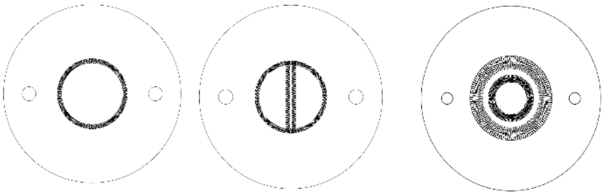

Figure 2: Three different serrated apertures, "Single ring","2-D" and "2-rings" from left to right respectively.

Serrated aperture parameters

There are several key parameters for serrated aperture design. The first is serration height to period ratios (H/L). Auerback[2] indicated this ratio must be larger than 6, if this ratio is too small, the beam edge profile can't keep the serrated aperture shape when it pass through a pinhole. The second key parameter is the pinhole size. From the simulation, if pinhole size is too big, the imprinted pattern can't be removed. If this size is too small, which leads to some rings on the centre of beam, as shown in Figure 3. In real experiment, the suitable pinhole size is around 1mm -2mm.

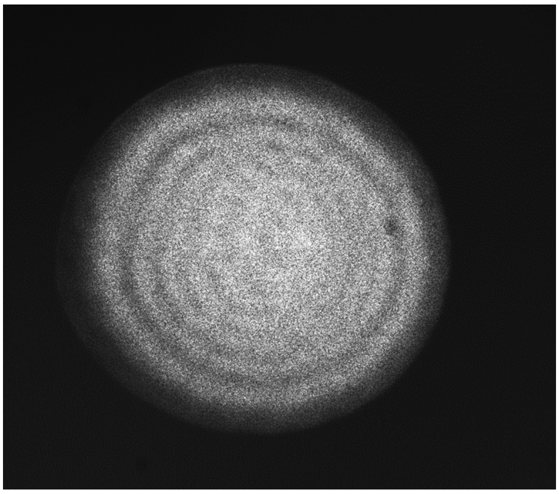

Figure 3: In experiment, the small pinhole lead to some rings on the centre of beam.

References

[1] Bontoux, T., Saiki, T., Kanabe, T., Fujita, H., & Nakatsuka, M. (1998). Study of serrated aperture for a cassegrain booster amplifier. Optical Review, 5(4), 234-241.

[2] Auerbach, J. M., & Karpenko, V. P. (1994). Serrated-aperture apodizers for high-energy laser systems. Applied Optics, 33(15), 3179.

1.9 kW average power 16-channel ultrafast fiber laser system

M. Mueller[1], *A. Klenke*[1,2], *H. Stark*[1], *J. Buldt*[1], *T. Gottschall*[1],
A. Tünnermann[1,2,3], *and J. Limpert*[1,2,3]

[1]Friedrich Schiller University Jena, Institute of Applied Physics, Jena, Germany
[2]Helmholtz-Institute Jena, Fröbelstieg 3, 07743 Jena, Germany
[3]Fraunhofer Institute for Applied Optics and Precision Engineering Jena, Germany

Ytterbium-doped ultrafast fiber lasers are versatile tools in scientific applications. An example is the generation of high-harmonics for experiments with attosecond pulses or diffraction imaging. The demands of these applications pushed the development of very-large-mode-area fibers and chirped-pulse amplification systems to handle nonlinear effects associated with the amplification of ultrashort pulses. Both technologies have matured and are constrained by manufacturing cost and tolerances. Now, the next generation power scaling technique is coherent beam combination (CBC, [1]).

In this contribution, an ultrafast fiber laser based on CBC of 16 amplifier channels is presented, demonstrating the huge power scaling potential this technique.

The setup is depicted in Fig. 1. The centerpiece of this system is a 16-channel interferometer with one ytterbium-doped large-pitch fiber amplifier (LPF) in each channel. The system is are arranged in two layers. A seed beam provided by preamplifiers is split into these channels using polarization beam splitters and half-wave plates (HWP). Each interferometer channel is equipped with a piezo-driven mirror for phase stabilization against environmental perturbations. After the amplifiers, the beams are superposed via polarization beam combining using thin-film polarizers (TFP). After each combination step, the superposed beam features linear polarization. Using a HWP after each step, the polarization is rotated back to p-state to allow full transmission through the following TFP. The output beam is enlarged in a lens telescope and is sent into a Treacy-type compressor. A more detailed description of the conceptually identical precursor to this system can be found in [2].

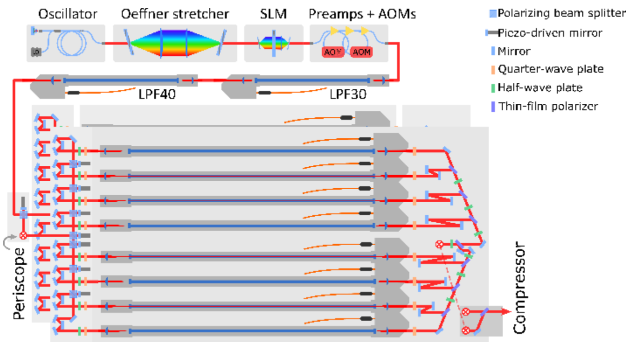

Figure 1: Schematic of the setup of the 16-channel laser.

The system frontend was set to generate a seed pulses with 481 kHz repetition rate and an average power of 41 W. The individual amplifiers delivered between 130 W to 150 W of average power at maximum pump power of 250W (976nm pumping). All beams combined yield 1925 W average power at 92% efficiency. The output spectrum features a FHWM of 10.2 nm supporting a transform limited pulse duration of 200 fs. The pulse duration was measured with an auto-correlator to be 220 fs FWHM. The most remarkable result is that the output beam quality is close to diffraction limited with M² = 1.1 on both beam axis, which is as good as the beam quality from a single emitter. Hence, coherent beam combination allows for power scaling far beyond the performance of a single amplifier channel without deterioration of laser parameters.

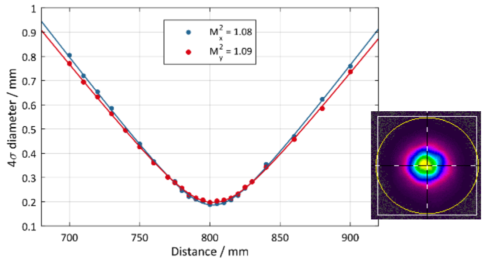

Figure 2: Beam caustic and output beam profile at 1.9kW average power proving a diffraction limited beam quality.

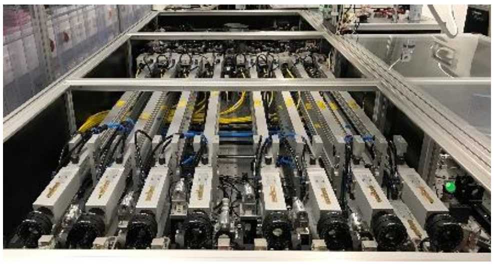

Figure 3: Photograph of the laser main amplifier stage.

In summary, a 16-channel ultrafast fiber laser system is presented, delivering the highest average power ever reported from an ultrafast fiber laser system. Output characteristics of individual amplifiers are maintained, allowing the development of ultra-high peak power laser sources far beyond the state of the art. One day, CBC will enable lasers even for particle acceleration that are technically impossible today [3].

References

[1] T.Y. Fan, et al., “Beam combining of ytterbium fiber amplifiers,” J. Opt. Soc. Am. B, 24, 8, 2007.
[2] M. Müller, et al., “1 kW 1 mJ eight-channel ultrafast fiber laser,” Opt. Lett., 41, 15, 2016.
[3] W. Leemans, “White paper of the ICFA-ICUIL joint task force: High power laser technology for accelerators,” ICFA Beam Dyn.Newslett., 56, 2011.

Acknowledgment: This work has been partly supported by the European Research Council grants no. [617173] “ACOPS” and [670557] ‘MIMAS’. M.M. acknowledges financial support by the Carl-Zeiss-Stiftung.

Enhancement of temporal contrast by filtered SPM broadened spectra

J. Buldt,[1] *M. Mueller,*[1] *R. Klas,*[1,2] *T. Eidam,*[3] *A. Tünnermann,*[1,2,4] *and J. Limpert,*[1,2,4]

[1]Institute of Applied Physics, Abbe Center of Photonics, Friedrich-Schiller-Universität Jena, Albert-Einstein-Str. 15, 07745 Jena, Germany; [2]Helmholtz-Institute Jena, Fröbelstieg 3, 07743 Jena, Germany; [3] Active Fiber Systems GmbH, Wildenbruchstr. 15, 07745 Jena, Germany; [4]Fraunhofer Institute for Applied Optics and Precision Engineering, Albert-Einstein-Str. 7, 07745 Jena, Germany

For the applications of high pulse energy, ultrafast lasers the pulse contrast is a crucial parameter. In strong-field physics, where an energetic laser interacts with matter, prepulses can contain sufficient energy to modify the experimental conditions. Therefore these experiments usually require a temporal pulse contrast exceeding 10 orders of magnitude. Common techniques to enhance the temporal contrast are cross-polarized wave generation (XPW) [1], nonlinear ellipse-rotation (NER) [2] and plasma mirrors [3]. But since these techniques are limited in average power, repetition rate or achievable contrast enhancement new techniques of contrast enhancement for future lasers and applications are required.

Here, a novel solution for contrast enhancement is presented that has a high efficiency of 30 % or more and with simultaneous pulse compression can conserve the peak power while being simple to implement. Another advantage of the presented technique is, that it relies on self-phase-modulation (SPM). SPM has already been widely used for pulse compression and the concepts can be used for contrast enhancement, too. Promising concepts for high pulse energies and average powers are bulk media [4] and gas filled multipass cells [5].

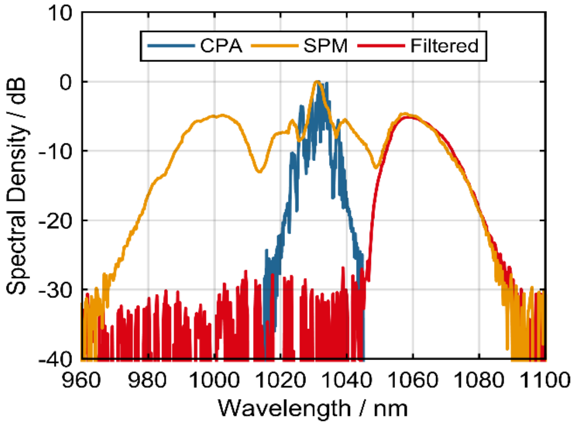

Figure 1: Spectrum of CPA-signal (blue), which is spectrally broadened by SPM (yellow) and filtered (red).

The output from an ytterbium based ultrafast fiber CPA system [6] is transmitted through an argon filled hollow-core fiber (HCF). The incident spectrum (Figure 1), which is centred at 1030 nm is spectrally broadened by self-phase modulation (SPM). Then, the signal is filtered with two long pass filters with the edge at 1050 nm. The broadening is adjusted by the gas pressure, such that the minimum spectrum coincides with the filter edge. The filtered signal has a very smooth spectrum centred at 1060 nm and an energy content of 20 – 30 % of the HCF-output pulses. It also has no spectral overlap with the incident spectrum, which is limited by the spectral hard cut of the compressor. The contrast is measured with a third order cross-correlator (Amplitude Technologies, Sequoia) with a dynamic range of ten orders of magnitude.

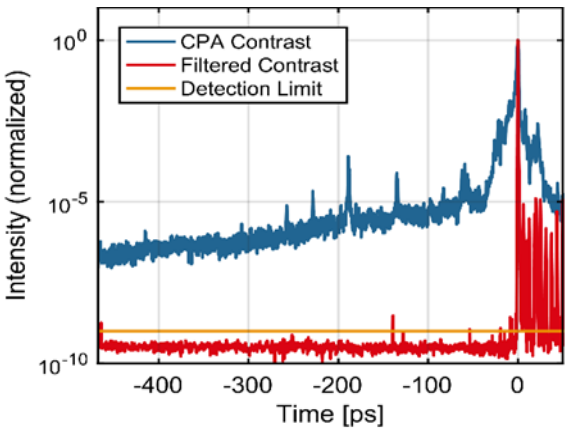

Figure 2: Pulse contrast of the CPA system before and after the contrast enhancement. The post-pulses (red curve) arise from internal reflections in the spectral filters.

As shown in Figure 2 the measured contrast of the filtered signal is better than 10^{-9}. Compared to the contrast of the incoming pulses of about 10^{-2} a contrast enhancement of at least seven orders of magnitude has been achieved. Since two filters, with a contrast of six orders of magnitude between blocking and transmission region each, were used one can expect the contrast to be even higher. The post-pulses in the filtered signal are caused by internal reflections in the spectral filters and could be avoided by using wedged filters.

In conclusion, we have demonstrated a novel technique for contrast-enhancement based on SPM in a proof-of-principle experiment. The method is simple to implement and allows highly efficient temporal pulse cleaning.

References

[1] A. Jullien et al., *Optics Letters*, **30**, 920, 2005.
[2] D. Homoelle et al., *Optics Letters*, **27**, 1646, 2002.
[3] H.C. Kapteyn et al., *Optics Letters*, **16**, 490, 1991.
[4] P. Lassonde et al., *Las. Phys. Let.*, **13**, 075401, 2016.
[5] M. Hanna et al., JOSA B, **34**(7), 1340, 2017.
[6] M. Kienel et al., *Optics Letters*, **41**, 3343, 2016.

Table-top and high-resolution Fourier transform holography

W. Eschen[2,3], G.K. Tadesse[1,2], R. Klaas[1,2], V. Hilbert[2], D. Schelle[2], A. Nathanael[2], M. Zilk[2], M. Steinert[2], F. Schrempel[2], T. Pertsch[2], A. Tünnermann[1,2,3], J. Limpert[1,2,3] and J. Rothhardt[1,2]

[1]Helmholtz Institute Jena, Jena, Germany; [2]Institute of Applied Physics, Friedrich Schiller University Jena, Jena, Germany; [3]Fraunhofer Institute for Applied Optics and Precision Engineering, Jena, German

We demonstrate a resolution of 34nm, which is the highest resolution so far demonstrated with Fourier Transform Holography at any light source. This was possible by combining a fibre laser driven high photon flux XUV source with latest nanofabrication technology.

Introduction

Coherent diffractive imaging (CDI) is a popular method for high resolution imaging with short wavelengths at large scale facilities as e.g. synchrotrons or free-electron-lasers. In CDI the far field diffraction pattern of an object is recorded without any optical elements between sample and detector which has the advantage that there is no loss or aberration introduced by optics. On the other hand, one must solve the so-called Phase Problem since the intensity is measured but the phase is lost. To recover the phase usually iterative algorithms, which are computationally intensive, are used [1]. In Fourier transform holography a reference wave is used to encode the phase in the measured diffraction pattern which enables straight forward reconstruction of the object without iterative algorithms.

In our experiment we used a table-top setup. A femtosecond fibre laser centred at 1030nm was focused into an argon gas jet to generate high harmonics. From the generated frequency comb a single harmonic at a wavelength of 18nm was selected and focused onto the sample by a pair of multi-layer mirrors as shown in figure 1 [2]. The sample consisted of the Logo of the Institute of Applied Physics (IAP) and five reference holes (figure 1 (b)) with a diameter of 50nm each. Since the achievable resolution is ~70% of the hole diameter [3] a resolution of 35nm can be reached.

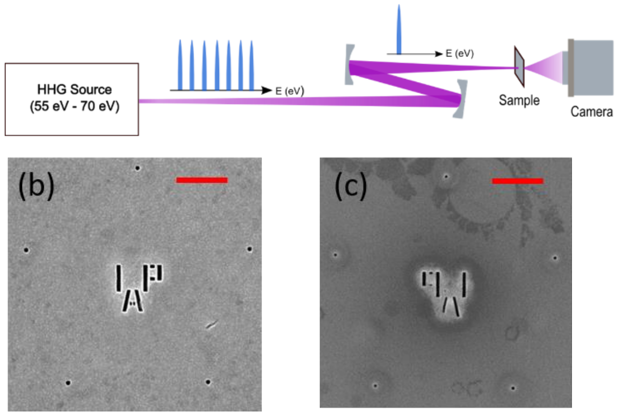

Figure 1: (a) Setup of the Fourier Transform Holography experiment. A XUV frequency comb is generated by a fibre laser. A single harmonic line is selected and focused by two multilayer mirrors. The diffraction pattern of the sample is collected in the far field by a XUV Camera. HIM front (b) and back (c) image of the sample and references. The scalebar is 500nm

Results and Discussion

An acquisition time of 20 seconds was used for recording the diffraction pattern (see figure 2 (a)). The Fourier transformation (see figure 2 (b)) of the recorded hologram gives the autocorrelation of the sample which includes the cross correlations of the IAP-Logo with the reference holes and resolves therefore the object. One of the cross-correlations from figure 2 (b) is shown in figure 2 (c).

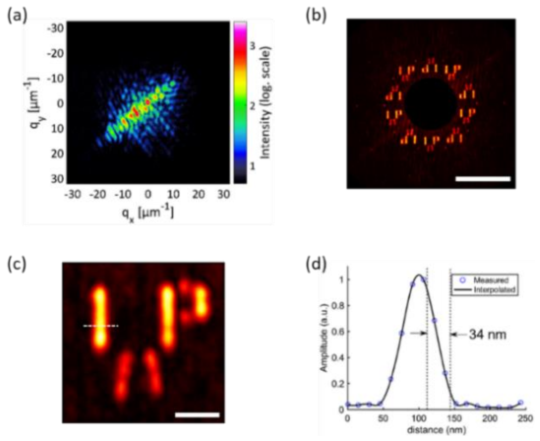

Figure 2: (a) Recorded hologram of the sample in logarithmic scale. (b) Fourier Transform of the Hologram yields the autocorrelation of sample. Scale bar corresponds to 2µm. (c) One of the cross-correlations of the IAP-Logo with the reference holes. Scale bar corresponds to 200nm. (d) Cross-section along the letter "I" from figure (b) which shows a 10/90 resolution of 34nm.

A cross-section along the dotted line is plotted in figure 2 (d) and gives a half-pitch (10/90) resolution of 34nm which indicates that the achieved resolution is limited by the reference hole diameter. Furthermore, the achieved resolution of 34nm is the highest resolution so far measured in a Fourier transform holography experiment from any light source. The disagreement between the HIM measurement and the reconstruction of the hologram origins form the sample manufacturing process. The IAP-structure was not in all regions successfully drilled through the sample which can be seen in the HIM measurement of the back of the sample (see figure 1 (c)). In future we will investigate real-world, biological samples and combine FTH with tomography to image 3-dimensional objects.

References

[1] J. Miao et al., Science, 348 , 530-535 (2015)

[2] J. Rothhardt et al., Opt. Express 24, 18133–18147 (2016)

[3] W. F. Schlotter, Dissertation, Stanford University, (2007)

Separation of High Average Power Driving Lasers from Higher Order Harmonics Using an Annular Beam

R. Klas[1,2]*, A. Kirsche*[1]*, M. Tschernajew*[1,2]*, J. Rothhardt*[1,2]*, J. Limpert*[1,2,3,]

[1]Institute of Applied Physics, Abbe Center of Photonics, Friedrich-Schiller-University Jena, Albert-Einstein-Straße 15, 07745 Jena, Germany

[2]Helmholtz Institute Jena, Fröbelstieg 3, 07743 Jena, Germany

[3]Fraunhofer Institute for Applied Optics and Precision Engineering, Albert-Einstein-Straße 7, 07745 Jena. Germany

Coherent extreme ultraviolet (XUV) light sources, based on high harmonic generation (HHG), are pivotal for a plethora of experiments at the Helmholtz Institute aiming at the understanding of fundamental chemical, biological and physical mechanisms. In particular, recent advances of high-flux coherent XUV sources (driven by high average power ultrafast solid-state lasers amplifiers [1]) enable novel experiments. Since the conversion efficiency of HHG is of the order of 10^{-9} to 10^{-5}, there is a great demand for an efficient separation of driving laser and generated high harmonics. Otherwise sensitive and expensive mirrors, samples or detection devices could be damaged, or experiments could be disturbed. Routinely used separation methods for high average power driving lasers and XUV light are grazing incidence plates (GIPs) (with an antireflective coating for the driving laser [2]) as well as thin metal filters. However, thin metal filters are very fragile and break at a few watts of average power, while GIPs have to be designed for the specific driving pulse parameters and get more and more difficult to realize for high photon energies. With the ever-growing average power of ultrashort pulsed amplifier systems [3], there is huge demand for alternative power- scalable separation techniques.

Here, we present a detailed study of HHG driven by annular beams. A simple pinhole can be used for separation, since the generated XUV beam is generated within the inner divergence cone of the annular beam. An excellent suppression of the driving laser by three orders of magnitude is observed, while the XUV beam stays unaffected. This concept already has been shown in 1994 [4] and is established e.g. in many Attosecond beamlines. However, the influence of the shaped beam on phase matching and efficiency has not been investigated in detail yet and is in focus of this study.

The setup for the experiment is shown in Fig. 1. A commercial femtosecond laser amplifier (Active Fiber Systems GmbH) was used as a driving laser. Afterwards the beam was sent either over a plane mirror or a pierced mirror with a 2 mm hole. HHG was achieved in a gas jet geometry and the XUV light was analysed with a flat field spectrometer.

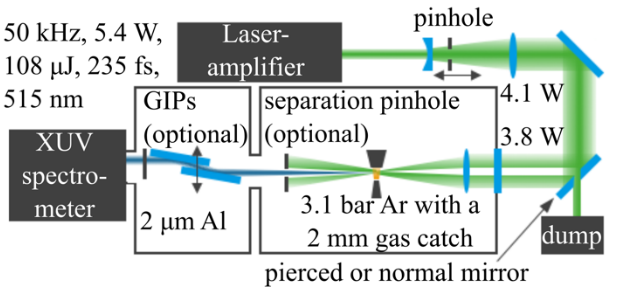

Figure 1: Experimental setup for HHG with annular

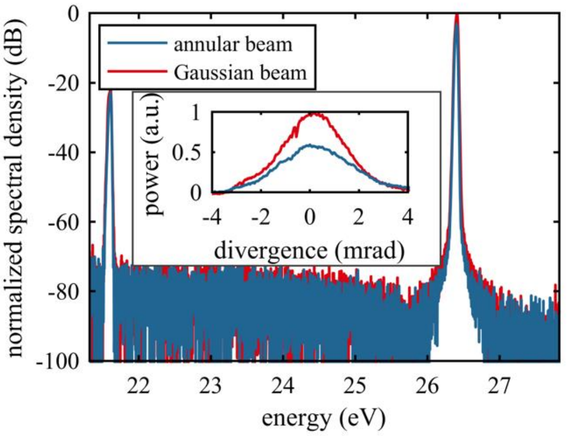

Figure 2: Normalized spectra for HHG with an annular and a Gaussian beam and the spatial profile (shown in the

First, the phase matching conditions for HHG with an annular beam have been compared to the conditions with a Gaussian beam. The driving laser was running with identical parameters for both beams. The lack of pulse energy due the pierced mirror of 76 µJ, compared to 81 µJ with a plane mirror, was negligible. Similar focal spot size and shapes have been observed for an annular and a Gaussian beam. Moreover, the Gouy phase gradient has been calculated to be similar in both cases. At last, the similar spectral and spatial shape of the XUV radiation (shown in Fig. 2) confirm that HHG takes place under similar phase matching conditions.

The conversion efficiency of the HHG process has been measured to $(2.6 \pm 0.2) \cdot 10^{-5}$ and $(1.9 \pm 0.2) \cdot 10^{-5}$ for a Gaussian beam and an annular beam, respectively. Resulting in a $(26.9 \pm 13.3)\%$ lower conversion efficiency of HHG with an annular beam compared to a Gaussian beam.

In conclusion, it has been shown, that HHG with an annular beam yields similar phase matching conditions and similar conversion efficiency as HHG with a Gaussian beam. This enables a power-scalable separation, that does not depend on the driving laser central wavelength, the pulse duration nor the generated XUV photon energy.

References

[1] S. Hädrich, et al., Journal of Physics B: Atomic, Molecular and Optical Physics 49.17 (2016) 172002.
[2] O. Pronin, et al., Optics Express 19.11 (2011) 10232.
[3] M. Müller, et al., Optics Letters 41.15 (2016) 3439.
[4] J. Peatros, et al., Optics Letters 19.13 (1994) 942.

High power few-cycle laser source development at 2 µm wavelength

M. Gebhardt,[1,2] *C. Gaida,*[2] *T. Heuermann,*[1,2] *F. Stutzki,*[2,+] *C. Jauregui,*[2] *J. Antonio-Lopez,*[3]
A. Schulzgen,[3] *R. Amezcua-Correa,*[3] *A. Tünnermann*[1,2,4] *and J. Limpert,*[1,2,4,#]

[1]Helmholtz-Institute Jena, Fröbelstieg 3, 07743 Jena, Germany; [2]Institute of Applied Physics, Abbe Center of Photonics, Friedrich-Schiller-Universität Jena, Albert-Einstein-Str. 15, 07745 Jena, Germany; [3]CREOL, College of Optics and Photonics, University of Central Florida, Orlando, Florida 32816, USA; [4]Fraunhofer Institute for Applied Optics and Precision Engineering, Albert-Einstein-Str. 7, 07745 Jena, Germany

Ultrafast laser systems with an emission wavelength around 2 µm are becoming regularly used tools for driving high-field light-matter interactions like the efficient generation of high-order harmonics (HHG) within the water-window [1]. However, numerous subsequent experiments like time-resolved observation of light-induced chemical reaction paths [2] and X-ray absorption edge spectroscopy of organic molecules [1] demand a significant increase in photon flux to transform laboratory demonstrations into real world applications with high signal-to-noise ratios and fast data acquisition. Hence, there is a strong application driven demand for the development of intense high-average power laser systems in the 2 µm wavelength regime. In this regard, thulium-doped fiber laser systems (TFL) represent a promising concept with substantial power scaling prospects. Recently, we have demonstrated kW-level average power in ultrafast operation [3] and several GW of peak power with 100 fs pulse duration [4], directly from a fiber laser system. These results emphasize the great potential of 2 µm fiber laser systems to enable future applications in high-field science.

It has been identified that few-cycle pulse duration is especially important for long-wave driven high-efficiency, high-cut-off HHG. One way of elegantly achieving this requirement is to operate in the nonlinear self-compression regime [5]. This is particularly interesting in the 2 µm wavelength regime where the anomalous waveguide dispersion within a hollow waveguide can overcome the normal material dispersion of the gas filling, which is responsible for the self-phase modulation (SPM) induced spectral broadening. If such anomalous net dispersion can compensate the SPM-induced chirp, the pulses are temporally compressed as they propagate along the pulse compression stage leading to a gradual increase in peak power and nonlinearity enabling large compression factors. Following this approach, a high-power self-compression experiment has been designed [6], which principal setup can be seen in Fig. 1. Its key component was an antiresonant hollow-core fiber (ARHCF) with 53 µm core diameter allowing for excellent power transmission of >90% including coupling losses. It was filled with 3 bars of Ar at its output side providing sufficient nonlinearity to broaden the input pulse spectra from the TFL to ~800 nm 20 dB-width. The overall compressed average power was 43 W, corresponding to 34 µJ of pulse energy at 1.25 MHz repetition rate. The significant pulse compression becomes apparent when comparing the input and output intensity autocorrelation traces depicted in Fig. 2. Based on numerical modelling of the pulse evolution along the ARHCF a pulse duration of 13 fs (2.1 optical cycles) and a pulse peak power >1 GW could be retrieved. The laser source presented herein is, to our knowledge, the highest average power 2 µm laser system delivering few-cycle pulses.

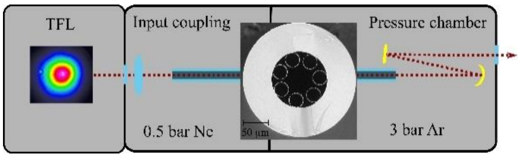

Figure 1: Schematic sketch of the experimental setup.

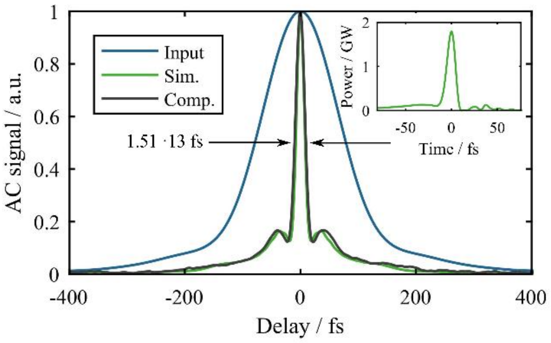

Figure 2: Measured AC traces before (blue) and after the nonlinear pulse compression stage (black) as well as simulation results (green). Inset: Retrieved pulse profile.

Outlook Our future work will include further power and energy scaling exploiting the full potential of ultrafast TFLs. However, we have also used the source described herein for mid-infrared generation via intra-pulse DFG and we have demonstrated unprecedented brightness and spectral bandwidth at >10 µm wavelength [7]. Additionally, the achieved laser parameter are exceptionally interesting for driving water-window HHG at MHz-repetition rate with unprecedented photon flux.

References

[1] S. L. Cousin et al., Opt. Lett. 39, 5383 (2014)
[2] Y. Pertot et al., Science, 355(6322), 264 (2017)
[3] C. Gaida et al, Proc. SPIE PW 10512 (2018)
[4] M. Gebhardt et al., Europe-EQEC CJ_11_1J (2017)
[5] T. Balciunas et al., Nat. Comm. 6, 6117 (2015)
[6] M. Gebhardt et al., Opt. Lett. 42, 4179 (2017)
[7] C. Gaida et al., submitted to LSA (2018)

[#]jens.limpert@uni-jena.de
+F.S. is now with Fraunhofer Institute for Applied Optics and Precision Engineering

Laser Particle Acceleration

Influence of a Prepulse on the Maximum Proton Energy

G.A. Becker[1]*, S. Keppler*[1,2]*, M. Hornung*[1,2]*, M. Hellwing*[1]*, F. Schorcht*[2]*, J. Hein*[1,2]
and M. C. Kaluza[1,2]

[1]Institut für Optik und Quantenelektronik, Friedrich-Schiller-Universität Jena, Germany;
[2]Helmholtz-Institut Jena, Germany;

Since the turn of the millenium, significant experimental and theoretical research has been devoted to the field of laser-driven proton acceleration. With a deeper understanding of the physical mechanisms behind this type of interaction, higher maximum energies of the accelerated protons may be achieved, necessary for applications [1].

To accelerate protons with a high-intensity laser pulse ($> 10^{18}\ \mathrm{W/cm^2}$), the pulse is focused on, e.g., a micrometer thin metal foil. Here, the rising edge of the laser pulse ionizes the foil's front side on a picosecond timescale resulting in the generation of a plasma. The main laser pulse accelerates electrons from this preplasma via the Lorentz force through the metal foil, leading to the formation of an electron sheath at the foil's rear side.

Between the electron sheath and the positively charged foil, an electric field builds up with a field strength on the order of $\mathrm{MV/\mu m}$. This field accelerates ions from the foil's back side as well as protons and ions from hydrogen containing contaminants to kinetic energies in the MeV-regime.

The characteristics of the accelerated proton beam like the maximum proton energy depend not only on the laser pulse's intensity but also on the temporal intensity contrast (TIC).

By drastically improving the TIC, it is possible to use few nanometer thin foils as targets and eventually increase the maximum proton energy via more efficient acceleration mechanisms [2]. However, contrast improvement mechanisms, such as a plasma mirror, lead to a decrease in the laser energy, thereby decreasing the overall intensity on the target.

A different approach would be to enhance the coupling of laser energy into hot electrons and therefore enhance the proton energy. This could be done by modifying the preplasma with which the main laser pulse interacts by introducing a controlled prepulse with a certain intensity and temporal delay relative to the main laser pulse.

An experiment has been performed at the Helmholtz-Institute Jena utilizing the POLARIS laser to investigate the influence of a variable prepulse on the maximum proton energy. In this experiment, POLARIS delivered laser pulses with a full-width-at-half-maximum (FWHM) pulse duration of $\tau \approx 200\ \mathrm{fs}$. The pulses were focused in a FWHM focal spot with $A \approx 32\ \mathrm{\mu m^2}$ containing 25 % of the laser pulse's energy. The main pulse intensity was varied by changing the laser energy ($\approx 2.5\ \mathrm{J},\ 5\ \mathrm{J},\ 10\ \mathrm{J}$) resulting in the laser intensities of $I_1 \approx 1 \cdot 10^{19}\ \mathrm{W/cm^2}$, $I_2 \approx 2 \cdot 10^{19}\ \mathrm{W/cm^2}$ and $I_3 \approx 4 \cdot 10^{19}\ \mathrm{W/cm^2}$, respectively. The maximum proton energies were measured with a Thomson Parabola Spectrometer under the target normal direction.

In Figure 1, the maximum proton energy is plotted over the foil's longitudinal position relative to the laser focus' position for I_3 without a prepulse and with a prepulse with fixed intensity $I_p = 3 \cdot 10^{-5} I_2$ (or $I_p = 1.5 \cdot 10^{-5} I_3$), which arrives 500 ps before the main pulse. The introduction of this prepulse leads to a significant enhancement of the maximum proton energies.

This enhancement depends not only on the delay, but also on the main laser pulse's intensity, as seen in Figure 2. For the I_1-case there is only a small increase of the proton energy (~20 %) for the 50 ps delay relative to the reference case without prepulse (0 ps). For the I_2-and I_3-cases the proton energy increases by ~ 50 % for the optimal delay of 100 ps.

A possible explanation for the increase in proton energy could be that the main laser pulse undergoes self-focusing in the preplasma induced by the prepulse [3]. Simulations will be performed to investigate this and also an experiment at POLARIS will be performed to optically probe the plasma induced by the prepulse.

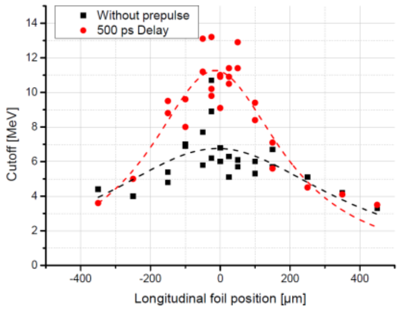

Figure 1: Dependence of the maximum proton energy on the foil's longitudinal position. Positive numbers correspond to the foil moving towards the focusing parabola.

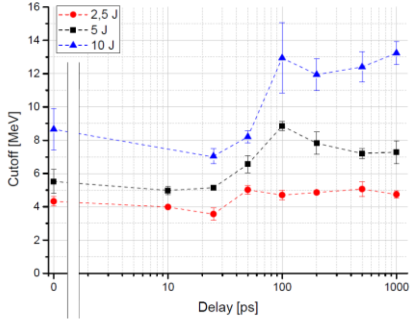

Figure 2: Dependence of the maximum proton energy on the prepulse delay relative to the main pulse for three different laser pulse energies. 0 ps is without prepulse.

References

[1] Macchi et al., Rev. Mod. Phys. 85, 751 (2013).
[2] Esirkepov et al., PRL 92, 175003 (2004).
[3] Bin et al., PRL 115, 064801 (2015).

Short-pulse multiplexing for temporal-resolved optical probing of plasmas

A. Massinger[1], S. Keppler[1,2], I. Tamer[1,2], M. Hornung[1,2], and M. C. Kaluza[1,2]

[12]Institute of Optics and Quantum Electronics, Jena, Germany; ²Helmholtz-Institute Jena, Germany

For laser-driven particle acceleration of protons or heavier ions from solid-density targets the temporal intensity contrast is one of the most important experimental parameters. Intense prepulses and/or the rising slope of the main pulse induce a preplasma in which the main pulse is absorbed, and thus, fast electrons are generated. In the so called 'Target-Normal-Sheath-Acceleration' (TNSA) regime, these electrons travel through the target and create a sheath field on the target's back side, in which protons from contamination layers are accelerated. In order to fully understand the influence of the preplasma and the generation of the backside's sheath-field, optical probing of the interaction with multiple, temporally separated short pulses would give a deep time resolved insight into the occurring processes. The slope of the main laser pulse rises on the time scale of several picoseconds (ps), which defines the necessary temporal resolution of the optical probing. To achieve this, different methods like "serial time-encoded amplified microscopy" (STEAM) [1], "sequentially timed all-optical mapping photography" (STAMP) [2], "single-shot multispectral tomography" (SMT) or other methods [3] can be used. Due to its high temporal resolution and the multi-shot imaging, the STAMP setup is most suitable for the investigation of laser-induced plasmas.

To realize this principle in experiments for proton acceleration at the POLARIS laser system, a fraction of the POLARIS seed pulse, generated by a commercial Ti:Sa oscillator 'MIRA 900' operating at 1030 nm [4], is separately amplified by a Yb:glass regenerative amplifier up to an output energy of 2 mJ with a pulse duration of (157±1) fs. For the temporal multiplexing, this pulse is diffracted at a grating and collimated with a lens at the distance of its focal length. Afterwards, different spectral components are back reflected by different 0°-mirrors as shown in Fig. 1. After the spectral components are diffracted again at the grating, multiple single pulses are generated from the single incoming short pulse.

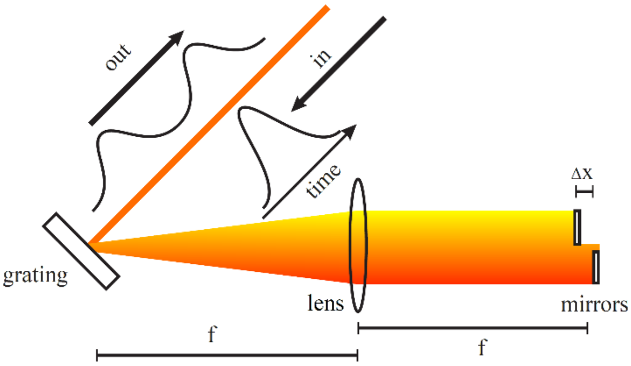

Figure 1: Schematic of the temporal multiplexing of an optical probe pulse. The incoming pulse is diffracted at the grating and imaged on two independently moveable mirrors, which reflect different spectral parts with different time delays.

The separation of the incoming and outgoing pulses was realised via a Glan-Thompson polarizer in combination with a Faraday rotator. The time delays between the individual pulses are given by the different optical path lengths determined by the lateral position of the 0°-mirrors. In order to fully characterize the multiplexed pulses, the spectrum, the spatial intensity profile in near and far field as well as the pulse duration were measured. Here, the incoming pulses provide a spectral bandwidth of 18 nm and a duration of (157±1) fs. With the multiplexing setup, two separated pulses with a slightly longer duration of (223±1) fs and (268±4) fs could be realized. Finally, the absolute delay between the separated pulses was measured with a dye-auto-correlator. The two separated pulses cause a symmetric 3-peak structure in the autocorrelation, where the spatial distance corresponds to the time delay of the multiplexed pulses (see Fig. 2).

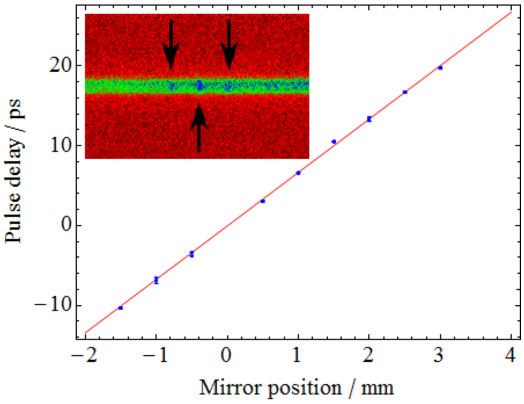

Figure 2: Pulse delay inside the dye correlator vs. the difference of the Δx-position of both 0°-mirrors. The embedded image shows a picture of the dye autocorrelation.

If the spectrally separated pulses are again separated spatially after passing the laser-plasma interaction, the developed short-pulse multiplexing setup will be used in combination with an imaging system to temporally probe the plasma expansion at the POLARIS laser system and thus to investigate the influence of pre-pulses and the generation of the target's backside sheath-field.

References

[1] K. Goda et al., "Serial time-encoded amplified imaging for real-time observation of fast dynamic phenomena," Nature 458, 1145 (2009).

[2] K. Nakagawa et al., "Sequentially timed all-optical mapping photography (Stamp)," Nature Photonics 8, 695 (2014).

[3] H. Mikami et al., Ultrafast optical imaging technology: principles and applications of emerging methods, Nanophotonics, 5, 497 (2016).

[4] M. Hornung et al., "54J pulses with 18nm bandwidth from a diode pumped chirped pulse amplification laser system", Optical Letters, 41, 5413 (2016).

First electron acceleration experiment at the JETI 100 laser system

S. Kuschel[1,2], *A. Seidel*[1,2], *C. Wirth*[1,2], *A. Sävert*[1], *M. B. Schwab*[1,2], *D. Hollatz*[1,2], *M. C. Kaluza*[1,2], *and M. Zepf*[1,2,3]

[1]Helmholtz Institute Jena, Fröbelstieg 3, 07743 Jena, Germany; [2]Institute for Optics and Quantumelectronics, Friedrich-Schiller-Universität of Jena, Max-Wien-Platz 1, 07743 Jena, Germany; [3]School of Mathematica & Physics, Queens University Belfast, BT7 1NN, UK

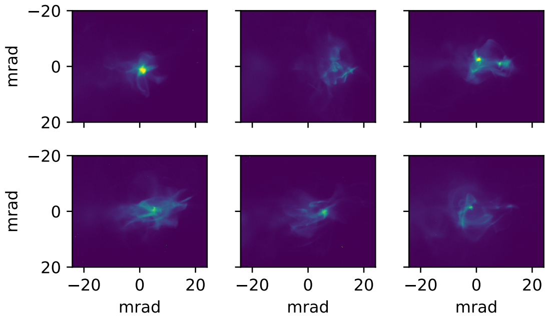

Figure 1: Consecutive beam profiles using a gas jet: The accelerated electron beam is strongly structured, has a large divergence and large pointing fluctuations.

The new JETI 100 laser system at the Helmholtzinstitute Jena has started operating last year. The system delivers laser pulses with 4 J before compression and 2.5 J on target at a pulse duration of sub 20 fs at $\lambda = 800$ nm. The maximum repetition rate is 5 Hz and the system has a peak power of 110 TW. Currently the first electron acceleration campaign is carried out with this new laser system.

The laser pulse is focused with an f/25 parabolic mirror into a gas target, which is either a gas jet or a gas cell. The pulse then drives a plasma wake inside the plasma and electrons can be accelerated in this traveling-wave-structure, called laser wake field acceleration (LWFA). The results show great advancements compared to the electron acceleration at the JETI 40 laser system: In comparison with a gas jet (fig. 1), a gas cell (fig. 2) has demonstrated ultra low divergence and very good pointing stability (each below 1 mrad RMS). An ongoing detailed analysis will yield exact values.

The highest electron energies of more than 600 MeV have been measured with an acceleration length of 11 mm (fig. 3). Using a longer plasma, only significantly lower electron energies have been measured, indicating dephasing of the electrons within the plasma wake. Increasing the electron energy further requires more laser energy at the current setup, which will be available after the scheduled installation of additional pump lasers this summer.

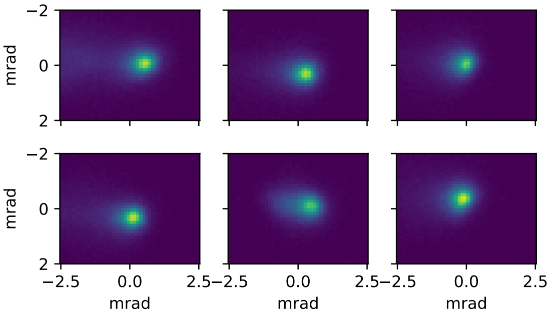

Figure 2: Consecutive beam profiles using a gas cell: The accelerated electron beam is ultra stable with a divergence and pointing stability of less than 1 mrad (RMS) each. Please note the scale change on the axis compared to fig. 1.

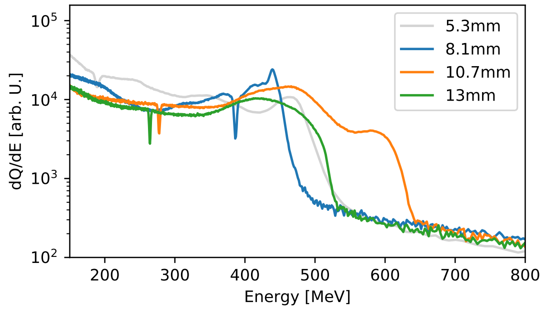

Figure 3: The resulting electron energies for different acceleration length of the gas cell: The maximum energy was measured at 11 mm acceleration length, reaching electron energies of more than 600 MeV (orange line). At the shortest acceleration length (5 mm) a smaller magnet spectrometer leading to a very low energy resolution. Therefore the maximum energy at 5 mm was most likely less than at 8 mm.

Femtosecond-probing at the JeTi-200 laser-system

C. Wirth[1], A. Sävert[2], M. B. Schwab[1], and M. C. Kaluza[1,2]

[1]Institute of Optics and Quantum Electronics, Jena, Germany; [2] Helmholtz-Institute Jena, Germany

We present a few-cycle probe beam system implemented on the JeTi-200 laser system for the investigation of relativistic laser-plasma interactions. By using a transverse pump-probe configuration a shadowgraphic image of a plasma wave structure in electron acceleration experiments was recorded.

In the process of laser wakefield acceleration (LWFA) electrons can be accelerated by the huge longitudinal electrics fields (> 100 GV/m) of a plasma wave structure [1].

To gain a deeper understanding into the physics underlying these acceleration processes and to improve the stability of electron acceleration in terms of pointing fluctuations, energy and charge one needs a diagnostic of the plasma wakefield with micrometer spatial and femtosecond temporal resolution.

Therefore a few-cycle probe beam system was implemented on the JeTi-200 laser system. The few-cycle pulses can be generated via spectral broadening in a gas-filled hollow-core fibre (HCF) [2] followed by a set of chirped mirrors (CM) temporally compressing the exiting pulses.

Depending on the filling-gas, its pressure and the incident laser pulse intensity, a spectrum spanning several hundred nm is achievable [3].

Experimental Setup

Figure 1 shows a diagram of the probe's setup. 3 % of the pump pulse's energy is picked off by a beam splitter creating a probe pulse intrinsically synchronized with the pump. After the reduction of the probe's beam diameter with an apodized-aperture a set of chirped mirrors (CM) temporally compresses the pulse and a 1.5-meter focal length lens focuses the beam into the entrance of the gas-filled HCF. Within this setup the probe's quadratic dispersion is controlled such that its shortest pulse duration is realized at the HCF entrance resulting in the highest possible intensity. The self-phase modulation in the gas filled fibre broadens the probe's spectrum enough to support sub-5 fs pulse durations.

After exiting the HCF the probe beam is collimated via a concave mirror and again passes a set of 4 CM and fused silica wedges to temporally compress the pulses and to achieve fourier limited pulse duration in the evacuated target chamber. With a delay stage the relative timing between the probe and pump can be adjusted in 10 µm (33 fs) steps.

For imaging the interaction between the JeTi-200 laser pulses and the plasma created from a gas target, a 10-times microscope objective (Mitutoyo M Plan Apo NIR 10x), an achromatic doublet (f = 250 mm) and a CCD (Basler avA2300-25gm, 5.5µm pixel size) is used resulting in a 12.5-times magnification and a resolution of 0,5µm / pixel.

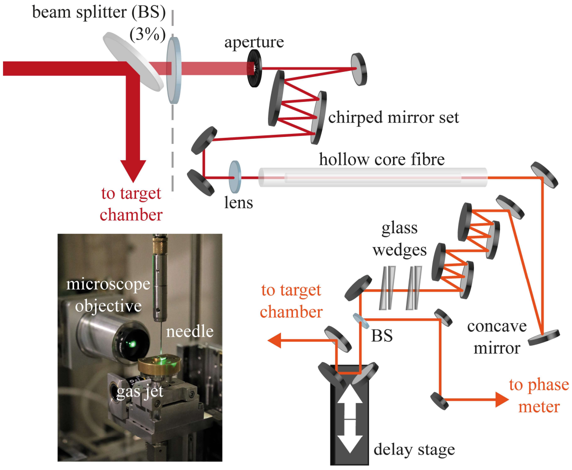

Figure 1: Schematic set-up of the few-cycle probe beam system. Inlet: Target set-up inside the vacuum chamber. The needle marks the focus position of the JeTi-200 beam.

Results

The probe setup's pulse duration was characterized using argon gas in the HCF and a stereo ATI phasemeter to measure the probe's pulse duration [4].

The best results for the available input pulse energy were achieved using a pressure of 200 mbar in the HCF resulting in a pulse duration of 5 fs on average and a pulse energy of (280 ± 9) µJ exiting the HCF.

These pulses were then used to image the laser-plasma interaction in a supersonic helium-gas jet with a backing pressure of 16 bar.

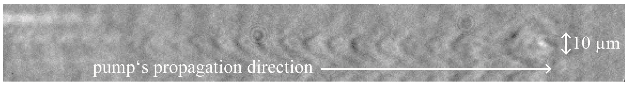

Figure 2: Shadowgraphic image of a plasma wave propagating from left to right.

Figure 2 shows a shadowgraphic image of a plasma wave driven by a high intensity JeTi-200 laser pulse.

The image proves that the few-cycle probe pulse system is a powerful diagnostic tool for gaining a deeper insight into wakefield acceleration physics.

References

[1] T. Tajima et al., Phys. Rev. Lett. 43 (1979)
[2] M. Nisoli et al., Appl. Phys. Lett. 68 (1996)
[3] M. B. Schwab et al., Appl. Phys. Lett. 103 (2003)
[4] D. Adolph et al., Appl. Phys. Lett. 110 (2017)

Measurement of Harmonic Wavefronts

R. McHugh[1,3], *L. Li*[2,3], *K. Chaitanya*[3], *C. Rödel*[3], *A. Sävert*[1,3] *and M. Zepf*[1,2,3]

[1]Institut für Optik and Quanteneletronik, Friedrich-Schiller-Universität Jena, Max-Wien-Platz 1, 07743 Jena, Germany.

[2]Department of Physics and Astronomy, Queens University Belfast, Belfast BT7 1NN, UK.

[3]Helmholtz Institute Jena, Fröbelstieg 3, 07743 Jena, Germany.

Using an adaptive optic and plasma mirror system, the JETI-200 laser produces a nearly diffraction limited high intensity spot. The resultant intensity distributions and wave front values of the high harmonics (HHG) generated can then be directly measured using a high numerical aperture (NA = 0.1) Hartmann wave front sensor. Such measurements allow a comparison of the spatial phase the distinct HHG processes based on the Relativistic Oscillating Mirror (ROM) and Coherent Wake Emission (CWE) and carry detailed information about the surface dynamics. The detailed understanding will contribute towards the development of bright single attosecond pulses and enhanced HHG using multi- colour fields[1].

Introduction

The phenomenon of HHG has been the backbone of a plethora of new developments within the field of laser-matter interaction in recent years[2]. An initially solid target is irradiated by a sufficiently intense laser pulse, and the rising edge quickly transforms the surface into a hot plasma. The electrons on this surface will be accelerated by the laser field, reaching relativistic velocities and periodically emit an atto-second XUV pulse each optical cycle. At least two distinct harmonic emission processes co-exist under such conditions. At sufficiently high intensities the Relativistic Oscillating Mirror (ROM) mechanism becomes dominant ($\sim 10^{16} Wcm^{-2}$), where the plasma response to the laser field becomes extremely nonlinear and the incident laser light is periodically Doppler-upshifted upon reflection from the oscillating vacuum-plasma boundary. By contrast, Coherent Wake Emission (CWE) requires much lower intensity ($\sim 10^{16} - 10^{18} Wcm^{-2}$) and occurs when the oscillating electrons return and excite strong oscillations in the density gradient which in turn emits HHG. The two are characterised by their intensity dependent emission phase, and this spatial phase has been found to have a major impact on the divergence of the harmonic beams[3]

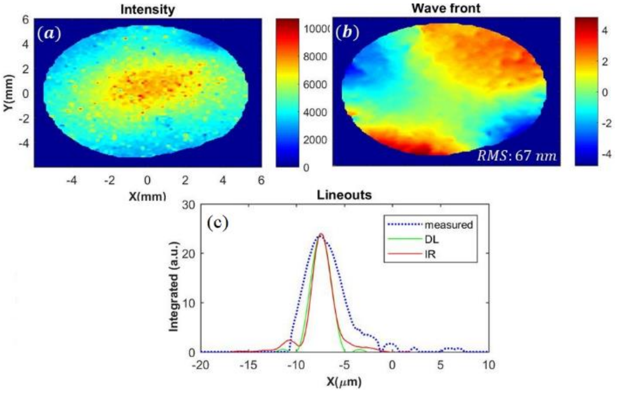

Figure 1: A CWE dominated harmonic; subplots (a, b) show the intensity and spatial structure, and the phase delay across the wave front in units of λ. (c) shows the integrated lineouts of 3 retro propagated foci, measured signal, a synthesised flat phase signal and the IR laser focus.

Experiment

Set-up

The Jeti-200 laser using a maximum energy of ~500mJ after compression and a single plasma mirror, was focused using a f/2.6 off-axis parabola into a 2.3µm FWHM spot on a fused silica target and a translatable multilayer XUV mirror is used to reflect the chosen harmonic toward the Hartmann wave front sensor[4]. The sensor consists of an aperture array mounted a small distance from the detection plane. Each aperture acts as an optical lever, displacing each diffracted spot a distance proportional to the average phase shift across it. This enables the sensor to measure the tilt over each aperture by comparing the measured positions of the diffracted spots to a reference beam spot array. Two meshless aluminium filters were installed between target, multilayer mirror and Hartmann sensor to reduce the secondary source generation on the multilayer mirror and the protect the cooled vacuum X-ray CCD of the sensor.

Analysis

We utilised two XUV mirrors for this study, one with a 33.5nm centre wavelength, to select the ~24th harmonic, ensuring the ROM process dominated, the other 44.4nm which extracted the ~18th harmonic, by referencing our XUV spectrometer and slightly varying the on-target focus, the CWE regime could also be guaranteed. The data was analysed using Imagine optic's HASO wave front analysis software, Fig. 1(a, b), allowing the source intensity shape and phase distribution to be reconstructed by retro-propagation Fig. 1(c). The CWE harmonics have noticeable astigmatism and allow an effective source size of the order of the laser focus to inferred.

References

[1] M. Yeung, et al. Nat. Phot. 11, 32-25 (2016).
[2] A Leblanc, et al. Nat. Phys. Lett. 12, 301-305 (2016).
[3] F. Quéré, et al. Phys. Rev. Lett. 100, 095004 (2008).
[4] P. Mercere, et al. Opt. Lett. 28, 1534 (2003).

Towards the indirect observation of the laser pulse evolution in a plasma

M. Reuter[1,2]*, M.Leier, E. Siminos*[3]*, A. Sävert*[1,2]*, and M. C. Kaluza*

[1]IOQ, Jena, Germany; [2]HIJ, Jena, Germany; [3]Chalmres University, Gothenburg, Sweden.

Ultra-short optical probing is a powerful tool to investigate the dynamics of a laser wakefield accelerator. Using few-cycle probe pulses, the evolution of the plasma wave can be investigated via shadowgraphy[1]. Furthermore, polarimetry measurements exploiting the Faraday and the Cotton-Mouton effect allow for the high-resolution detection of the magnetic fields inextricably connected to laser wakefield acceleration [2,3]. By combining both methods, deeper insight into the acceleration processes can be gained.

In the experiment, carried out with the Jeti-40 laser at the IOQ and HI Jena, the main pulse propagating in x-direction generates a plasma from a pulsed helium gas jet and excites a plasma wave which co-propagates with the main pulse. Electrons trapped in the negative half cycle of the plasma wave can be accelerated to velocities close to the speed of light, c. With the ultra-short probe pulse and its high resolution imaging system, snapshots of the plasma wave are recorded. Moreover, a polarizer in the probe beam's path after the interaction helps to identify the change of polarisation of the probe beam acquired in the magnetic fields in the region of interaction. Magnetic fields oriented parallel to the probe beam's direction of propagation rotate the plane of polarisation via the Faraday effect by an angle ψ which for a probe beam propagating in y-direction and initially polarised in x-direction manifests itself in the generation of an electric field component in z-direction. Furthermore, perpendicular magnetic fields introduce a phase shift δ between the probe pulse's two electric field components (Cotton-Mouton effect). Within the frame of laser wakefield acceleration, azimuthal magnetic fields are generated both by the plasma wave's displacement currents and the accelerated electrons. Those azimuthal fields can be decomposed into a component parallel to the propagation direction of the probe pulse (y) and a perpendicular component (z). Moreover, the perpendicular component is superimposed by the more than one order of magnitude stronger oscillating magnetic fields of the laser pulse. The intensity of the probe beam transmitted through a polariser $I_{pol} = I_{pol}(\delta, \psi)$ contains information both on ψ and δ, i.e. the separation of both parameters from experimental data involves an extensive experimental setup. For the sake of experimental simplicity, we chose an initial setup designed to retrieve the combined angle $\vartheta_{\delta,\psi}$, which represents the rotation of the polarisation ellipse and can be obtained by inverting Eq.1 under the assumption δ = 0. Fig. 1 compares experimentally obtained (left-hand side) and Particle-In-Cell (PIC)-simulated (right-hand side) rotation maps $\vartheta_{\delta,\psi}(x,z)$. While the rotations maps detected early in the interaction (top) could be explained by pure Faraday rotation [2,3], the bottom rotation maps representing a later stage during the interaction are more complex and suggest an additional influence of the Cotton-Mouton effect and hence, the pump laser pulse's magnetic field.

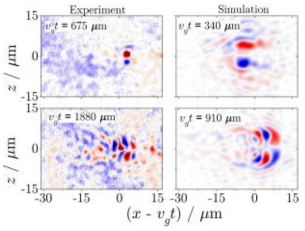

Figure 1: Angle of rotation $\vartheta_{\delta,\psi}$ in experiment (left-hand side) and simulation (right-hand side).

We will now explore two scenarios, S1 and S2, which will help to understand the effect of ψ and δ on $\vartheta_{\delta,\psi}$ and therefore, support the above assumption. In Fig.2 all black lines are related to S1 while dashed orange lines correspond to S2. With pre-determined distributions of ψ and δ (Fig.2a), the intensity transmitted through the two polarisers are computed (Fig.2 b) and the angle $\vartheta_{\delta,\psi}$ (Fig.2 c) is retrieved by inverting the intensity distribution under the assumption δ = 0. Since this assumption holds for S1 , the intensity distribution is uniform and the retrieved angle $\vartheta_{\delta,\psi}$ is identical to the angle of rotation ψ. However, for S2, δ ranges between 0° and 180°, which results in an alternating intensity distribution, which is transferred to $\vartheta_{\delta,\psi}$ as an alternating sense of rotation.

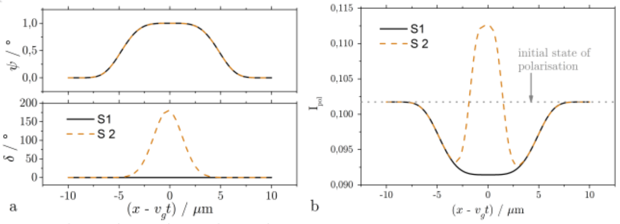

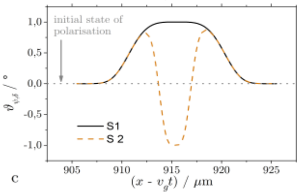

Figure 2: Dependence of $\vartheta_{\delta,\psi}$ on ψ and δ presented in two scenarios S1 and S2.

Hence, the scenario S1 can explain the rotation maps obtained early in the interaction by pure Faraday rotation while S2 is required to describe the generation of the later rotation map as a consequence of an interplay of Faraday rotation and the Cotton-Mouton effect.

Due to the sub-plasma wavelength resolution of the ultra-short probe pulse and its imaging system, we could observe an influence of the strong magnetic fields of the laser pulse on the probe beam's state of polarisation and thus, pave the way for the optical observation of laser pulse evolution in a plasma.

References

[1] M. C. Kaluza et al., PRL 105 (11), 2010
[2] A. Sävert et al., PRL 155 (5), 2015
[3] A. Buck et al., Nat.Phys. 7 (7), 2011

Longitudinally-polarized terahertz pulse generation from laser-overdense plasma interactions

A. Woldegeorgis[1,2#], T. Kurihara[3], M. Almassarani[1,2], R. Größe[1], B. Beleites[1], F. Ronneberger[1], G. G. Paulus[1,2] and A. Gopal[1,2]

[1]Helmholtz-Institut Jena, Germany; [2]IOQ-Universität Jena, Germany; [3]Univesität Konstanz, Germany

Focusing a radially polarized beam, compared to a linearly polarized beam, creates a strong and tightly focused longitudinal field [1]. Recently, it has been demonstrated that longitudinal terahertz (THz) fields have a promising potential in particle acceleration [2]. Here we report on the generation and detection of longitudinally polarized THz pulses with field strength two orders of magnitude higher than the highest field strength demonstrated so far.

High-power broadband THz radiation can be generated when intense laser pulses interact with matter. When the intensity of the laser pulse is higher than the ionization potential, plasma is generated. The charged particle dynamics and the resultant quasi-static fields and currents generated inside the plasma can give rise to broadband electromagnetic radiation ranging from x-rays to THz radiation. We studied the radially polarized THz radiation generated by the transient dynamics of charged particles exiting the target rear surface. The generation processes are discussed extensively in [3].

The experiment was conducted at the JeTi40 laser system which delivers pulses of 30 fs duration at a center wavelength 0.8 µm with on-target energy of 650mJ. The laser pulses were focused by an f/1.2 45° off-axis parabola (OAP) onto thin metal foils to a FWHM spot area of $10\mu m^2$ producing intensities $>5x10^{19}$ W/cm^2. The THz radiation generated at the back side of the target is predominantly emitted in the noncollinear directions with respect to the target normal. The radiation was collected by an ellipsoidal reflector, and a set of reflective optics collimates and steers it out of the interaction vacuum chamber towards the THz diagnostics. Noncollinear pump-probe electrooptic (EO) technique was deployed to estimate the peak electric field and study the temporal and spectral properties of the THz pulses [3].

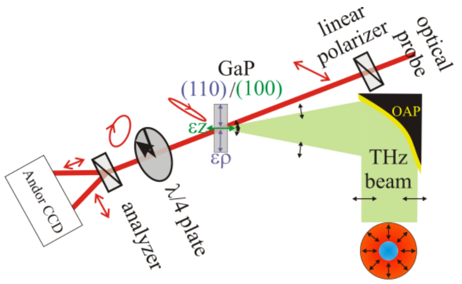

Fig. 1: Experimental layout.

As shown in the experimental layout, depicted in Fig. 1, the collimated THz beam is focused, by an f/1.5 OAP (NA=0.33), onto the gallium phosphide (GaP) EO crystal. 100 µm and 500 µm thick GaP crystals cut in <110> and <100> planes were employed to measure the transverse/radial (εr) and the longitudinal (εz) field components respectively. Broadband attenuators were inserted in the beam path so that the birefringence induced in the EO crystal by the THz pulse is purely electronic.

A longitudinally polarized THz pulse with field strength of 0.15 GV/m and a transverse component with field amplitude in excess of 0.3 GV/m were measured at the focus of the THz beam (Fig. 2a). Inset of Fig. 2a shows the corresponding spectral amplitudes. The longitudinal-to-transverse electric field strength ratio of 0.5 is slightly higher than the theoretical value (≈ 0.43) calculated for an input field which is perfectly collimated, purely radially polarized with homogeneous beam profile, and focusing parameters of the optics used in this experiment. In principle, stronger longitudinal fields could be achieved by employing a high NA focusing optics [4].

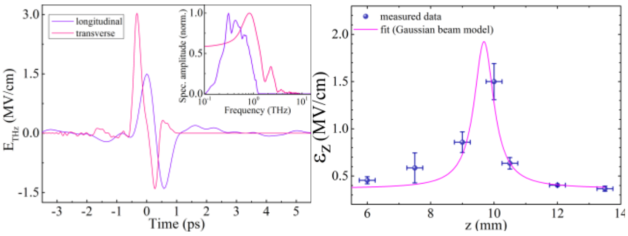

Fig. 2: a) Temporal waveform of εr and εz. Inset shows the corresponding spectral amplitudes. b) Longitudinal electric field amplitude εz for different axial positions of the GaP crystal.

Furthermore, a phase difference of π/2 between the two components, which is universal [5], can be observed from their temporal profiles. A z-scan was performed by translating the GaP crystal along the THz beam propagation direction in order to determine the nominal focal position and to study the evolution of the amplitude and phase of the longitudinal field component through the focal plane (Fig. 2b). Such a powerful longitudinal field will find numerous exciting applications in terahertz as well as particle accelerator physics.

References

[1] Dorn, R. et al., Phys. Rev. Lett. 91, 23901 (2003)
[2] Nanni, E. et al., Nat. Commun. 6, 8486 (2015).
[3] Gopal, A. et al. Phys. Rev. Lett. 111, 074802 (2013); Gopal, A. et al. New J. Phys., 14, 083012 (2012); Herzer, S. et al. New J. Phys., accepted (2018).
[4] Youngworth, K.S. et al., Opt. Express 7, 77 (2000).
[5] Winnerl, S. et al., New J. Phys. 14, 103049 (2012).

[#] abel.woldegeorgis@uni-jena.de

Raising the injection threshold in Laser Wakefield Accelerators by avoiding microscopic density ripples

S. Kuschel[1,2], *M. B. Schwab*[1,2], *W. Ziegler*[1,2], *M. Yeung*[1], *D. Hollatz*[2], *A. Seidel*[2], *A. Sävert*[1,2], *M. C. Kaluza*[1,2], *and M. Zepf*[1,2,3]

[1]Helmholtz Institute Jena, Fröbelstieg 3, 07743 Jena, Germany; [2]Institute for Optics and Quantumelectronics, Friedrich-Schiller-Universität of Jena, Max-Wien-Platz 1, 07743 Jena, Germany; [3]School of Mathematica & Physics, Queens University Belfast, BT7 1NN, UK

Laser wake field accelerators (LWFA) have shown the potential to accelerate electrons over cm-scales distances to GeVs of energy[1]. It holds the promise to provide accelerated electrons for different kinds of secondary experiments while still being an affordable tool for university sized labs. While the maximum energy of laser accelerated electrons has been continuously increased, accurate control over the spectral shape and particularly the spectral bandwidth of the electrons still need to improve to match the requirements for many secondary experiments.

The slow down of the phase velocity of the plasma wake (β_p) is a neccessary requirement for wave breaking to occur. This slow-down depends on the plasma density but also a plasma density gradient (down-ramp). We have identified the gradient as the leading contribution in gas jets:

$$\beta_p = 1 - \underbrace{\frac{1}{2}\frac{\omega_p^2}{\omega^2}}_{0.3\%} - \underbrace{\frac{\omega_p^2}{\omega^2}}_{0.6\%} - \underbrace{\frac{\partial \lambda_p}{\partial z}}_{\substack{\text{jet: } \sim 3\% \\ \text{cell: } < 0.25\%}}$$

with the laser frequency ω, the plasma frequency ω_p, the co-moving coordinate ζ and the plasma density n_e. The transverse probing pictures (Shadowgrams), which resolve the plasma wave with an unprecended precision ([2]) also allow to infer the plasma density variations on a micron scale. The data show, that density downramps due to an inhomogeneous plamsa density profile are the leading contribution the slow down of the phase velocity of the plasma wake rather than dispersion and etching alone. Consequently these variations also act as the main trigger for wave breaking and therefore the self-injection process in the gas jet.

The accelerated charge (fig. 1) in the gas jet (orange) and the gas cell (green) demonstrates the suppression of wave breaking, while plasma wakes could still be observed by transverse probing [2].

Our findings are reproduced by 3D PIC simulations (fig. 2) revealing their major influence on the injected charge.

References

[1] W.P. Leemans et al., PRL 113, 24 (2014)

[2] M.B. Schwab et al., APL 19, 103 (2013)

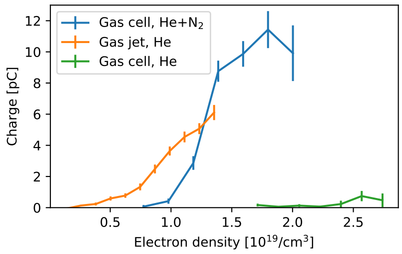

Figure 1: Accelerated charge as a function of the electron density for different target configurations. The onset of the electron injection for the gas jet was measured to be at $n_e \approx 0.8 \cdot 10^{19}/cm^3$ (below that density the appearance of an electron beam was highly unstable), corresponding to $P/P_c = 1.8$. Using the gas cell with pure He even for densities up to $n_e = 2.75 \cdot 10^{19}/cm^3$, corresponding to $P/P_c = 5.5$, no electron acceleration could be observed. The measured charge for the highest density is caused by a very diffuse background without any beam-like structures visible.

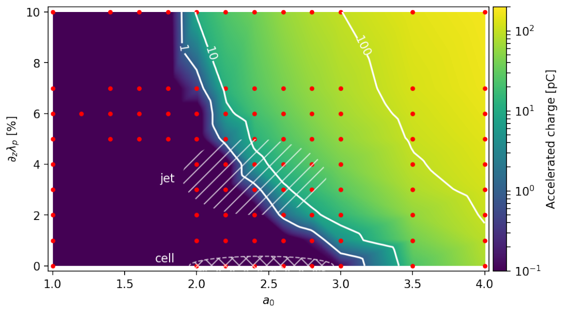

Figure 2: Accelerated charge in pC depending on the input a_0 of the laser pulse and the gradient of the plasma downramp $\partial_z\lambda_p$. A 3D PIC simulation has been carried out for every red dot shown while color scale and contour lines are interpolated from the simulation data. The threshold for wave-breaking is indicated by the onset of the color scale at 0.1 pC. In addition contour lines at 1 pC, 10 pC and 100 pC are shown. The sudden onset of the injection process is clearly visible. The typical operating range of gas jet and gas cell are also indicated separating the different regimes.

Upgrade of back-reflection diagnostic based on frequency-resolved optical gating at PHELIX*

J. Hornung[1,2], *V. Bagnoud*[1,2], *M. Zepf*[2,3,4]

[1]GSI, Darmstadt, Germany, [2]Helmholtz-Institut Jena, Germany, [3]Institut für Optik und Quantenelektronik, Friedrich-Schiller-Universität Jena, Germany, [4]School of Mathematics and Physics, Queens University Belfast, UK

Motivation

During the interaction of an ultra-intense laser pulse with sub-micrometer thin foils, complex effects on the femtosecond timescale take place. During this interaction, a part of the laser pulse is transmitted via hole boring and another is reflected back at the position of the cirtical plasma density. Both reflected and transmitted pulses are modulated due to effects like relativistic self-phase-modulation, while the spectrum of the reflected pulse is additionally Doppler-shifted by the moving critical plasma density happening during hole boring. To study these effects and timescales a diagnostic for back-reflected light based on frequency resolved optical gating (FROG) [1] has been developed and implemented at the PHELIX facility [2]. The FROG consists of a single-shot autocorrelator and an imaging spectrometer which spectrally and temporally resolves the incoming laser pulse. To achieve more reliable results the existing diagnostics has been upgraded.

Upgrade

One part of the upgrade is the change of the spectrometer setup. To keep the device as small as possible, a crossed Czerny-Turner-spectrometer was used in the first setup. Short focal-length mirrors and large reflection angles inside the spectrometer lead to strong aberrations, mostly astigmatism, that strongly influence the spectral resolution and spacial homogeneity of the two-dimensional spectrometer. To reduce the aberrations the focal length of the mirrors has been doubled, from 100 mm to 200 mm and the reflection angles could be reduced from 25 and 20 degree to roughly 16 and 12 degrees. The result of this change can be seen in figure 1. which shows the spectral lines of a calibration lamp. The corresponding sum of the spectrum in yellow, for the previous (a) and new (b) configuration, shows narrower lines.

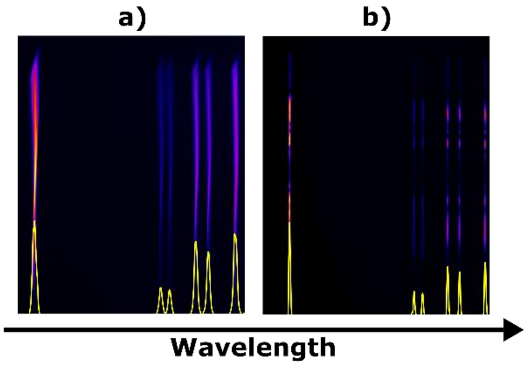

Figure 1: Spectrum of a calibration lamp and the corresponding sum over the complete image in yellow for the old (a) and new (b) spectrometer setup.

This changes the resolution from roughly 1 nm to below 0.5 nm with a much more homogeneous resolution over the whole image.

A further problem, detected during the commissioning of the device, was a slight asymmetric FROG-trace in the delay axis, shown in figure 2 a), which was produced due to misalignment of the autocorrelator and a beamsplitter with a non-equal transmission and reflection ratio. After changing the beamsplitter and realigning the autocorrelator the FROG-trace symmetry in the delay axis could be improved, as shown in figure 2b).

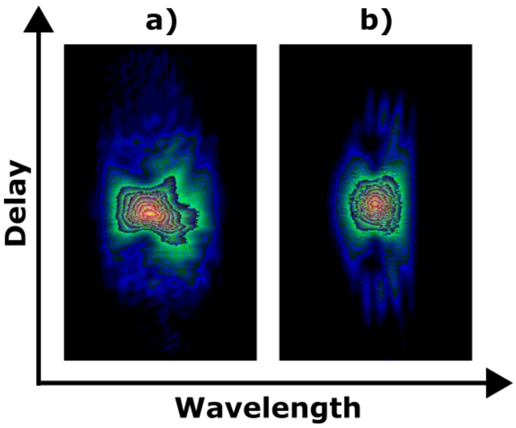

Figure 2: FROG-trace before (a) and after (b) the change of the beamsplitter and realignment of the autocorrelator.

This symmetry improvement increases the accuracy of the pulse-reconstruction algorithm [3] which therefore leads to more reliable measurements.

Conclusion

The upgrade of the back-reflection diagnostic lead to a more symmetric and spectrally better resolved FROG-trace which will produce more reliable data in upcoming experiments.

References

[1] D. J. Kane and R. Trebino, IEEE Journal of Quantum Electronics **29**, Issue 2 (1993) 199311

[2] F. Wagner, J. Hornung, C. Schmidt, et al., Review of Scientific Instruments **88** (2017) 023503

[3] K. W. DeLong, R. Trebino, J. Hunter, et al., Journal of the Optical Society of America B, **11** (1994) 002206

---

* This report has also been published in "GSI Scientific Report 2017".

Moderation of a laser-generated neutron beam at PHELIX

A. Kleinschmidt[1,2]*, S. Aumüller*[3]*, V. Bagnoud*[1]*, D. Jahn*[3]*, V. A. Schanz*[3]*, M. Zimmer*[3]*, and M. Roth*[3]

[1]GSI, Darmstadt, Germany; [2]HI Jena, Jena, Germany; [3]IKP, TU Darmstadt, Germany

Introduction

The PHELIX laser at GSI is one of the leading petawatt short pulse systems in the world. It provides peak energies of 200 J within pulse lengths of about 500 fs and peak intensities above 10^{20} W/cm^2. The high contrast of the system of 10^{12} [1] allows the investigation and application of acceleration mechanisms that require thin targets, as it is the case e.g. for ion acceleration in the relativistic transparency regime.

One of these applications is a laser-driven neutron source [2,3], which is based on the conversion of laser-accelerated ions into neutrons via nuclear reactions inside a converter material (catcher). Depending on the reaction, neutrons get emitted spatially homogeneous or in a directed neutron beam. The latter is more pronounced in the case of deuteron break-up reactions inside the catcher. To enhance the acceleration of deuterons from a deuterated polymer target, thicknesses of a few 100 nm are used which represents merging into the regime of relativistic induced transparency.

The energy spectrum of a laser-based neutron source is exponentially decaying to cutoff energies of several 10 MeV. Nevertheless, many applications, like resonance spectroscopy, scattering experiments, and resonance imaging, require a high flux of low-energy neutrons in the range of 0.1 eV to 100 keV. In order to adapt laser-based neutron sources to these applications, a moderating material is used to slow down the high-energy component of the spectrum. As the moderator temporally spreads the neutron pulse due to multiple scattering, its design is crucial for a successful measurement and should be adjusted for every new experiment or application.

Neutron moderation at PHELIX

In a first proof of principle experiment conducted at the Trident laser facility at LANL, the moderation of laser-based neutrons has already been successfully demonstrated [4,5]. However, the setup, especially the catcher-moderator design was far from the optimum regarding emitted neutron yield and temporal spread of the neutron pulse.

For the moderation of a laser-based neutron beam at PHELIX, the used setup was optimized, first in FLUKA simulations, and later during the experiment itself. Figure 1 shows the new moderator design as a result from simulations (left). The beryllium catcher was placed inside a high density polyethylene (HDPE) moderator. It is narrow in line of sight to the main detector (indicated by a green arrow), which significantly reduces the temporal spread of the neutron pulse. The main difference to the previous Trident setup is an addition of material at the moderator sides in the direction of the incoming ion beam (indicated by a violet arrow). These two "wings" increase the neutron yield from the catcher-moderator configuration by slowing down neutrons emitted in this direction. Furthermore, the moderator is long in the direction of the impinging ions propagation path to slow down a large part of the high-energy component of the neutron spectrum. The right-hand side of Figure 1 shows the addition of material during the PHELIX experiment.

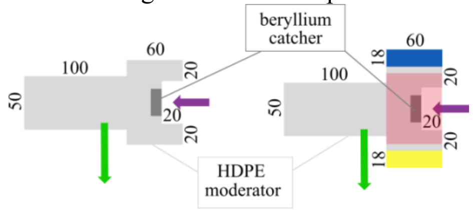

Figure 1: By simulations optimized moderator (left) and addition of material during the experiment (right).

Figure 2 represents a comparison of the fast and thermal neutron yield for increasing moderator thickness. Starting with the FLUKA simulation, 18 mm HDPE were added first to one wing (indicated in yellow in Fig. 1), then additionally to the other one (blue block in Fig. 1). Finally another 20 mm HDPE were placed on top of the moderator (marked red in Fig. 1). It is clearly visible that the thermal neutron yield only exceeds the fast one for the setup with the thickest moderator, whereas the absolute thermal neutron maximum could be achieved by adding 18 mm HDPE to one side of the moderator (yellow). However, as the experiment took place in December 2017, these are preliminary results. Furthermore, the influence of the moderator setup on the temporal broadening of the neutron pulse still has to be investigated.

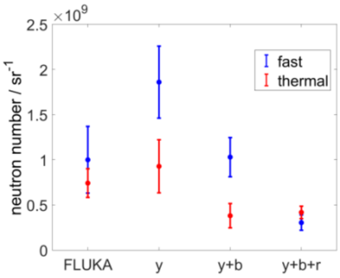

Figure 2: Neutron yield for fast (blue) and thermal (red) neutrons. The x-axis represents different moderator setups with increasing HDPE thickness. The labels y for yellow, b for blue, and r for red are referring to the highlighted blocks in Figure 1 (right).

References

[1] V.A. Schanz et al., Opt. Express 25, 8 (2017)
[2] D. Jung et al., Phys. Plasmas, 20, 056706 (2013)
[3] M. Roth et al., Phys. Rev. Lett., 110, 044802 (2013)
[4] A. Kleinschmidt, PhD thesis, TU Darmstadt (2017)
[5] A. Kleinschmidt et al., GSI scientific report 2016, p. 281 (2017)

Relativistic interaction of mid-infrared laser pulses with nanowire targets: towards a novel laser-plasma interaction regime

Z. Samsonova[1,2], S. Höfer[1], V. Kaymak[3], S. Ališauskas[4], V. Shumakova[4], A. Pugžlys[4], A. Baltuška[4], T. Siefke[1], S. Kroker[5], O. Rosmej[6], A. Pukhov[3], I. Uschmann[1], C. Spielmann[1,2], and D. Kartashov[1]

[1]IOQ & IAP, Friedrich-Schiller-University Jena, Germany; [2]Helmholtz Institute Jena, Germany; [3]Heinrich-Heine-University Düsseldorf, Germany; [4]Vienna University of Technology, Austria; [5]LENA, Technical University Braunschweig, PTB, Germany; [6]GSI, Darmstadt, Germany.

In this report we present the results of the investigation of the relativistic mid-infrared laser pulses with silicon targets. The novelty of this regime lies in the scaling of the interaction parameters such as plasma critical density and normalized vector potential with the wavelength [1]. It also means that for mid-IR pulses the ionization happens in the tunnel regime, which in contrast to one/multiphoton ionization allows sharp plasma density gradients. These new features strongly influence the parameters of created plasmas, thus, generated X-ray emission. The use of nanostructured targets may additionally enhance the effect due to the high laser energy absorption shown in earlier works [2-4]. In order to investigate the possibility to generate extreme plasma states we compare the line emission spectra and bremsstrahlung emission generated from the polished and nanowire targets, and apply PIC simulations together with kinetic FLYCHK code to match our experimental findings and the theoretical predictions.

Experiment & Results

The p-polarized idler beam of OPCPA laser system (TU Vienna) with energy of 25 mJ is focused under 45° onto the samples resulting in the peak intensity of nearly 10^{17} W/cm^2 with a pulse duration of 90 fs. The generated X-ray emission is then detected with the crystal spectrometer and the Timepix detector in a single shot. It is shown, that the intensity of the K-shell emission from neutral atoms as well as the hard X-ray bremsstrahlung are comparable for polished and nanowire (NW) targets. However, the efficiency of the line emission from highly charged ion states differs dramatically. In case of the polished sample there is essentially no emission from the transitions in He- and H-like Si observed (Fig. 1). This means that the electron density and bulk electron temperature are higher for the NW target. Similar behaviour has been observed in our previous experiments with ZnO targets irradiated by a frequency doubled pulses of Ti:Sapphire system [5].

Simulations & Discussions

To estimate the achieved plasma parameters we attempted to fit the experimental X-ray spectra with the synthesized ones using the temporal evolution of the parameters predicted by the PIC code. In case of NWs, the bulk electron temperature reaches its maximum value in the keV range by the end of the laser pulse, while the electron density exceeds solid density in the whole volume of nanowires. Corresponding X-ray line emission spectrum matches well to the hot part of the experimental spectra (Si^{12+}-Si^{13+}). The PIC simulations for the polished target are more troublesome requiring an inclusion of the spatial distribution of the laser intensity (not a plane wave) and higher resolution. However, assuming similar time scale for plasma cooling and its recombination and introducing a two-parameter search over the maximum bulk electron temperature and density we achieve a good agreement between the simulations and the experimental results for the maximum electron density about 10^{23} cm^{-3} and the bulk temperature of several hundred eV. The severe difference may arise from the larger penetration depth and higher absorption of the laser pulse within the NWs. Remarkably, the predicted electron density exceeds the critical density calculated for the used mid-infrared pump by 3 orders of magnitude.

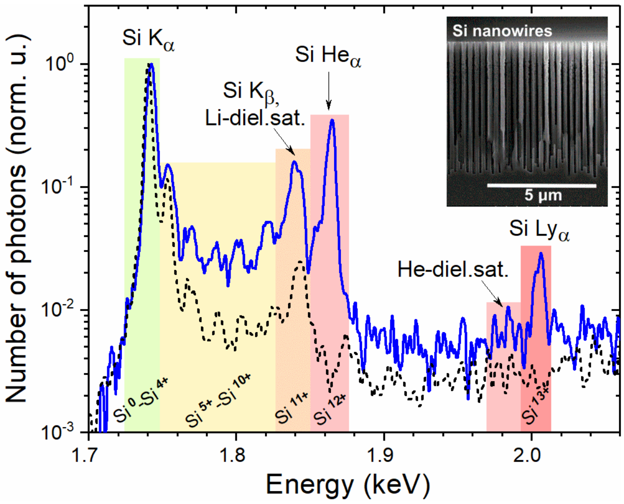

Figure 1: K-shell emission spectra for the polished (black dashed) and the NW (blue solid) Si targets. Inset: SEM image of the NW array.

Our studies demonstrate that relativistically intense ultrashort laser pulses in mid-IR spectral range are capable to generate solid density and keV-temperature plasmas and using NW targets may significantly increase the efficiency of the impact ionization and plasma heating.

References

[1] J. Weisshaupt et. al., Nat. Phot. 8, 927-930 (2014).
[2] T. Nishikawa et. al., Appl. Phys. B 78, 885 (2004).
[3] S. Mondal et. al., Phys. Rev. B 83, 035408 (2011).
[4] M. A. Purvis et. al., Nat. Phot. 7, 796-800 (2013).
[5] Z. Samsonova et. al., AIP Conf. Proc. 1811, (2017).

*This report is also submitted to the GSI Scientific Report 2017.

Optimization of laser based sources of electrons and gammas for backlighting of high areal density targets at FAIR

Ş. Zähter[1]*, O. Rosmej*[2]*, N. Andreev*[3]*, L. Borisenko*[4]*, N. Borisenko*[4]*, B. Borm*[1,2]*, P. Christ*[1]*, F. Horst*[2,5]*, D. Khaghani*[6,7]*, P. Neumayer*[2]*, V. Pimenov*[8]*, L. Pugachev*[3]*, K. Schmal*[1]*, C. Wagner*[1]*, N. Zahn*[1]*, K. Zerbe*[1]*, J. Jacoby*[1]*, APPA-HED@FAIR, Plasmaphysics/PHELIX*

[1]Institute for Applied Physics, Goethe University, Frankfurt, Germany; [2]GSI, Darmstadt, Germany; [3]Joint Institute for High Temperatures, RAS, Moscow, Russia; [4]Lebedev Physical Institute, RAS, Moscow, Russia; [5]Justus Liebig University Giessen, Giessen, Germany; [6]Friedrich Schiller University Jena, Jena, Germany; [7]Helmhotlz Institute Jena, Jena, Germany; [8]Zelinsky Institute of Organic Chemistry, RAS, Moscow, Russia

Laser-based intense and well-directed beams of MeV electrons and γ-rays are being investigated for their application in backlighting states of matter with high areal density. In order to optimize the properties of the secondary sources when the laser parameters cannot be changed, one can modify the structure of near critical density targets. Simulations demonstrate that the interaction of a relativistic laser pulse ($4 \cdot 10^{19}\ \mathrm{W/cm^2}$) with a near critical plasma layer ($10^{21}\ \mathrm{cm^{-3}}$) leads to the effective generation of highly energetic electrons (>10-20 MeV) carrying a charge that exceeds predictions from ponderomotive scaling by at least two orders of magnitude [1]. At the time of the ns-prepulse, electrons accelerated from the pre-ionized low-density foam target with a thickness of 500 µm have the highest energies and the highest charge (ca. 25 nC for electrons with energies higher than 30 MeV). A significant increase of the electron number with energies of tens of MeV makes such kind of laser-based electron sources a high potential diagnostic tool for high areal density HED states. In this work, we present the first pilot experiments on the characterization of MeV electron beams generated by the interaction of the PHELIX-laser pulse with CHO-foams of 2 mg/cc density (P138, October 2017).

Electron spectra up to 100 MeV were measured using dipole magnets as dispersive elements. The electrons follow a certain path in the spectrometer according to their kinetic energy and the radius of gyration. This dispersion was calculated for our spectrometer. FUJI Film BAS-TR imaging plates were used as detectors. The response function of the imaging plates is known for photons, electrons and several other heavier particles [2]. A schematic of the electron spectrometer is shown in Figure 1.

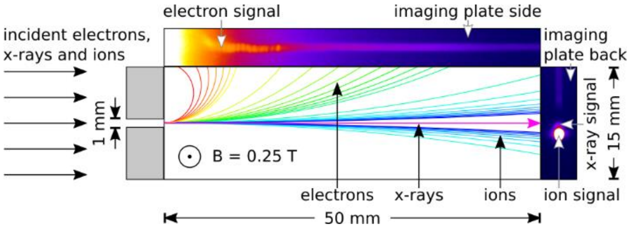

Figure 1: Schematic view of the electron spectrometer. Data in false-color images. Image by Ş. Zähter.

The interaction of the high power laser pulse of relativistic intensities with different target materials allow for the generation of MeV electrons. Ponderomotive scaling laws predict an electron temperature of 2.1 MeV for the effective laser intensity. In experiments with near critical plasmas, the production of intense MeV electron beams was demonstrated. Figure 2 shows the cumulative number of electrons with energies above detection threshold. Compared to the laser shot onto the Cu-foil (shot 30, black and red solid lines), corresponding to the usual way for laser-based particle acceleration, the interaction of relativistic laser pulses with pre-ionized low density plasmas of near critical density led to a strong increase in electron number with energies above 10 MeV (green solid line, shot 44).

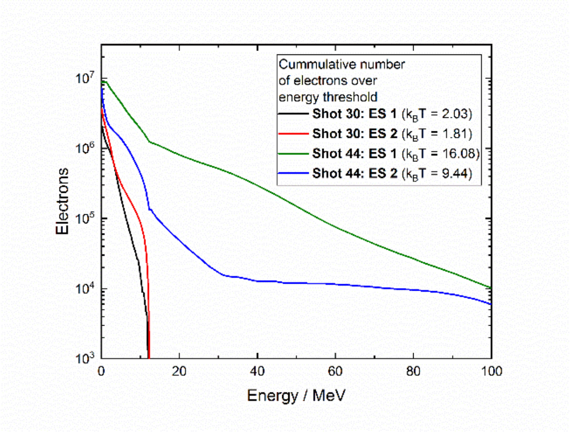

Figure 2: Cumulative number of electrons with energies above detection threshold. Image by Ş. Zähter.

Electrons are mostly accelerated in the laser direction reaching a mean energy of 16 MeV. Hot MeV electrons interacted with a 17 mm thick Fe-flange and created hard bremsstrahlung radiation measured by means of a ten channel TLD-spectrometer [3]. The radiation dose on the TLD-cards showed the same results as the electron spectrometers, namely a 10-100-fold increase in the bremsstrahlung-dose in the laser direction. Experiments have also demonstrated the reproducibly of these results.

References

[1] L.P. Pugachev et al., “Acceleration of electrons under the action of petawatt-class laser pulses onto foam targets”, NIM A 829 (2016), pp. 88-93.

[2] T. Bonnet et al., “Response functions of imaging plates to photons, electrons and 4He particles”, RSI 84 (2013), pp. 103510-1-103510-7.

[3] F. Horst et al., “A TLD-based ten channel system for the spectrometry of bremsstrahlung generated by laser-matter interaction”, NIM A (2015), p. 1.

Photon and Particle Spectroscopy

Precision spectroscopy using a maXs microcalorimeter

M. O. Herdrich[1,2,3], G. Weber[1,2], A. Fleischmann[4], D. Hengstler[4], and Th. Stöhlker[1,2,3]

[1]HI Jena; [2]IOQ, FSU Jena, [3]GSI, Darmstadt, [4]KIP, RKU Heidelberg

Introduction

A new generation of cryogenic microcalorimeters for usage as high precision X-ray spectrometers is currently under development for the SPARC collaboration. The maXs-30 of the maXs (microcalorimeter array for X-ray spectroscopy) detector design developed by the group of Prof. Enss at KIP, Heidelberg features 64 pixels and a theoretical energy resolution of 5 eV FWHM at 6 keV photon energy with an accessible energy range from several 100 eV up to 100 keV [1]. A fast signal rise time (≈100 ns) enables coincidence measurements with time resolutions in the order of 10 ns. Combined with a high linearity [2] and a good long-term stability, the maXs detector system is well suited for high precision measurements at storage rings such as the ESR or CRYRING at GSI/FAIR. First experiments have already been conducted using a prototype detector in the beginning of 2016 and preliminary results were obtained using a new signal processing algorithm based on finite response filters. The new method is more stable and due to much a faster execution time allows for an online analysis of the detector signals.

Preliminary Results

The experiment was conducted at the ESR using U^{89+} ions with a beam energy of 80 MeV/u in collision with a N_2 gas target. A maXs-30 detector was positioned at 90° with respect to the beam axis, with a ≈10 cm air gap to the interaction chamber. Preliminary results (see fig. 1) show that an energy resolution of approx. 80 eV is achieved throughout the whole energy range of the detector using the newly designed finite response filter for data analysis. This is only 10 eV worse compared to the commonly used optimal filter algorithm [3] which is too computational expensive for online analysis of the measured data. Insufficient temperature control of the detector and noise induced by the ESR might explain the divergence from the theoretical optimal resolution. Nevertheless, a comparison with results from experiments with He-like Uranium conducted by X. Ma et. al in 2000 [4] shows that the achieved energy resolution already surpasses the one of standard semiconductor-based X-ray detectors be a factor of 5. Further improvements can be expected with a better temperature correction. The rather small ratio between the intra-shell transition Δn=0 and the Balmer lines compared to theory is explainable by the absorption of the photons in the air gap and two Beryllium windows which act like a high pass filter for X-rays. A detailed simulation of the collision system is planned to determine the spectral lines as well as to separate radiation stemming from capture and excitation processes.

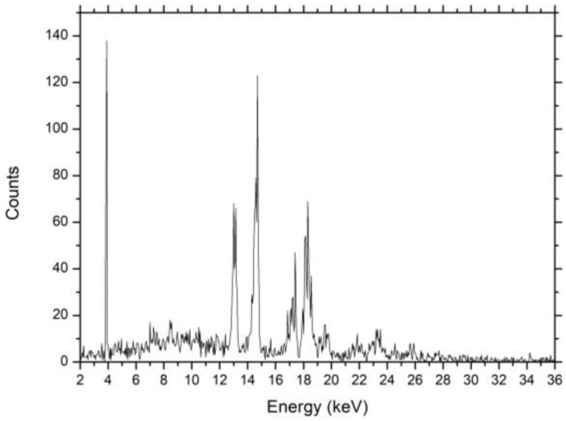

Figure 1: Preliminary results showing an X-ray spectrum recorded at the ESR for U^{89+} collisions with N_2 at 80 MeV/u. Visible are the inner shell transition $\Delta n=0$ in the L-shell ($1s_2\ 2p_{3/2} \rightarrow 1s_2\ 2s_{1/2}$) of the projectile as well as several Balmer ($n > 2 \rightarrow L$) and Paschen ($n > 3 \rightarrow M$) transitions. Radiation resulting from both capture and excitation of the projectile can be seen.

Conclusion and Outlook

The analysis of first experimental data recorded by the maXs-30 detector shows that results generated with the new algorithm are comparable to the results of the optimal filter. Planned improvements include a recently updated version of the maXs-30 detector, which contains a temperature sensitive pixel. Every global temperature change of the detectors shifts its operating point and thereby changes the baseline of the detector signals. By reading out the baseline of the temperature sensitive pixel for every readout cycle, a correlation between energy and working point can be found. A simple bilinear correction is applied to compensate temperature induced shifts of the read-out energy. First tests show, that this method is highly effective in resolving artificial multipeak structures arising from an unstable operation point.

This report is also part of the GSI Annual Report 2017

References

[1] D. Hengstler et al., Phys. Scr. T166, 2015
[2] C. Enss et al., J. Low Temp. Phys., Vol. 121, 2000
[3] A. Fleischmann, Dissertation, RKU Heidelberg, 2003
[4] X. Ma et al., Phys. Rev. A, Vol. 64, 2001

Excitation cross sections of hydrogenlike uranium in collisions with hydrogen and nitrogen targets

G. Weber[1], A. Gumberidze[2], A. Surzhykov[3,4], C. J. Fontes[5], and Th. Stöhlker[1,2,6]

[1]Helmholtz Institute Jena, Germany; [2]GSI, Germany; [3]PTB, Germany; [4]TU Braunschweig, Germany; [5]Los Alamos National Laboratory, USA; [6]FSU Jena, Germany;

Electron impact excitation (EIE) and proton impact excitation (PIE) of bound electrons belong to the most fundamental atomic physics interaction processes. Compared to ionization, excitation is mediated by the same interaction mechanism, but the bound electron is excited into a bound state of the ion and not into the continuum. Therefore, the final state of the electron after the collision can be determined by measurements of the deexcitation photons, which allows for a rigorous testing of corresponding theories. While in particular EIE excitation of few electron ions, such as hydrogenlike argon, titanium and iron, has been thoroughly studied in electron beam ions traps [1], for probing of relativistic effects, i. e. the generalized Breit interaction (GBI) [2,3], high-Z ions that are available at GSI provide the best conditions.

Indeed, a recent study of the Lyman radiation emitted by hydrogenlike uranium in collisions with hydrogen and nitrogen gas targets allowed the first identification of the GBI contribution in EIE of a high-Z system [4,5]. The measurement was performed at the internal gas target of the experimental storage ring of GSI, Darmstadt where an array of standard Ge(i) detectors were recording the x-ray emission from the interaction zone of the ion beam and the gas jet target. After capturing a target electron the down-charged projectiles were recorded by a MWPC detector located downstream after the next dipole magnet. Applying a coincidence condition between x-rays and down-charged ions allows identifying those spectral features that are associated with the capture of target electrons into bound projectile states. This is illustrated in Fig. 1 where the photon spectrum coincident with electron capture is contrasted to the one which is not associated to a change of the projectile charge and that contains Lyman emission subsequent to the excitation of the projectile in collisions with target atoms. The previous study of projectile excitation [4,5] concentrated on the intensity ratio of the Ly-a$_1$ line ($2p_{3/2}$ to $1s_{1/2}$) to the Ly-a$_2$ ($2s_{1/2}$, $2p_{1/2}$ to $1s_{1/2}$) line that reflects a significant enhancement of the EIE cross section due to the GBI which populates preferentially the j=1/2 orbitals.

In a follow-up study we now aim to determine not only relative excitation cross sections (ground state to the L shell) but absolute ones by normalizing the observed Lyman radiation intensity to the intensity of the radiation emitted in the capture of target electrons into the K and L shell of projectile (K- and L-REC). Since in light targets the electrons are only loosely bound, they can be treated as quasi-free, making REC similar to the radiative recombination (RR), which is the time-inverse of the well-understood photoelectric effect.

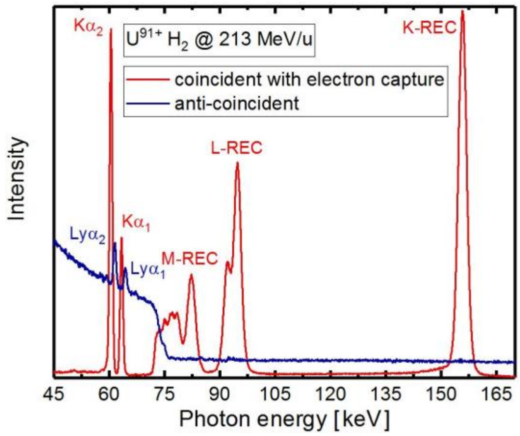

Figure 1: X-ray spectrum recorded by a Ge(i) detector located at 120° with respect to the ion beam axis.

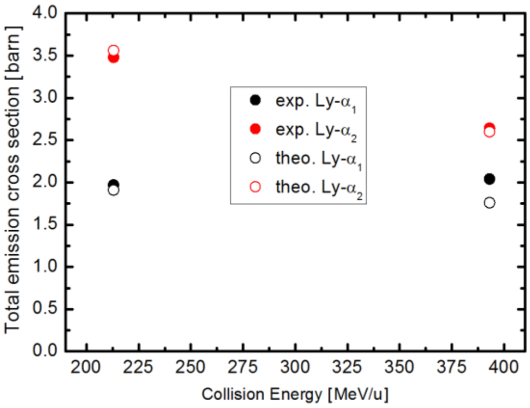

Figure 2: Preliminary results for K-L excitation cross sections for U^{91+} in collision with hydrogen atoms.

Preliminary results of this analysis are shown in Fig. 2 for the collision of hydrogenlike uranium with hydrogen atoms. Theoretical predictions combine both PIE as well as EIE, the latter including the GBI. Note that the population of n=2 states by cascades from higher lying states is not included yet in the theoretical values.

[1] D. L. Robbins et al., Phys. Rev. A 74, 022713 (2006).
[2] C. J. Bostock et al., Phys. Rev. A 80, 052708 (2009).
[3] C. J. Fontes et al., Phys. Rev. A 49, 3704 (1994).
[4] A. Gumberidze et al., Phys. Rev. Lett. 110, 213201 (2013).
[5] A. Gumberidze et al., J. Phys. B 48, 144006 (2015).

Measurements of linear polarization of radiative electron capture*

M. Vockert[1,2], *G. Weber*[2,3], *U. Spillmann*[3], *T. Krings*[4] *and Th. Stöhlker*[1,2,3]
for the SPARC Collaboration

[1]Friedrich Schiller University, Jena, Germany; [2]HI Jena, Germany; [3]GSI, Darmstadt, Germany; [4]FZ Jülich, Germany

In recent years, substantial efforts of the SPARC collaboration went into the development of Compton polarimeters to address the linear polarization properties of hard x-rays emitted by relativistic highly-charged ions interacting with matter. By applying this technique, subtle effects could already be revealed such as the E1/M2 multipole mixing for the Lyman transitions in H-like uranium [1] or the polarization transfer of bremsstrahlung arising from spin-polarized electrons [2]. Moreover recently the polarization transfer in Rayleigh scattering was studied using the aforementioned polarimeter systems [3]. To further improve and to widen the range for future applications, a new 2D position-sensitive demonstrator system has been developed based on a ≈9 mm thick Li-drifted silicon detector (for details see Ref. [4]). A unique feature of this new demonstrator are cooled preamplifiers, enabling a strong noise reduction and consequently a substantial improvement of the energy resolution.

The superior performance of the new polarimeter system was demonstrated in a test experiment at the internal gas target of the ESR storage ring. For the measurement bare xenon ions at an energy of 31 MeV/u have been used, colliding with a molecular hydrogen target [5]. The x-ray emission associated with electron capture into the projectile ions has been observed at 90° with respect to the beam axis in coincidence with a particle detector located behind the next dipole magnet. The resulting, well-resolved x-ray spectrum is displayed in figure 1, showing radiative (REC) as well as characteristic transitions of the projectile.

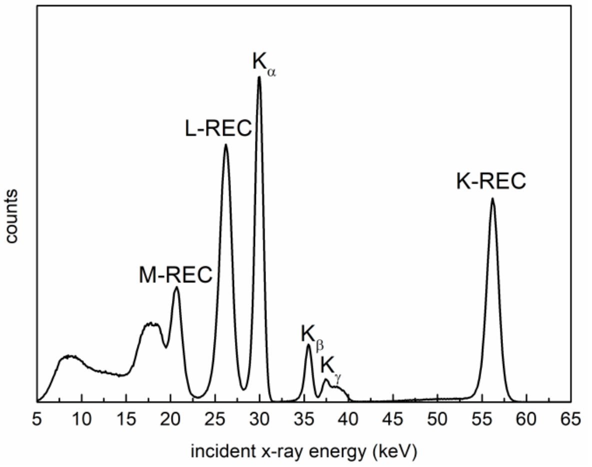

Figure 1: Spectrum obtained at the internal gas target of the ESR storage ring using a beam of bare xenon ions at a kinetic energy of 31 MeV/u and a hydrogen target.

Due to the improved detector performance, Compton polarimetry could be applied to the K-REC radiation with an energy of about 56 keV. Note that when using the previous Compton polarimeters with preamplifiers at room temperature, this technique could only be applied at energies above 80 keV.

The preliminary analysis indicates an almost complete linear polarization (close to 100%, see Fig. 2). This astonishing finding is in agreement with rigorous relativistic calculations which for the specific collision system and observation angle yield similar results as the non-relativistic dipole approximation [6]. This observation indicates that for medium-Z ions and at such low collision energies, relativistic effects are quite small. Note, in comparison with the data previously obtained at higher energies [7,8], the obtained accuracy of the improved setup was increased as well, leading to an uncertainty of only about 1.5%. Therefore, by utilizing the characteristics of the REC radiation, we realize an energy-tunable, monochromatic source of almost fully polarized x-rays for a broad energy range.

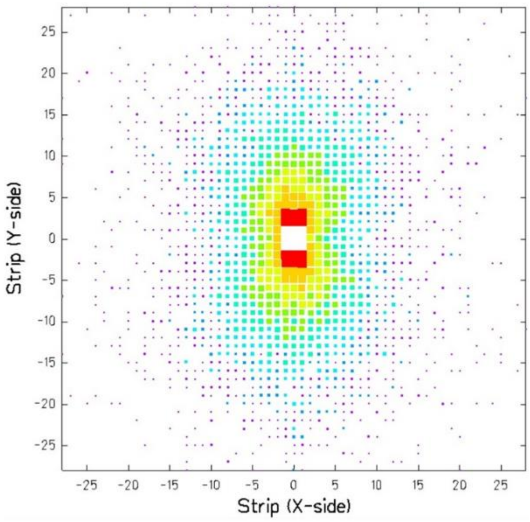

Figure 2: Position distribution of the scattered Compton photons with respect to the point where the scattering took place for the K-REC peak restricted to polar scattering angles of $\vartheta = (90 \pm 15)°$.

[1] G. Weber et al., Phys. Rev. Lett. 105, 2010, 243002
[2] R. Märtin et al., Phys. Rev. Lett 108, 2012, 264801
[3] K.-H. Blumenhagen et al., New J. Phys. 18, 2016, 103034
[4] M. Vockert et al., Nucl. Instr. Meth. B 408, 2017, 313
[5] J. Glorius et al., J. Phys. Conf. Ser. 875, 2017, 092015
[6] J. Eichler and Th. Stöhlker, Phys. Reports 439, 2007, 1-99
[7] S. Tashenov et al., Phys. Rev. Lett. 97, 2006, 223202
[8] S. Hess et al., J. Phys. Conf. Ser. 194, 2009, 012205

---

* Work supported by BMBF Verbundprojekt 05P15SJFAA. This report is also part of the GSI Scientific Report 2017.

Experimental determination of electron capture cross sections into excited states of decelerated xenon projectiles

F. M. Kröger[1,2,*], G. Weber[2,3], J. Glorius[3], Y. Litvinov[3,4], M. O. Herdrich[1,2], U. Spillmann[3], M. Vockert[1,2], Th. Stöhlker[1,2,3]

[1]FSU Jena, Germany; [2]HI Jena, Germany; [3]GSI, Germany; [4]RKU Heidelberg, Germany

Currently only very few data exists for electron-capture cross sections of highly-charged ions colliding with atoms/molecules at energies well below the respective projectile ionization threshold. However, such conditions will be common for beams of decelerated highly-charged heavy ions in the recently commissioned CRYRING@ESR of GSI/FAIR, Darmstadt, where the capture rate with residual gas atoms/molecules will determine the ion beam lifetimes. Thus, the knowledge of electron capture cross sections is of particular importance for the planning of experiments in this storage ring.

Here we report on the evaluation of experimental cross-section data obtained for Xe^{54+} ions colliding with H_2 molecules [1]. The experiment was performed at the internal gas target of the ESR storage ring at GSI, Darmstadt using collision energies between 5.5 MeV/u and 30.93 MeV/u. An array of Ge(i) X-ray detectors was placed at various observation angles around the interaction zone. These detectors allowed to record the X-ray emission arising from the ion-atom collisions, in particular those resulting from radiative capture of target electrons into bound states of the projectile ions and also characteristic K radiation due to subsequent transitions from excited states to the ground state, see fig. 1. Note that for a H-like high-Z system two-photon transition rates are negligibly small compared to single-photon transitions. Therefore, as all electron-capture events into excited states will lead to K transitions, the K-shell emission cross-section is a measure of the total electron capture cross-section into projectile states with $n > 1$. By normalizing the observed intensity of the characteristic K radiation to the K-REC (meaning Radiative Electron Capture into the projectile K-shell) intensity (similar to [2]) we related the characteristic K emission cross-section to the well-known K-REC angular differential cross-section.

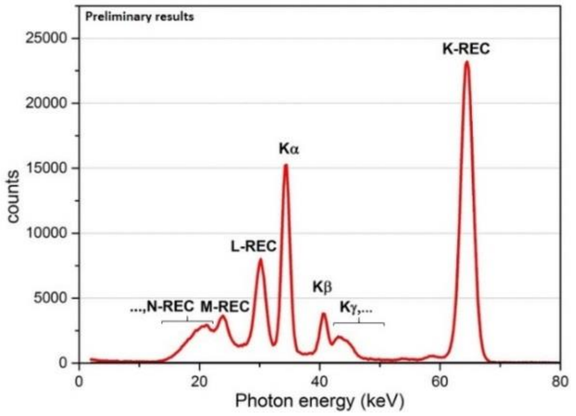

Figure 1: X-ray spectrum of bare xenon ions colliding with H_2 molecules at 30.93 MeV/u, recorded with a photon detector at 60°.

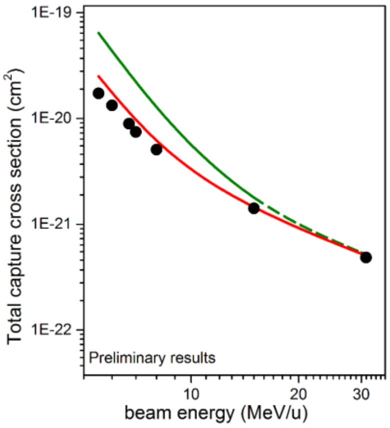

Figure 2: Comparison of total electron-capture cross-sections resulting as the sum of the REC cross sections from [3] and the NRC cross sections calculated with the Schlachter formula (green line) and with the eikonal theory (red line) to the experimental data (full circles) as function of the ion beam energy. In order to present total capture cross sections into all projectile states the experimental cross sections were complemented by theoretical K-REC cross sections.

In figure 2, a comparison of the commonly used empirical Schlachter formula (green line) [4] and of the eikonal theory [5] for non-radiative electron capture (NRC) plus the REC to the preliminary experimental data (full circles) is shown. For the particular collision system under discussion, the range of validity of the Schlachter formula is limited to $E_{kin} < 16$ MeV/u. A dashed line is used for beam energies that lie beyond this range. Note that for the operation of the CRYRING the most important parameters are the total electron capture cross-sections into all projectile states. Therefore, in order to compare the resulting experimental and the theoretical total electron capture cross-sections, theoretical K-REC cross-sections [3,6] were added to the experimental and theoretical capture cross sections into projectile states with $n > 1$. For completion also theoretical K-shell NRC cross-sections should be included, which however are negligibly small compared the K-REC cross-sections.

As can been seen in figure 2, the results of the Schlachter formula deviate markedly from the experimental data in contrast to the eikonal theory, which is in reasonable agreement with the experimental data.

[1] J. Glorius et al., JPCS 875, 092015 (2017).
[2] Th. Stöhlker et al., Phys. Rev. A 58(3), 2043 (1998).
[3] M. O. Herdrich et al., NIM B 408, 294 (2017).
[4] A. S. Schlachter et al. Phys. Rev. A, 27, 3372 (1983).
[5] J. K. M. Eichler, Phys. Rev. A 23, 498 (1981).
[6] G. Weber et al., JPCS 599, 012040 (2015).
[7] J. Eichler and Th. Stöhlker, Phys. Rep. 439, 1 (2007).

---

*felix.kroeger@uni-jena.de

The spectral shape of the atomic two-photon transition in He-like ions

S. Trotsenko[1], A. Volotka[2,3], A. Surzhykov[4,5], A. Kumar[6], D. Banas[7], A. Gumberidze[8], H.F. Beyer[8], H. Bräuning[8], S. Fritzsche[1,2], S. Hagmann[8,9], S. Hess[8], P. Jagodzinski[7], C. Kozhuharov[8], R. Hess[8], S. Salem[8], A. Simon[10], U. Spillmann[8], M. Trassinelli[11], L.C. Tribedi[12], G. Weber[2,8], D. Winters[8], and Th. Stöhlker[1,2,8]

[1]Friedrich-Schiller-Universität, Jena, Germany; [2]Helmholtz Institute Jena, Jena, Germany; [3]Department of Physics, St. Petersburg State University, St. Petersburg 198504, Russia; [4]Physikalisch-Technische Bundesanstalt Braunschweig Germany; [5]Technische Universität Braunschweig Braunschweig Germany; [6]NPD, Bhabha Atomic Research Centre, Mumbai, India; [7]IP, Jan Kochanowski University, Kielce, Poland; [8]Helmholtzzentrum GSI, Darmstadt, Germany; [9]IKF, University of Frankfurt, Frankfurt, Germany; [10]Department of Physics, University of Notre Dame, Notre Dame, IN 46556, USA; [11]Institut des NanoSciences de Paris, CNRS, Sorbonne Universités, UPMC Univ Paris 06, F-75005 Paris, France; [12]Tata Institute of Fundamental Research, Homi Bhabha Road, Coloba, Mumbai 400005, India

Two-photon decay has been an interesting topic since its prediction in 1930's by M. Göppert-Mayer [1]. In this process, two correlated photons are emitted simultaneously under the boundary condition that the sum of their energies equals to the total transition energy, i.e.

$$\hbar\omega_1 + \hbar\omega_2 = E_I - E_F = E_0 \qquad (1)$$

Here, $\hbar\omega_1$ and $\hbar\omega_2$ are the energies of the photons, E_0 is the total transition energy, and E_I and E_F are the energies of initial and final atomic states, respectively. The energies of individual photons form a continuum spectrum which, for the case of decay from $2s$ state, has a maximum intensity at half of the transition energy and gradually falls to zero at both endpoints. This continuum shape is determined by the summation over all intermediate bound- and continuum-states for calculating the transition probabilities which requires knowledge of their energies and wave functions. Hence, the spectral distribution of the two-photon emission is sensitive to the entire atomic structure.

Measurements of the two-photon spectral shape in He-like ions have been significantly improved by the method involving a selective ionisation of a K-shell electron from the initially Li-like ion [2]. Using this method a very clean spectral distribution of the 2E1 decay in He-like tin has been measured. From the measured distribution, a reduced full width at half maximum (FWHM) was obtained. For this, the experimental distribution was fitted with a polynomial distribution. The reduced FWHM was calculated as the width of the distribution divided by the maximum possible photon energy (the energy difference between the $1s2s\ ^1S_0$ and $1s^2\ ^1S_0$ states).

Our preliminary result for the reduced FWHM is compared with theoretical values in figure 1. The comparison shows a clear deviation from the non-relativistic prediction and a very good agreement with our relativistic calculations based on the method developed in [3]. This unambiguously confirms the importance of the relativistic effects for the 2E1 two-photon decay energy distribution. Here, we would like to add that the relativistic values for FWHM obtained by Derevianko and Johnson [4] were found to be in good agreement with the results of our relativistic calculations [2]. The current experimental value for He-like tin can be considered to favor the fully relativistic treatment against the frozen Dirac-Fock result, thus emphasising the importance of accurate treatment of the electron-electron interaction in the mid-Z regime.

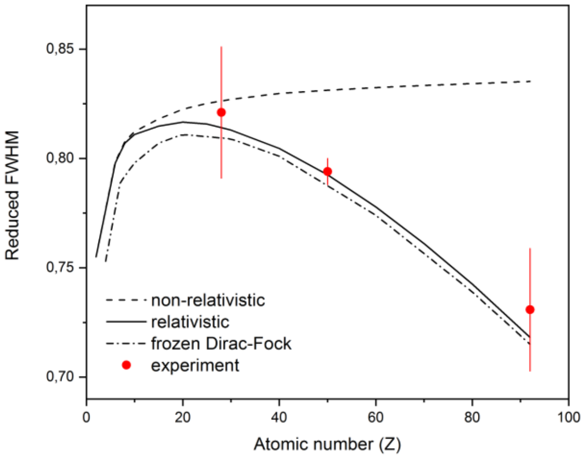

Figure 1: Preliminary results: Comparison of the measured reduced FWHM of the 2E1 two-photon spectral shape for He-like tin with the nonrelativistic calculations, the frozen Dirac-Fock method and the relativistic calculations. In addition, the experimental values for He-like nickel [5] and uranium [6] are shown.

References

[1] M. Göppert-Mayer, Naturwissenschaften 17, 932 (1929)

[2] S. Trotsenko et al., Phys. Rev. Lett. 104, 033001 (2010).

[3] A. V. Volotka, A. Surzhykov, V.M. Shabaev, and G. Plunien, Phys. Rev. A 83, 062508 (2011).

[4] A. Derevianko, W. R. Johnson, Phys. Rev. A 56, 1288 (1997).

[5] H. W. Schäffer et al., Phys. Scr. T80, 469 (1999).

[6] D. Banas et al, Phys. Rev. A 87, 062510 (2013).

*Also part of the GSI scientific report 2017

A scintillator-based high-energy ion detector for CRYRING@ESR*

C. Hahn[1,2,3], P. Pfäfflein[1,2,4], E. Menz[1,2], G. Weber[1,3] and Th. Stöhlker[1,2,3]

[1]HI Jena, Jena, Germany; [2]FSU, Jena, Germany; [3]GSI, Darmstadt, Germany; [4]DESY, Hamburg, Germany

The realization of the novel FAIR accelerator and storage complex achieved a major milestone with the commissioning of the CRYRING synchrotron facility in late 2017. To fully exploit the multifaceted field of research thus made accessible, robust and reliable ion detectors are of fundamental importance [1]. These sensors will need to cope with MHz count rates of ions with energies ranging from sub-MeV/u to 15 MeV/u, and have to withstand the radiation damage imparted by the energetic ions. Given these restrictions, a detector system based on the YAP:Ce crystal scintillator provides an attractive approach, utilizing a material that is both comparatively affordable and endowed with a significant degree of radiation hardness [2].

A UHV-capable sensor design was devised and implemented as a collaborative effort of HI Jena, the University of Jena's Institute for Optics and Quantum Electronics, and the GSI Helmholtz Center. Figure 1 shows a cutaway view of the detector head: to accommodate the low end of the expected ion energy spectrum, the detector is essentially windowless, placing the scintillator material directly inside the vacuum. A light guide coupled to a fused silica window then channels the luminescence generated by the impinging ions to a photomultiplier tube (PMT) for conversion into an electrical signal. To facilitate the vacuum capability, this PMT – and all subsequent electronics – are kept on the atmospheric side of the window, and are installed only after the mandatory baking procedure is completed.

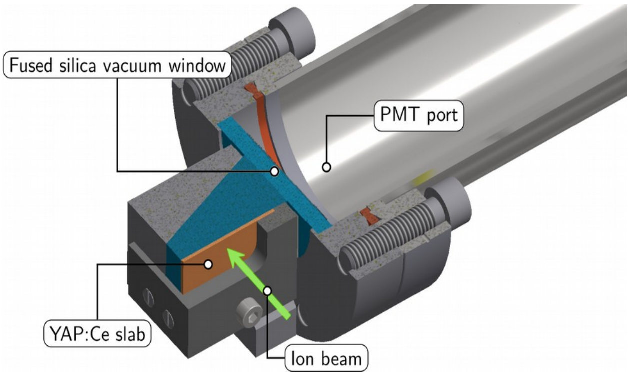

Figure 1: Schematic drawing of the detector head design. The ion beam hitting the scintillator induces light pulses which are registered by a photomultiplier tube attached to the atmospheric side of a UV-transparent vacuum window. Image by P. Pfäfflein and C. Hahn.

To gauge the assembly's sensitivity and long-term durability, a characterization measurement of this system, sans the light guide prism, was conducted at the 3 MV tandem accelerator JULIA operated by the Institute of Solid State Physics at the University of Jena. Using hydrogen, oxygen and iodine ions at energies varying from 0.1 MeV/u to 2.4 MeV/u, the evolution of the PMT output signal was traced through increasing fluences of ion deposition inside the scintillator material, as illustrated by Figure 2. A marked decrease of the pulse height was found with proliferating damage: eventually, the output signal amplitude falls below the level of random noise pulses emitted by the PMT, at which point "true" events, i.e. pulses originating from incident ions, can no longer be reliably discerned by a simple pulse height threshold. This establishes a critical fluence, usually on the order of 10^{13} cm^{-2}, upon which the scintillator material has to be replaced. The exact magnitude of this fluence depends largely on the mass of the impinging ions; their kinetic energy plays only a minor role. On the other hand, the accumulating substrate damage does not appear to lead to an increase of the output pulse length past the initial value of about 50 ns, ensuring a uniform rate capability even after prolonged ion irradiation [3].

Building on the results of this successful proof-of-concept measurement, the final detector setup will be installed at CRYRING in early 2018.

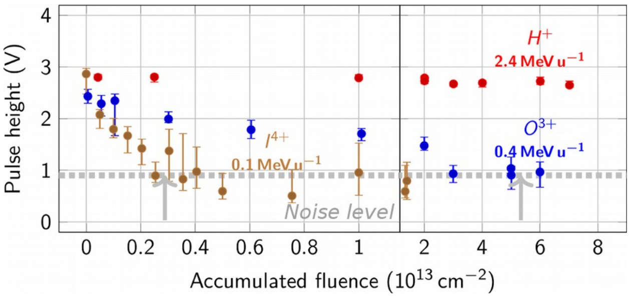

Figure 2: The average observed peak height for different ion species, at increasing accumulated fluences. Once the peak height reaches about 1 V, pulses originating from impinging ions can no longer be easily distinguished from random noise. Image by C. Hahn.

References

[1] M. Lestinsky et al., European Physics Journal Special Topics 225 (2016) 797

[2] M. Tokman et al., Physica Scripta 2001 (2001) 406

[3] P. Pfäfflein, "Entwicklung und Aufbau eines Teilchendetektors für erste Experimente am Ionenspeicherring CRYRING", Masterarbeit, Friedrich-Schiller-Universität Jena (2017)

---

*This report is also part of the GSI Scientific Report 2017.

Charge State Tailoring of Relativistic Heavy Ion Beams for FAIR and CERN

F. M. Kröger[1,2,*], G. Weber[2,3], V. P. Shevelko[4], Th. Stöhlker[1,2,3]
[1]FSU Jena, Jena, Germany; [2]HI Jena, Jena, Germany; [3]GSI, Darmstadt, Germany; [4]Lebedev Physical Institute of the Russian Academy of Sciences, Moscow, Russia

Upcoming heavy ion acceleration facilities will allow to extend the range of achievable beam intensities and energies. For experiments relying on intense, few-electron charge state ions, it is necessary to produce the required charge states with stripper foils optimized for the specific experimental parameters. However, corresponding data on the charge state distribution for the design of effective stripper foils is very rare in the relativistic regime. In addition widely used program codes to estimate the charge state distribution during the passage through matter are limited in the newly accessible high energy range. While for example the commonly used CHARGE code [1] is usable also for relativistic ion-atom collisions, it takes into account only naked, H-like or He-like projectile ions. Therefore the recently developed BREIT[†] code [2], has been verified and adapted to overcome this limitation. In contrast to codes like CHARGE, GLOBAL [1] and ETACHA [3] it has no built-in charge exchange cross sections, so that the algorithm can be used for arbitrary beam energies and charge states as long as the relevant cross sections are provided by the user. For the production of these input cross-sections different well-tested codes have been used. Once these are set the code calculates the charge state distribution as a function of penetration depth for all ions of interest. After first consistency checks at energies of several hundred MeV/u the BREIT code was used together with the aforementioned cross-section codes for an exemplification study for the upcoming FAIR facility at GSI, and finally for a study for the planned Gamma Factory at CERN. In the following these facilities and their respective studies will be presented.

Although a fragment separator (FRS) is not yet planned behind the heavy ion synchrotron SIS100, still there might be a possibility to separate relativistic highly-charged ions at the Super-FRS that could be produced by stripping lowly-charged ions behind the SIS100. However, for this particular example, acting as a proof of principle, the acceleration of U^{82+} ions at the SIS100 up to 2700MeV/u with subsequent stripping to the high charge state U^{89+} was assumed. This charge state was not chosen for a special reason, but it simply is the next highest charge state that the described calculation model newly allows to investigate in this high energy regime. The results calculated for different stripping materials could then be compared to each other to find the ideal target material and thickness for an effective production of the ions of interest, as can be seen in figure 1.

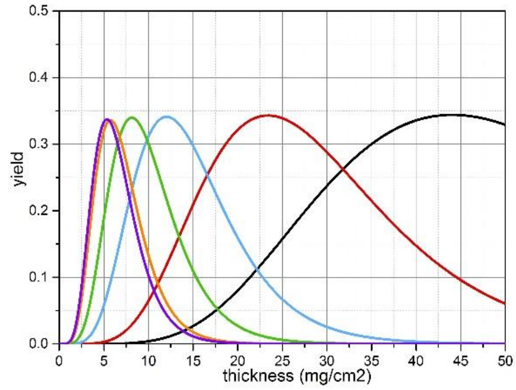

Figure 1: Yield of U^{89+} after collision of U^{82+} with different target materials at 2700 MeV/u against the target thickness in $\mathrm{mg/cm}^2$, calculated with the BREIT code. The lines from left to right are corresponding to the following target materials: ${}^{207}_{82}\mathrm{Pb}$ (violet line), ${}^{197}_{79}\mathrm{Au}$ (orange line), ${}^{108}_{47}\mathrm{Ag}$ (green line), ${}^{64}_{29}\mathrm{Cu}$ (blue line), ${}^{27}_{13}\mathrm{Al}$ (red line), ${}^{12}_{6}\mathrm{C}$ (black line).

Currently, members of the 'Physics Beyond Colliders' study group are exploring possibilities to broaden the present CERN research programme. It is proposed to create a multi-purpose Gamma Factory that pushes the intensity limits of presently operating light-sources by at least seven orders of magnitude in the particular interesting domain of photon energies of $1 \leq \hbar\omega \leq 400$ MeV, opening new research opportunities at CERN [4]. For this task the production of partially stripped relativistic heavy ions Pb^{80+} and Pb^{81+} out of Pb^{54+} will be necessary. The CERN facility allows two different stripping scenarios, one at 72.2 MeV/u and the other at 5900 MeV/u. Both have been studied using the BREIT code, as well as the widely used GLOBAL code in order to find the ideal stripper targets for the mentioned tasks. As a result of this study, ${}^{27}_{13}\mathrm{Al}$ as well as ${}^{48}_{22}\mathrm{Ti}$ stripper foils will be installed in the TT2 transfer line of CERN in order to investigate the stripping yield at an energy of 5900 MeV/u. This first test experiment for the Gamma Factory is scheduled for 2018. The results of the FAIR and CERN studies are tabulated in [5].

[1] C. Scheidenberger, Th. Stöhlker et al., NIM B 142, 441-462 (1998).
[2] N. Winckler et al., NIM B 392, 67-73 (2017).
[3] J. P. Rozet et al., NIM B 107.1-4, 67-70 (1996).
[4] M. W. Krasny, PoS, 532 (2018).
[5] F. Kröger, Master's Thesis (2018).

---

[*] felix.kroeger@uni-jena.de
[†] Balance Rate Equations for Ion Transportation
[‡] Stored Particles Atomic Research Collaboration
[††] Heavy Ion Synchrotron

Acknowledgement goes to M. W. Krasny from LPNHE, University Paris Sorbonne, CNRS–IN2P3, Paris, France and CERN, Geneva, Switzerland

First Tests of X-ray Crystal Optic at the S-EBIT Facilities

S.Wipf,[1,2]*, S.Trotsenko*[1]*, Robert Lötzsch*[1]*, R. Schuch*[3]*, Th. Stöhlker*[1,2]

[1]Friedrich-Schiller-Universität Jena, Germany; [2]HI Jena, Germany; [3]University of Stockholm

Studies at Electron Beam Ion Traps (EBIT) have gained interest in particular in the domain of atomic physics and astrophysics. Here, majority of EBIT-based experiments are aiming on x-ray spectroscopy of the trapped ions. This can be used both for acquiring basic knowledge of transitions in partially ionized atomic system and also as a tool to gain information on the physical processes in the EBIT and to make statements particularly about the composition of the ions. Thereby detectors energy resolution for detection of the emitted x-ray radiation plays an important role. The S-EBIT facility of the Helmholtz Institute Jena, apart from other activities, provides a tool for further steps in the improvement of x-ray spectroscopy in terms of resolving power and collection efficiency. Our previous x-ray diagnostics at the S-EBIT was so far based on a silicon (or germanium) pin-diode detectors with a resolution of a few 100 eV in the energy region of interest [1].

Magnetic metallic microcalorimeters possess new very promising x-ray detection technology that combines the excellent spectral resolution being typical for crystal spectrometers with the high stopping power of solid-state detectors. With this detector technology, the resolution for detected photon energies in keV range is expected to be a few eV [2]. But such microcalorimeters provide only a small active area and, consequently, can cover only a small solid angle in particular if the high magnetic field of the EBIT limits the geometry. Here, the application of a focussing x-ray crystal optics become handy and the effective surface of the detector can be increased by at least an order of magnitude (Fig. 1). The incident and the outgoing x-ray should fulfil the Bragg condition for the x-ray energies that are subject to an enhanced detection efficiency. For the details of this technology we refer to [3].

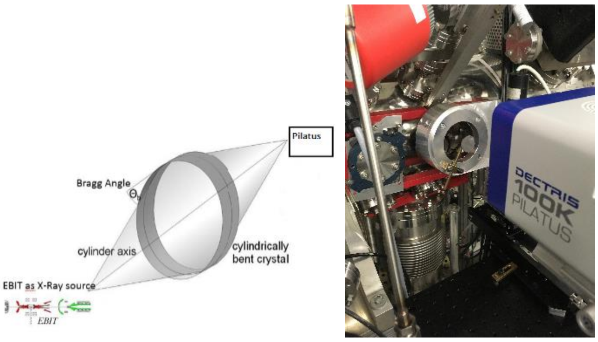

Figure 1: A sketch of the set up and crystal optics mounted in front of the EBIT together with a position sensitive Pilatus detector.

Here we present a first proof of principle measurement of the aforementioned method. The K_α-line of the ionized iron was observed at around 6.75 keV. The crystal optic we used is made of Highly Annealed Pyrolitic Graphite (HAPG) and modified for reflection in the energy range from 7 keV to 12.5 keV. The Bragg angle of the optics with respect to the window was theoretically calculated to be around 16.0° for the energy range of interest and the distance between optics and detector was 163 mm. We used the spatial resolving silicon pixel detector PILATUS behind a toroidal shaped x-ray optic and obtained an image of the ion cloud inside the trap. A motorized steering with dedicated LabView software has been used to align the x-ray optic to match the focussing conditions, given by the energy-dependent Bragg angle and the distance between source, optics and the detector. The threshold of the Pilatus detector was set to 1.5 keV and frames with 100 s exposure time were taken. Figure 2 shows an image of the ion trap in the X-Ray wavelength- range with the presented set up (top) and attendant spectrum measured with the Si-pin diode on the opposite EBIT view port (bottom). The EBIT-I operated with 25mA (10keV) electron beam.

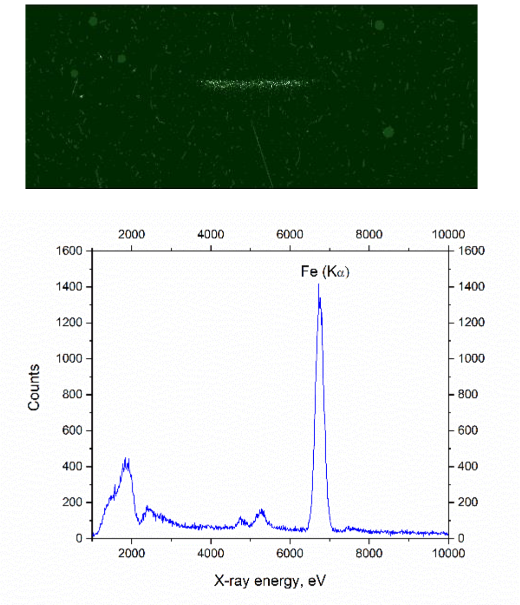

Figure 2: Image of the EBIT x-rays formed by the x-ray optics (top) and a spectrum measured in parallel with the Si-pin diode (bottom).

In summary, we successfully performed the first proof of principle of the x-ray optics measurements at the S-EBIT facility. The further steps are currently in progress and will involve measurements with the position and energy resolving CCD detector. Ultimately, the combination of the magnetic metallic microcalorimeter detectors with the crystal optics at the S-EBIT should reveal the full power of the invented method for the x-ray spectroscopy of highly charged ions.

References

[1] S. Trotsenko, HI Jena Scientific Report 2016, p.76
[2] C. Pies et al., 2012, J Low Temp Phys (2012) 167:269–279
[3] R. Lötzsch, HI Jena Scientific Report 2015, p. 49

Highly Charged Ions at the HILITE Penning trap experiment*

S. Ringleb[1], N. Stallkamp[1,2,3],M. Kiffer[1], S. Kumar[4], T. Morgenroth[1,3], G. Paulus[1,2], W. Quint[3,5], Th. Stöhlker[1,2,3]and M. Vogel[3]

[1]Friedrich Schiller Universität Jena; [2]Helmholtz-Institut Jena; [3]GSI, Darmstadt, Germany; [4]Inter-University Accelerator Centre, New Delhi, [5]Ruprecht Karls-Universität Heidelberg

Detailed investigations of laser-matter interactions require well-defined ion targets and detection techniques for high-sensitivity measurements of reaction educts and products. Therefore, we have conceived, designed and built the HILITE Penning trap experiment. It employs ion-cloud formation techniques as well as destructive and non-destructive techniques to analyse the trap content for all species and charge states individually and simultaneously [1]. This facilitates reconstruction of non-linear interactions of stored particle targets with high-energy and/or high-intensity lasers.

In order to be independent from external ion sources and to be able to perform experiments at different laser facilities, a dedicated ion source is needed, which fulfils the key requirement of the complete setup, namely to be easily transportable. For that purpose, a compact electron beam ion source (EBIS) together with a dedicated control and readout system has been implemented and brought into operation [2].

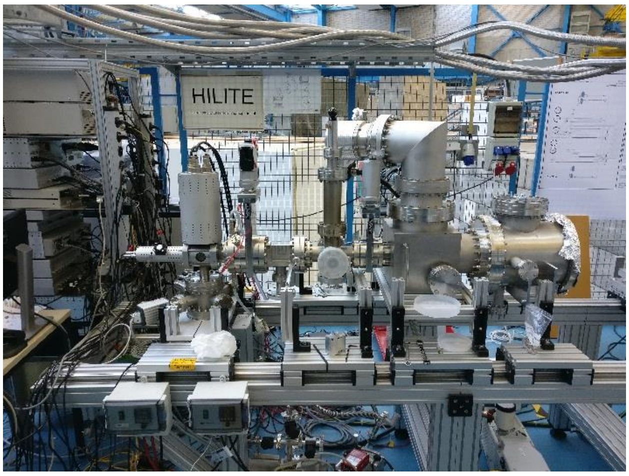

Figure 1: Ion source setup (EBIS, left) with attached diagnostic chamber (right).

We have measured the voltage switching times for ion deceleration and ion capture to verify the performance when slowing down ions extracted from the EBIS for subsequent storage in the HILITE trap. After capture, the ions will initially have kinetic energies of the order of 200 eV. For fast and efficient ion slowing, we have developed a novel implementation of 'active ion slowing', where the ion-signal induced in one trap electrode segment is used for negative feedback. Consequently, the ions experience a repulsive force when approaching the electrode and an attractive when leaving it. Obviously, feeding the slowing signal back to the pick-up electrode causes a strong overlap between ion signal and the slowing signal itself. To overcome this issue, we have implemented a balanced Wheatstone bridge consisting of four capacitors, one of which is the trap electrode itself. The voltages applied to both branches are subtracted from each other. In consequence, the difference is the pure ion signal, as this is only induced in one of the branches. The circuit diagram and the manufactured electronics board used in our trap is shown in figure 2. First tests show, that both branches can be balanced out well.

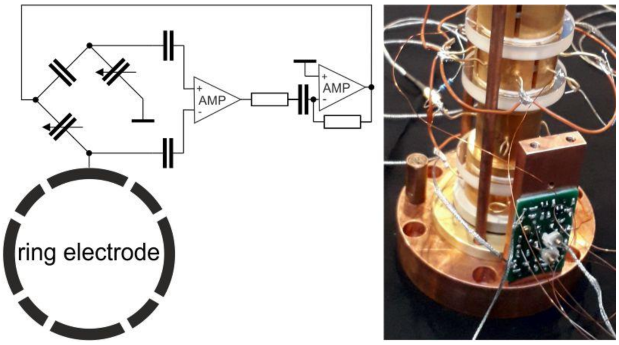

Figure 2: Feedback ion-cooling circuit and photo of the electronics board attached to the trap.

Following this active feedback slowing, we will apply cooling techniques to further cool the ion ensemble down to the environmental temperature of about 4K. This will be done by the well-known 'resistive cooling' technique, where the ions lose energy by dissipating power to a cryogenic resonance resistance. Such cooling facilitates the application of various ion manipulation techniques for control over ion density, position and the overall composition of the target ion ensemble confined in the trap.

*Also part of the annual report 2017, GSI.

References

[1] S. Ringleb, M. Vogel, S. Kumar, W. Quint, G. Paulus, Th. Stöhlker, Journal of Physics Conference Series 635 (2015) 092124

[2] T. Morgenroth, Master thesis, Uni Jena 2017

A status report on 2D Compton polarimeter development

U. Spillmann^{1}, T. Krings^{2}, M. Vockert^{3,4}, G. Weber^{3}, and Th. Stöhlker^{1,3,4} on behalf of the SPARC collaboration

^{1}GSI, Darmstadt, Germany; ^{2}IKP, FZ-Jülich, Germany; ^{3}HI Jena, Germany; ^{4}IOQ, Friedrich Schiller Universität Jena, Germany

For the experimental program of the SPARC collaboration [1] at GSI and FAIR, x-ray spectroscopy and x-ray polarimetry are essential tools.

Polarization of x-rays coming from recombination processes induced by collisions of heavy and highly charged ions at relativistic energies with electrons or low-density gaseous targets provides a unique insight into the dynamics of charged particles in extremely strong and temporally short electromagnetic fields. Detailed knowledge of these processes has, besides atomic physics itself, a great relevance for plasma- and astrophysics.

During the last years we continuously strengthened the instrumentation portfolio of SPARC with dedicated Si(Li)-and Ge(i)-Compton polarimeters which we employed very successfully in experiments at GSI and other research labs, like DESY and ESRF. This technology is based on LN_2-cooled planar double-sided structured detectors (Li-drifted silicon or high purity germanium bulk) with thicknesses in the range of 10 mm. The optimization of such systems for different energy regimes is an ongoing effort.

In this context we designed two test systems where the discrete preamplifier stage was replaced by ASICs to study the pros and cons with focus on a multi-channel readout solution. A 16-pixel HPGe(i) detector was equipped with Cube-ASICs which were run in the transistor-reset as well as in the resistor-reset mode [2]. With this chip we measured the best spectroscopic resolution for our systems up to now. Unfortunately the very high price per channel will only allow for the implementation in very special cases.

In the second study we built a system based on the PIXIE-ASIC[3], developed by Rutherford Appleton Laboratory (RAL), bonded to a linear Si(Li) pixel detector and later to a linear Ge(i) pixel detector. The PIXIE ASIC was developed by RAL to study the properties of CdTl and CdZnTe detectors with small pixel structures at room temperature.

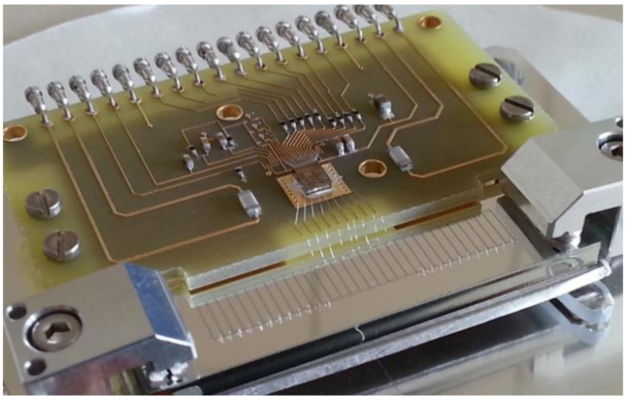

Figure 1: The test pcb with the PIXIE ASIC bonded to a test detector.

Finally we were able to show that this chip, although cooled down to 200 K and operated with higher detector capacitance than allowed by the specs, was able to produce nice results. With pixel structures of 1x5mm^{2} we achieved 1.5 keV resolution at 60 keV x-ray energy. This is comparable with discrete preamps run at room temperature. The ASIC pcb is at least by a factor 5 more compact compared to discrete preamps. This test has proven the usability of this technology for a multi-channel readout ASIC for Si(Li)- and Ge(i)-detectors. With minor modifications, to adapt the ASIC especially for these semiconductors, the spectroscopic performance could even be more optimized.

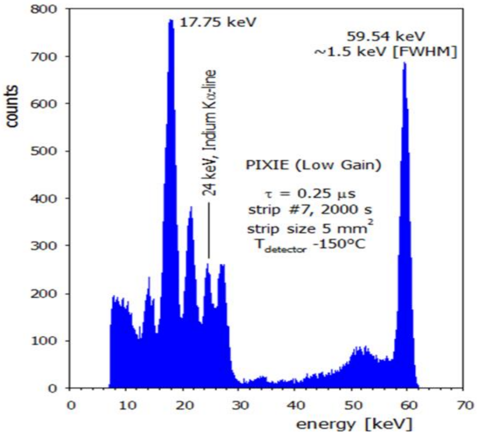

Figure 2: Spectroscopic results of the PIXIE ASICs with Si(Li) pixel detector irradiated with a Am-241 x-ray source.

We like to thank P. Seller, M. French, M.C. Veale, J. Lipp, L.L. Jones, A. Hardie from STFC, RAL(United Kingdom).

This report is also part of the GSI Scientific Report 2017.

References

[1] Technical Report of the SPARC collaboration https://www.gsi.de/work/forschung/appamml/atomphysik/ap_und_fair/sparc/dokumente.htm

[2] T. Krings et al., 2015 JINST 10 C02043

[3] M.C. Veale et al., IEEE Trans. Nucl. Sci., vol. 58, no. 5, October 2011, pp. 2357-2362

High-purity polarization spectroscopy of electronic anisotropies in cuprates

A.T. Schmitt[1,2], I.Uschmann[1,2], K.S. Schulze[1,2], R. Lötzsch[1,2], H. Bernhardt[1,2], B. Grabiger[1,2], B. Marx-Glowna[2], Y. Joly[3], M. von Zimmermann[4], H. Yavas[4], H.-C. Wille[4], E. Förster[1,2], G.G. Paulus[1,2], R. Röhlsberger[4]

[1]Institut für Optik und Quantenelektronik, Friedrich-Schiller-Universität, Max-Wien-Platz 1, 07743 Jena, Germany

[2]Helmholtz-Institut Jena, Helmholtzweg 4, 07743 Jena, Germany

[3]Institut Néel, 25 Avenue des Martyrs, 38042 Grenoble, France

[4]Deusches Elektron-Synchrotron DESY, Notkestr. 85, 22607 Hamburg, Germany

Since the discovery of high-temperature superconductivity in 1986 there has been much effort to explain the physics in strongly correlated systems like cuprates as conventional theories fail to explain their origin [1]. To understand the superconductivity in the cuprates it is a powerful method to explore the electronic structure and symmetry of the copper oxides by XANES measurements at the Cu absorption edge. Especially the pre-edge region of the K-edge offers unique insights into materials containing transition metals.

Combining spectroscopy and polarimetry in the x-ray regime

Unique x-ray polarizers designed in Jena can reach polarisation purities up to 10E-10 and have already been used successfully for applications in nuclear resonance, Mößbauer spectroscopy and quantum optics in the last years [2,3]. Those x-ray polarizers are based on Bragg reflection at scattering angles very close to 90°. Using crossed x-ray polarizers, tiny optical anisotropies caused by electronic anisotropies can be detected.

The combination of this extreme sensitive technique with x-ray spectroscopy provides information about the polarization dependent absorption and therefore enables detection of electronic anisotropies and structural symmetries. Such information helps to understand the behaviour of cuprates at low temperatures and may path the way for the complete understanding of high-temperature superconductivity.

For the investigation of cuprates, quartz polarizers with a 320-reflection were designed to achieve a high energy resolution of 50 meV combined with a high polarisation purity of 1.2E-7 at the Cu K-edge.

To test this new technique of x-ray spectroscopy combined with x-ray polarimetry, CuGeO3 was used as a model substance for the complicated cuprate superconductors. In order to investigate electronic anisotropies in CuGeO3, absorption spectra of the Cu K-edge were measured for different angles between the crystal axes and the electric field vector. The measurements exhibited a strong polarization dependent absorption of the 1s to 3d transition at the Cu pre-edge at 8979 eV, which indicates a certain orientation of the 3d orbitals. DFT-simulations can provide information about dipole and the quadrupole contribution to the pre-edge features, in order to gain information about structural symmetries or symmetry breaking.

This sensitive method of spectropolarimetry with quartz crystals can now be used to investigate cuprate superconductors and other substances to explore electronic anisotropies.

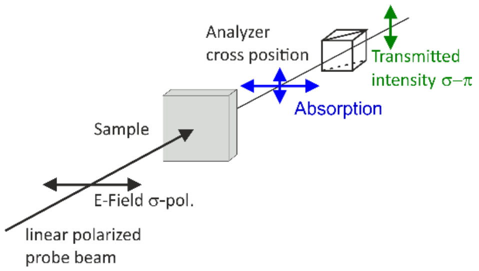

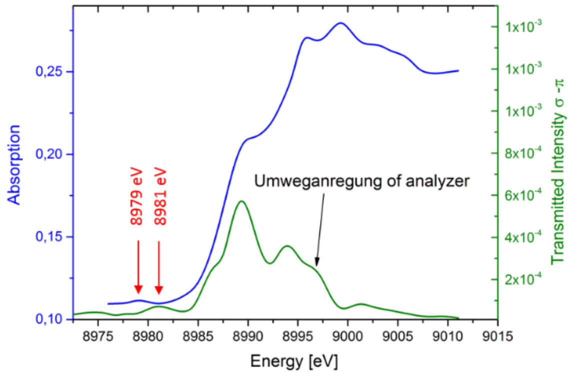

Figure 1: Polarized XANES measurement of Cu K-edge of CuGeO3 (blue) in comparison to the transmitted intensity of sigma to pi with crossed polarizer and analyser setup (green).

References

[1] B. Keimer et al. , Nature 518, 179 (2015)

[2] B. Marx, K.S. Schulze, I. Uschmann, T. Kämpfer, R. Lötzsch, O. Wehrhan, W. Wagner, C. Detlefs, T. Roth, J. Härtwig, E. Förster, T. Stöhlker, G.G. Paulus Physical Review Letters 110 (2013), 254801 1-4

[3] J. Haber, K.S. Schulze, K. Schlage, R. Loetzsch, L. Bocklage, T. Gurieva, H. Bernhardt, H.C. Wille, I. Uschmann, G. G. Paulus, R. Röhlsberger, Nature Photonics 10, 445-449 (2016) and references therein.

Refractive index modulation induced by high intensity THz radiation

M. Almassarani[1,2]*, A. Woldegeorgis**[1,2]*, T. Kurihara*[4]*, J. Bosserrt*[3]*, R. Größe*[2]*, B. Beleites*[2]*, F. Ronneberger*[2]*, G. G. Paulus*[1,2]*, and A. Gopal*[1,2]

[1]Helmholtz-Institut Jena, Jena, Germany; [2]Institut für Optik und Quantenelektronik, Jena, Germany; [3]Otto Schott Institute of Materials Research, Jena, Germany; [4]Department of Physics, University of Konstanz, Konstanz, Germany

Nonlinear refractive index modulation induced by intense terahertz (THz) pulses in silicon and lactose samples is measured in the spectral regime extending from 0.1 to 3 THz. THz pulses with field strength of 440 MV/m have been employed. Transmittance and the transmitted spectra were measured using Z-scan and single shot noncollinear electro-optic pump-probe techniques. A maximum change in refractive index (Δn) of -0.128 and $+0.245$ were measured in lactose and silicon respectively.

In this experiment, performed at the JeTi 40 TW laser system, high-power broadband THz pulses were generated from rear side of a thin metal foil when its front surface is shined with TW laser pulses[1]. The THz beam is collected and focused by an f/1.18 ellipsoidal mirror to a $1/e^2$ spot size w_0 of 2 mm producing a peak THz intensity of 26 GW/cm^2. The experimental scheme is described in figure 1. The transmission and closed-aperture Z-scan measurements[2] were performed on 1.5 mm thick α-lactose and 700 μm thick silicon samples which were placed at the focus of the THz beam inside the vacuum chamber. The peak electric field, and the temporal and spectral characteristics of the transmitted THz pulses with and without the sample inserted were measured outside the chamber using a noncollinear pump-probe electro-optic (EO) technique. 100 μm thick gallium phosphide (GaP) crystal cut along the $<\ 110\ >$ plane was used as EO crystal. The 2-D image of the optical laser beam that probes the induced birefringence in the GaP crystal was recorded using a CCD camera. The horizontal axis of the image gives the temporal information of the THz pulse from which the spectrum of the THz pulse is retrieved where as the vertical axis provides the spatial dimension of the THz beam. Focusing and defocusing of the THz beam due to nonlinear refraction were seen as shrinkage and elongation of EO signal in the spatial axis of the CCD image.

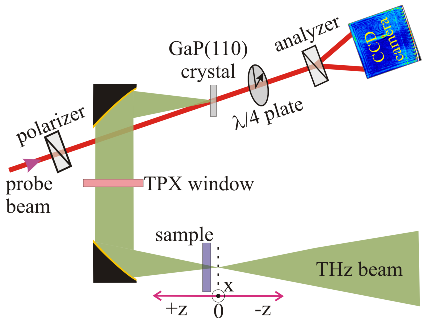

Figure 1: Schematic of the experimental setup.

Results from Z-scan measurements show opposite sign of nonlinearity for silicon and lactose indicating self focusing (positive) and self-defocussing (negative) effects when the samples are translated from pre-focal plane through the focus. Figure 2 shows that THz induced refractive index modulation is frequency-dependent. The spectrally-averaged refractive index change Δn of -0.032 ± 0.003 and $+0.092 \pm 0.007$ were measured in lactose and silicon respectively. The Kerr coefficient n_2, determined using the Z-scan technique for a center frequency 0.2 THz, of lactose was calculated to be -1.49×10^{-12} cm^2/W whereas the n_2 value for silicon is 3.51×10^{-12} cm^2 /W.

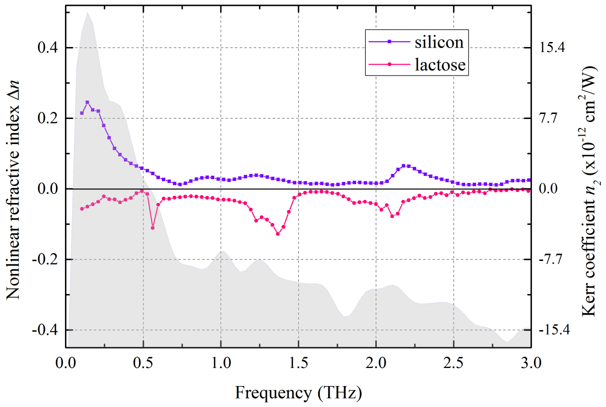

Figure 2: Nonlinear refractive index modulation Δn and Kerr coefficient of lactose and silicon sample as a function of frequency in the spectral range $0.1 - 3$ THz calculated at $z = 0$. The light gray background shows the spectral amplitude of the reference THz pulse.

Upcoming experimental campaigns will focus on thorough investigation of nonlinear processes such as nonlinear refraction and absorption saturation in the THz spectral range in various semiconductors.

References

[1] Gopal, A. et al. Phys. Rev. Lett. 111, 074802 (2013); Gopal, A. et al. New J. Phys., 14, 083012 (2012); Herzer, S. et al. New J. Phys., accepted (2018).

[2] Sheik-Bahae, M. et al. Opt. Lett. 14, 955-957 (1989).

---

[*] abel.woldegeorgis@uni-jena.de

Fragmentation of the HeH$^+$ molecular ion in strong laser fields

P. Wustelt[1,2], F. Oppermann[3], L. Yue[4], A.M. Sayler[1,2], M.Möller[1,2], T.Stöhlker[1,2], S.Gräfe[4], M. Lein[3] and G.G. Paulus[1,2]

[1]Helmholtz Institut Jena, Germany; [2]Institute for Optics and Quantum Electronics, Friedrich-Schiller-University Jena, Germany; [3] Institut für Theoretische Physik, Leibniz Universität Hannover, [4]Institute for Physical Chemistry, Friedrich-Schiller-University Jena, Germany

In this project, we experimentally study the laser-induced fragmentation of the HeH$^+$ molecular ion, the benchmark system for the investigation of multiple-electron molecules, mass-asymmetric molecules, charge-asymmetric molecules, and molecules with a permanent dipole. Our measurements of short-pulse laser-induced single and double ionization at various wavelengths and intensities highlights the role of the permanent dipole moment of HeH$^+$.

Since its first experimental observation in 1925 the HeH$^+$ molecular ion, the simplest polar heteronuclear molecule, has served as a fundamental benchmark system for understanding principles of molecular formation and electron correlation [1]. HeH$^+$ continues to intrigue researchers as the first molecular species to arise in the universe, yet it has mysteriously remained absent in astronomical spectra

HeH$^+$ is a two-electron system with an electronic asymmetry and a permanent dipole moment. Despite its great importance, experimental studies of HeH$^+$ in intensive laser fields are rather rare. The reason is, that neutral HeH is not stable. The ion must be synthesized, e.g. in a plasma, and prepared in an ion beam apparatus. For these measurements presented here, a HeH$^+$ ion beam is created in a duoplasmatron ion source using a mixture of helium and hydrogen gas. High intensity laser pulses are then focused into the interaction region of the ion beam coincidence 3D momentum imaging setup, which is regularly operated at the HI Jena.

Three-dimensional momentum distributions of the nuclear fragments of all fragmentation pathways of HeH$^+$, including single and double ionization as well as an estimation of non-ionizing dissociation, were measured for different laser intensities. Using solutions of the time-dependent Schrödinger equation (TDSE) and simulations based on dressed surface hopping (DSH), we are able to reconstruct fragmentation pathways and determine the times and internuclear distances at which each ionization step occurs (see Fig. 1).

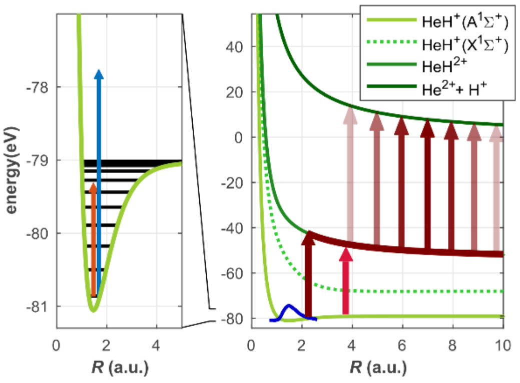

Figure 1: The potential energy curves of HeH$^+$, HeH^{2+}, and HeH^{3+} with the most likely fragmentation pathway for single(dark red) and double ionization (red arrow). The left panel zooms into the ground state and displays its vibrational levels. An 800-nm laser pulse (red arrow) will couple these in contrast to a 400-nm pulse (blue).

The intensity- and KER-dependent single ionization yield of HeH$^+$ at 800 nm pulses is shown in Fig. 2. Here, the most distinct feature is a transition region around $2 \cdot 10^{15}$ W/cm^2, highlighted by an arrow. Responsible for the low-KER fragments is a resonant excitation of vibrational states at the same electronic state, which allows the molecule to stretch and facilitates ionization at lower intensities. The extreme asymmetric nature of HeH$^+$, which is manifested in a strong permanent dipole, results in fundamentally different fragmentation dynamics than those seen in homonuclear molecules. Namely, direct vibrational excitation, with almost no electronic excitation, dictates the fragmentation process here, which is the antithesis of symmetric molecules.

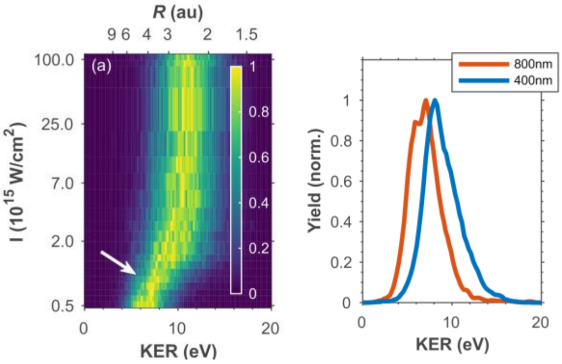

Figure 2: Single ionization of HeH$^+$: (left) Measured fragmentation yield as a function of intensity and KER (lower axis) or internuclear distance R (upper axis) for 800-nm pulses. The yield is normalized for each intensity. At I < 10 15 W/cm^2 substantial ionization is only possible after the bond has stretched, while HeH$^+$ can be ionized without appreciable stretching for high intensities. At 800 nm, the higher vibrational states can be resonantly excited. The stretching dynamics is reduced at 400 nm, which results in slightly larger KER at low intensities (right).

References

[1] T. R. Hogness, E. G. Lunn, *Phys. Rev*. **26**, 44 (1925).
[2] Pedersen et al., *Phys. Rev. Lett*. **98**, 00319007 (2007).
[3] D. Ursrey, F. Anis, B. D. Esry, *Phys. Rev. A* **85**, 023429 (2012).
[4] T. Rathje, et al., *Phys. Rev. Lett.* **111**, 093002 (2013)

Semiconductor nanostructures in strong mid-IR laser fields

R. Hollinger[1,2], *V. Schumakova*[3], *P. Malevich*[3], *R. Röder*[4], *A. Schleusener*[5], *M. Zapf*[4], *U. Reislöhner*[4], *M. Wächtler*[5], *A. Pugzlys*[3], *A. Baltuska*[3], *C. Ronning*[4] *D.Kartashov*[1], *Ch.Spielmann*[1,2]

[1]Institute of Optics and Quantum Electronics, Abbe Center of Photonics, Friedrich-Schiller-University Jena, Max-Wien-Platz 1, 07743 Jena, Germany
[2]Helmholtz-Institute Jena, Helmholtzweg 4, 07743 Jena, Germany
[3]Institute for Photonics, Technical University Vienna, Gußhausstraße 25-29, 1040 Vienna, Austria
[4]Institute for Solid State Physics, Friedrich-Schiller-University Jena, Max-Wien-Platz 1, 07743 Jena, Germany
[5]Leibniz Institute of Photonic Technology, Albert-Einstein-Straße 9, 07745 Jena, Germany

Strong field laser physics describes the interaction of laser pulses with matter in which the electric field is comparable to the electronic binding fields. For condensed matter such as the semiconducting material ZnO this regime is reached for a field strength above ~0.1 V/Å or an intensity of ~1 TW/cm^2 . In this regime the electric field cannot be considered as a weak perturbation to the equilibrium system leading to higher order harmonic generation (HHG) [1] and other effects.

Since the 80's of the last century, HHG has been extensively studied in the gas phase. Transformation of the physical phenomena to the condensed phase was not possible because of the low damage threshold of solids. This problem can be solved using wide band bap materials and ultrashort, long wavelength driving laser pulses [2].

In our experiments we are using intense femtosecond mid-IR (3.9 µm) laser pulses from a high power optical parametric amplifier to experimentally investigate HHG in nanostructured semiconductors.

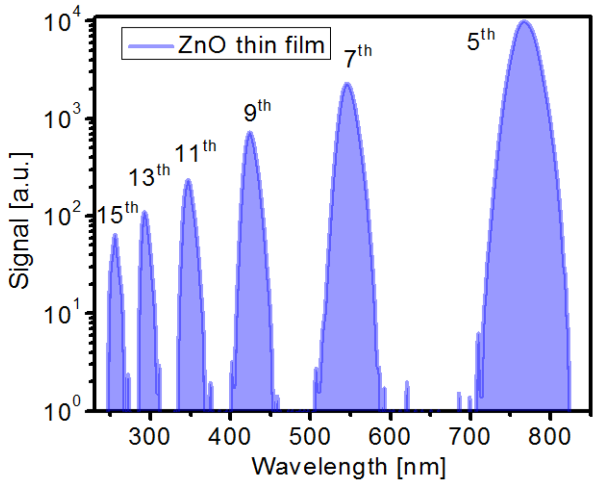

Figure 1: Higher order harmonic generation from rf-magnetron sputtered 300 nm thick ZnO thin films on a sapphire substrate.

Figure 1 depicts a typical higher order harmonics spectrum emitted from a 300 nm thick ZnO thin film. Note, we are able to observe radiation up to the 15th harmonic order. Due to the lack of phase matching for HHG in solids, thin film samples are advantageous compared to bulk samples and show a more efficient light conversion process. Additionally, in this kind of samples a promising tailoring of the light matter interaction by ion implantation is possible.

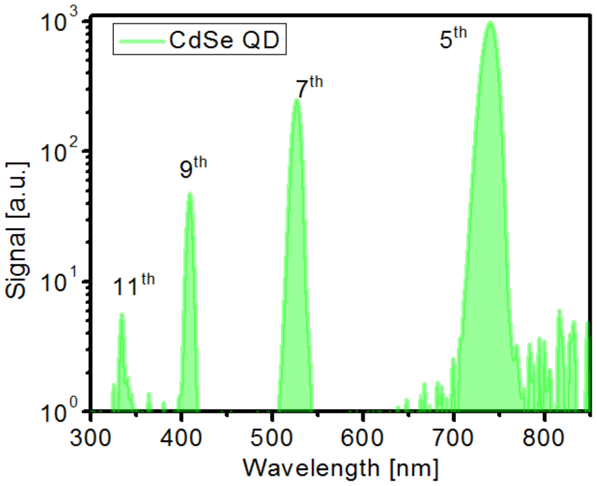

Figure 2: Higher order harmonic generation from colloidal ~2.5 nm CdSe quantum dots drop casted on a sapphire substrate.

Figure 2 shows results using CdSe quantum dots (QD) with a diameter of ~2.5nm to generate higher order harmonics from the mid-IR driver. Due to the strong electronic confinement resulting in a discrete electronic structure and additional crystalline structure, QD's are considered an intermediate model system between atoms/molecules and crystalline solids. Thus the validity of the well-established physical pictures about HHG in gases can be investigated using solids.

After this first successful demonstration of HHG, future work will focus on the investigation of HHG dynamics in nanostructured semiconductors.

References

[1] S. Ghimire, G. Ndabashimiye, A. D. DiChiara, E. Sistrunk, M. I. Stockman, P. Agostini, L. F. DiMauro and D. A. Reis, Journal of Physics B, 47, 204030 (2014)

[2] S. Ghimire, A. D. DiChiara, E. Sistrunk, P. Agostini, L. F. DiMauro and D. A. Reis, Nature, 7, 138-141 (2011)

Characterizing spatial properties of XUV-beams by an improved Young- double slit setup

T. Helk[1,2], *F. Tuitje*[1,2] *and C. Spielmann*[1,2]

[1]HIJ, Jena, Germany; [2]Institut für Optik und Quantenelektronik, FSU Jena, Jena, Germany

Introduction

Increasing the resolution of imaging methods is limited, due to the criteria developed by Abbè and Rayleigh. With modern microscopy techniques like STORM [1] it is possible to achieve a better resolution at the expense of a more complex and versatile setup. A more straightforward way to achieve higher resolution is to decrease the wavelength of the incident radiation. With short wavelength radiation, in the extreme ultraviolet (XUV) or X-ray range, the resolution can be as high as several nm, but is usual lower due the lack of high numerical aperture optics. Lensless imaging methods, for example coherent diffractive imaging (CDI) or ptychography, require a light source with defined spatial properties. A modified Young-double slit setup is capable to measure the required characteristics. This method is called “SCanning Interference Measurements for Integrated Transversal Analysis of Radiation ” (SCIMITAR). Based on the work of Lloyd et. al [2, 3], we developed a modified set-up to measure the spatial and axial characteristics of different XUV-sources.

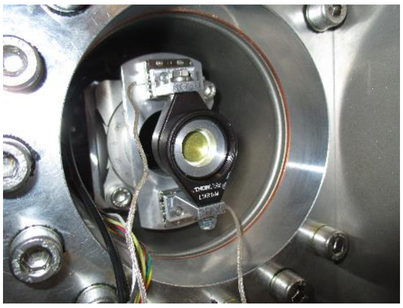

Figure 1: View of the assembled SCIMITAR-setup.

Experimental implementation

The SCIMITAR-setup is a combination of two different slit apertures, one single slit and one X-shaped slit [2]. The two slits are mounted on linear stages, which are constructed on a rotating mount. The whole part is mounted on a linear stage, for movement in direction of the optical axis (see Fig.1). The two apertures are arranged in a way that their longitudinal separation is less than the Rayleigh length and their transverse orientation allows to form a single pinhole at zero position. Moving the X-slit perpendicular to the single slit leads at first to a deformation of the single pinhole and after a minimum distance x_{min}, which depends on the dimensions of the slits, two separated pinholes, at which one is stationary and one moves away. Guiding the monochromatized XUV-radiation onto the slits leads to interference fringes (see Fig.2), depending on the separation spacing d, which could be detected in the farfield. Larger spacing leads to narrower fringe patterns.

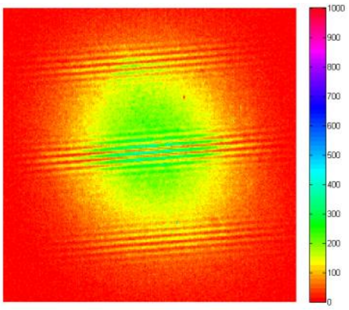

Figure 2: Farfield diffraction pattern.

Using this setup, different XUV-sources were characterized, nameley two different high harmonic sources, a seeded soft X-ray laser and a XUV-laser plasma source.

Reconstruction of spatial properties

From the recorded images, different properties of the beam could be reconstructed. The first step is to extract the intensity profile of the radiation. A Fourier transformation of each pattern is made and the intensity for the zero-frequency in Fourier space gets extracted from each spacing d. This intensity represents the summed up intensities I_1, I_2 which transmitted through each pinhole, respectively. Assuming I_1 = const., because one pinhole is stationary, I_2 at each point is known, because at d = 0 I_1 equals I_2. The intensity profile is used for calculating the coherence length. Therefore the maximal visibility V of the pattern is extracted and used to calculate the modulus of the degree of coherence |μ|:

$$|\mu|(d) = \frac{I_1+I_2(d)}{2\sqrt{I_1 I_2}}\, V \qquad (1)$$

Using an appropriate fit function the curve of |μ| is recovered and the coherence length could be determined, i.e. the distance at which the value of |μ| drops down to a certain value [4]. Using van-Cittert-Zernike-theorem the coherent area of the radiation could be extracted and by backpropagation the coherent part of the source could be approximated. The Rayleigh-length and the wavefront curvature are further spatial properties, which could extracted out of phase and intensity profile along the optical axis, by using the correspondent linear stage.

References

[1] M. Bates, S. A. Jones, X. Zhuang, Cold Spring Harbor Protocols 2013, pdb.top075143 (2013).

[2] D. T. Lloyd, K. O’Keeffe, S. M. Hooker, Opt. Lett. 38, 1173 (2013).

[3] D. T. Lloyd, K. O’Keeffe, P. N. Anderson, S. M. Hooker, Scientific Reports 6, 30504 (2016).

[4] P. Salires, A. L. Huillier, M. Lewenstein, Physical Review Letters 74, 3776 (1995).

Single shot imaging with an intense femtosecond soft X-ray Laser

F. Tuitje[1,2], T. Helk[2], M. Zürch[1,2], S. Sebban[3], C. Spielmann[1,2]

[1] Helmholtz Institute Jena, 07743 Jena, Germany

[2] Institute of Optics and Quantum Electronics, Abbe Center of Photonics, 07743 Jena, Germany

[3] LOA, ENSTA, CNRS, Ecole Polytechnique, Université Paris-Saclay, F-91762 Palaiseau cedex, France

We report single shot nanoscale lensless imaging with a femtosecond soft X-ray Laser (SXRL), seeded by a high harmonic XUV pulse. We perform ptychographic imaging to recover the wavefront of the SXRL and employ this to study the seeding properties of the SXRL.

Introduction

Plasma based soft X-ray lasers are high brilliance table-top light sources emitting at intensities allowing in principle single shot imaging, however, the limited spatial coherence usually emerging in the SASE scheme hamper applications in diffraction imaging [1]. In turn, sources based on high harmonic generation (HHG) exhibits excellent coherence properties at relatively low flux. HHG-seeded plasma based SXRL are, thus, ideally combining high flux and excellent beam properties such as high spatial and temporal coherence and short pulse durations [2]. Therefore this kind of source appears to be in ideal choice for high resolution lensless imaging. We use spatial wave front diagnostics by ptychographic reconstruction of the incoming wave front to image the illumination at the sample position. Single-shot reconstructions of binary artificial samples demonstrate the capabilities of the HHG-seeded SXRL.

Experiment and Results

The experiments were conducted at the Laboratoire d'Optique Appliquée with the 'Salle Jaune' Ti:Sapphire laser system used for creating a plasma waveguide, pumping it and generating the seed pulse. As an amplifying medium, Kr8+ ions were used emitting at 32.8 nm. The seeding high harmonic pulse was generated from an Argon filled gas cell resulting in 2 µJ pulse energy per shot. The amplified pulse was separated from the fundamental beam by aluminium filters and reimaged onto the sample by optimized curved multilayer mirrors with a demagnification of 1:10. As seen in Fig. 1b (inset), a gold coated silicon-nitride membrane with an ion beam etched bar structure was used for CDI. The diffraction pattern (Fig.1a) was captured with a single shot of several 100 fs pulse duration. For ptychographic beam sampling, sample consisting of a gold layer of 200nm thickness with regular holes of 0.6 µm diameter and 1 µm pitch was used as seen in Fig. 1c (inset). The sample was raster scanned in a spiral pattern of 30 scan points with an overlap of 90 % and a probe diameter of approx. 5 µm. The resolution achieved at an NA of 0.2 is in the order of ~100 nm.

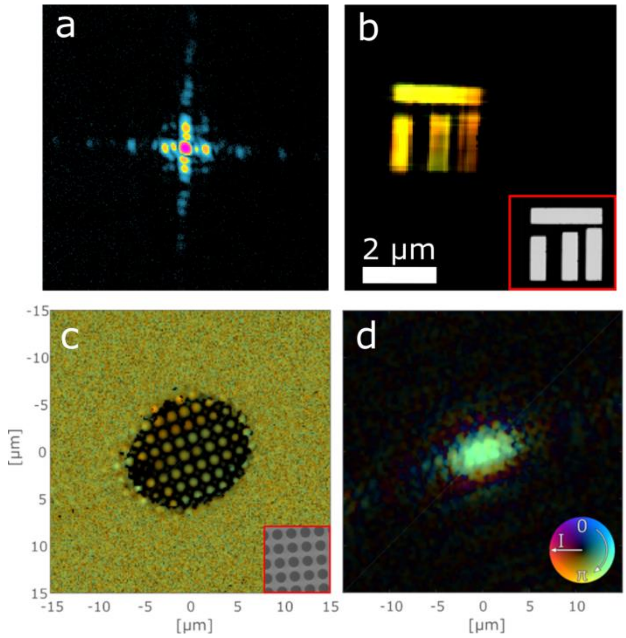

Figure 1: Single shot diffraction pattern (a) and corresponding reconstruction (b), the inset shows a SEM image of the object. The ptychographic reconstructed periodic object (c) shows the periodic hole structure as seen in the inset. The reconstructed illumination function (d) shows an elliptic shape with the largest diameter (FWHM) of ~5 µm. The complex- valued reconstructions are color-coded as amplitude and phase as shown in the inset of (d).

References

[1] M. Zürch, R. Jung, C. Spaeth, J. Tümmler, A. Guggenmos, D. Attwood, U. Kleineberg, H. Stiel, C. Spielmann, ”Spatial Coherence Limited Coherence Diffraction Imaging using a Molybdenum Soft X-ray Laser Pumped at Moderate Pump Energies,” Scientific Reports 7, 5314 (2017)

[2] A. Depresseux, E. Oliva, J. Gautier, F. Tissander, J. Nejdl, M. Kozlova, G. Maynard, J. P. Goddet, A. Tafzi, A. Lifschitz, H. T. Kim, S. Jacquemot, V. Malka, K. Ta Phuoc, C. Thaury, P. Rousseau, G. Iaquaniello, T. Lefrou, A. Flacco, B. Vodungbo, G. Lambert, A. Rousse, P. Zeitoun, S. Sebban, “Table-top femtosecond soft X-ray laser by collisional ionization gating,” Nature Photonics 9, 817 (2015)

Forschergruppe: XUV technology and methods for imaging with nanoscale resolution

S. Fuchs[1,2]*, G.G. Paulus*[1,2]*, F. Tuitje*[1,2]*, M. Zürch*[1,2]*, C. Spielmann*[1,2]*, M. Tschernajew*[1,3]*, J. Rothhardt*[1,3]*, J. Limpert*[1,3]*, M.O. Herdrich*[1]*, G. Weber*[1]*, T. Stöhlker*[1,2]

[1]Helmholtz Institute Jena, Jena, Germany; [2]Institute of Optics and Quantum Electronics, Friedrich Schiller University Jena, Jena, Germany; [3]Institute of Applied Physics, Friedrich Schiller University Jena, Jena, Germany

At the Helmholtz Institute Jena, the research collaboration "Forschergruppe: XUV imaging", funded by the Thüringer Aufbaubank (TAB), combines various expertise in different fields of XUV technology inside the institute to enable nanoscale three-dimensional imaging on a lab scale. In the following, we present the most important advances in the different areas of the collaboration in 2017.

Source development

The recent years of high harmonic generation (HHG) based XUV source development have established highly efficient sources with photon fluxes of above 1E14 ph/s in the < 100 eV range. However, having high power densities, the main challenge remains to separate the generating laser beam from the XUV radiation. We worked on a power scalable solution using an annular driving beam ["Separation of High Average Power Driving Lasers from Higher Order Harmonics Using an Annular Beam", R. Klas et al.]. The key feature is the generation of HHG in the inner cone of the driving beam. This method offers an efficient and wavelength-independent way to block the fundamental radiation using a pinhole, without influencing the generated HHG beam. Furthermore, the phase matching conditions were fully investigated to compare them with the conditions that occur in a Gaussian driving beam, to ensure an optimum generation regime.

Coherent Imaging

To show the excellent quality of the generated XUV radiation, we established a Fourier transform holography imaging experiment ["Table-top and high-resolution Fourier transform holography", W. Eschen et al.]. In comparison to CDI, the phase information of the incoming beam is maintained in the diffraction pattern, due to reference holes in the sample. This enables straight-forward sample reconstruction. Using a wavelength of 18 nm, the physically possible resolution of 34 nm, given by the size of the reference holes, was reached. This is the highest resolution so far at any light source, using the Fourier transform holography method.

We furthermore report on single shot lensless diffraction imaging of nanostructures with a HHG seeded femtosecond soft X-ray Laser at LOA (ENSTA Paris). Plasma based X-Ray lasers are known for their high brilliance and high intensity. But they typically suffer from shot-to-shot variations in the wave front due to fluctuations in the amplifying plasma [1]. On the other hand, light sources which use high harmonic generation deliver short and stable pulses. However, the intensities are rather low which ultimately results in long integration times. The combination of both techniques, namely a HHG seeded plasma based soft X-ray laser, leads to excellent beam properties and short pulse durations. With such a source, we were able to capture single-shot diffractograms with exposure times down to several hundred femtoseconds. We then reconstructed the object in intensity and phase with a resolution of approx. 120 nm.

Coherence Tomography

We report on major advances of XUV Coherence Tomography (XCT), which enable artifact-free three-dimensional imaging of nanoscale objects. XCT is the XUV equivalent of Optical Coherence Tomography (OCT). By using the broad bandwidth of high harmonics of femtosecond laser pulses the axial resolution of XCT can reach a few nanometers [2]. However, the typically modulated HHG spectra need to be transformed into a continuous spectrum by averaging HHG spectra generated with slightly shifted fundamental frequencies [3]. A challenge for XCT is the reconstruction of the sample structure from the measured intensity reflectivity, as the backtransform without knowledge of the phase information leads to artifacts in the reconstructed image. This problem has recently been addressed by implementing a novel one-dimensional phase retrieval algorithm, which has ultimately led to the artifact-free reconstruction of three-dimensional samples [4] (see figure 1).

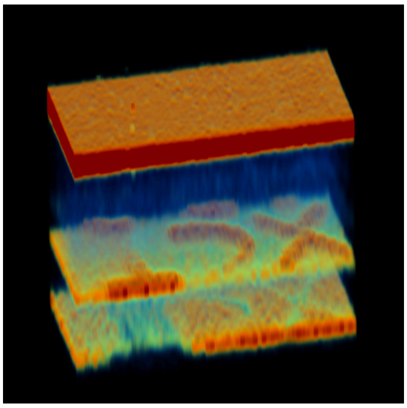

Figure 1: XCT tomogram of a silicon-based sample. The axial resolution is 20nm. The reconstructed image is free of former artifacts and shows the three-dimensional sample structure.

References

[1] M. Zürch et al., Scientific Reports 7 (2017) 5314.

[2] S. Fuchs et al., Scientific Reports 6 (2016) 20658.

[3] M. Wünsche, S. Fuchs et al., Optics Express 25 (2017) 6936-6944.

[4] S. Fuchs et al., Optica 4 (2017) 903-906.

Simulation and LIGA fabrication of planar parabolic γ-ray refractive gold lenses

N. Sahraei[2], M. M. Günther[1], M. Jentschel[4], M. Steglich[2], M. Fritz[3], S. Merx[2], A. Bund[3], H. Gross[2], E.-B. Kley[2], A. Tünnermann[2], and U. Zeitner[2]

[1]HI Jena, Germany; [2]IAP, Jena, Germany; [3]TU-Ilmenau, Ilmenau, Germany; [4]ILL, Grenoble , France

The results of optical simulation taking dispersion and absorption into account suggest that there is a possibility of focusing γ-rays via refractive lenses. Based on these results, planar parabolic compound refractive gold lenses were designed for energetic γ-rays. These lenses were fabricated by LIGA technology. Both focal lines and focal spots can be achieved using these lenses.

Motivation and method

NRF analysis is one of the recent application of focused energetic γ-rays. Michael Jentschel et al. have developed an NRF based radiography system, capable of performing a non-destructive assay of material with microgram precision and micrometer spatial resolution [1]. A nanogram precision and nanometer spatial resolution can be achieved by adopting focusing refractive lenses in NRF analysis system. However, there has been no report on simulation or fabrication of refractive lenses for γ-rays. Recently Marc Günther et al. [2] have performed a series of experiments validating theoretical values for refractive index experimentally for Si at energies of $200keV$ to $2MeV$. Being inspired by these results a simulation study on the possibility of focusing γ-rays via refractive lenses was conducted.

The refractive index in γ-ray range can be written as $n(E) = 1 + \delta(E) + i\beta(E)$ where $1 + \delta(E)$ and $\beta(E)$ are representing respectively refractive and absorptive parts of the refractive index. δ and β can be written as:

$$\delta = -Z r_0 2\pi \frac{(\hbar c)^2 N_A \rho}{E^2 A}, \tag{1}$$

$$\beta(E) = \frac{\mu\lambda}{4\pi}, \quad \mu(E) = \frac{\sigma(E)\rho N_A}{A}, \tag{2}$$

Where Z is the atomic number, r_0 is the classical scattering length of one electron, E the photon energy, A the atomic mass, and $\mu(E)$ represents the overall attenuation coefficient. In optical design, only the effect of photo-absorption on $\mu(E)$ was taken into account.

Considering the thin lens approximation with some corrections a focal length of few meters can be achieved by adopting a stack of N biconcave lenses or Compound Refractive Lens (CRL). Ni CRLs have been tested for energies as high as $212keV$[3]. Planar parabolic CRLs with $R = 5\mu m$ were taken as initial lens geometry. According to the simulation, for higher energies, Au and W CRLs are capable of focusing γ-rays efficiently. An Au CRL with N=30 and $R = 5\mu m$ in a linear and crossed geometry was designed, and a focal line and spot respectively at $478keV$ energy with a focal length of approx. $6m$ was achieved.

The designed Au CRL was fabricated by LIGA method. For this purpose, first, a working mask with the CRL pattern consisting of an AZ 125 nXT photoresist layer with thickness of $180\mu m$ that was structured and developed on a Si wafer coated with $200nm$ Au was fabricated. As the next step Au was electro-deposited on the working mask. The Au deposition duration was 9:20 h at galvanic bath temperature of $72°C$ with the current density of $0.5A/dm^2$. With this method Au CRLs with the minimum structure height of approx. $100\mu m$ with tapered sidewalls with a deviation angle of $1 - 3°$ from vertical geometry were characterized. Considering simulation results such tapered sidewalls can deteriorate the lens focusing quality, but the CRL is still capable of focusing light despite such fabrication errors.

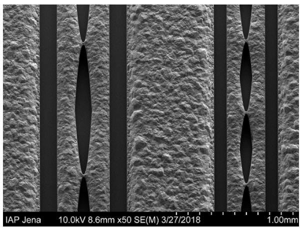

Figure 1: An SEM overview of planar parabolic Au CRL.

Conclusion

According to the numerical simulation results, Au and W CRLs are capable of focusing γ-rays. Therefore planar parabolic Au CRL for $478keV$ energy was designed and fabricated via LIGA method. The simulation results for the Au CRL with tapered sidewall suggests that focusing of γ-rays in spite of fabrication errors such as tapered sidewalls with certain angles is possible. The optical performance of the lenses will be soon investigated via a series of experiments in a beamline facility.

References

[1] Jentschel, M et al., “Isotope-selective radiography and material assay using high-brilliance, quasi-monochromatic, high-energy photon”, 2015

[2] Günther, M. M. et al. “Refractive-index measurement of Si at γ-ray energies up to 2 MeV”, Phys. Rev. A, vol 95, issue 5, 053864, May 2017

[3] Nazmov, V et al. “LIGA fabrication of X-ray Nickel lenses”, Microsystem Technologies, 11 (2005) 292–297, Springer-Verlag 2005

Dependency of the refractive index from atomic charge number Z at γ-ray energies up-to 2 MeV

M. M. Günther[*][1,2], *A. V. Volotka*[1], *M. Jentschel*[3], *P. G. Thirolf*[4], *and M. Zepf*[1]
[1]HI Jena, Jena, Germany; [2]GSI, Darmstadt, Germany; [3]ILL, Grenoble, France; [4]LMU, Garching, Germany

The index of refraction was investigated experimentally as well as theoretically for Materials with atomic charge number from $Z = 4$ (beryllium) to $Z = 82$ (lead). The results were compared with theoretical calculations. We found a good agreement between experiment and theory (Fig.1). For an applied point of view in case of the feasibility of refractive optics the results show that high-Z materials become increasingly attractive compared to established low-Z materials used in X-ray applications (Fig.2). For a detailed description see Günther et al. [1].

The investigation of basic optical properties of matter irradiated with visible light is of crucial importance for the development of optics in industrial as well as scientific applications. The discovery of X-ray radiation by Wilhelm-Konrad Röntgen and the subsequent development of X-ray radiation sources during the last century, opened a new field in optics and optical applications. The evolution towards modern brilliant X-ray sources such as synchrotrons made the investigation of the optical properties of materials up to about 100 keV possible. This allowed for the development of novel diffractive as well as refractive optics.

To date, the theoretical description of the optical behaviour of materials has been validated experimentally in the X-ray energy regime from several hundreds of eV up to tens of keV. For γ-ray energies up to several MeV no experimental tests to verify the theory of the refractive index have been performed so far.

From an application point of view, it is important to validate the classical approximation up to the γ-ray energy regime. To investigate the refractive index at γ-ray energies it needs sophisticated experimental instrumentation, because the effect is expected to be very tiny. First measurements of the refractive index of silicon at γ-ray energies was performed by Habs et al. [3, 4]. Subsequent experiment beam times [2] showed that the conclusions drawn from the experimental results needed to be corrected at high energies due to a systematic error that had not been accounted for. A detailed discussion, including new results of the refractive index measurements of silicon, is presented in [2].

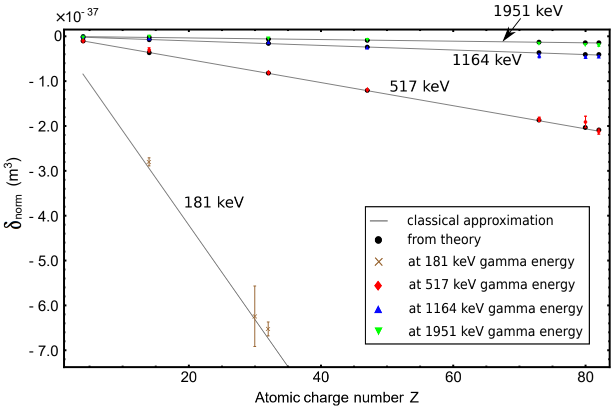

Figure 1: The normalized real part δ_{norm} of the complex index of refraction as a function of the atomic charge number Z. The Z dependence is shown for different photon energies E_γ (181 keV, 517 keV, 1164 keV, and 1951 keV). A slight deviation of δ_{norm} from the classical theory is observed at energies above 517 keV. The black dots are calculated δ_{norm}*'s* from theory. The gray dotted line is an interpolation of the classical approximation over the measured atomic charge range.

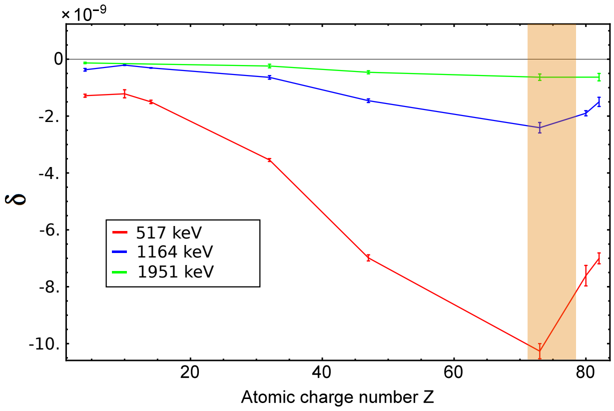

Figure 2: Z dependence of the measured δ for three different photon energies. The shaded area highlights the range of materials with maximum mass density.

References

[1] Günther, M. M. et al. “Dispersive refraction of different light-to-heavy materials at MeV γ-ray energies”, arXiv:1804.10061v1 [physics.atom-ph] (2018) (submitted to Phys. Rev. A)

[2] Günther, M. M. et al. “Refractive-index measurement of Si at γ-ray energies up to 2 MeV”, Phys. Rev. A, vol 95, 053864 (2017)

[3] Habs, D. et al. “Refractive Index of Silicon at γ Ray Energies”, Phys. Rev. Lett., vol 108, 184802 (2012)

[4] Habs, D. et al. “Erratum: Refractive Index of Silicon at γ Ray Energies”, Phys. Rev. Lett., vol 118, 169904 (2017)

---

[*] m.guenther@gsi.de

Investigations of different types of current coupling for the new Cryogenic Current Comparator with eXtended Dimensions (CCC-XD)*

V. Tymppel[1], R. Neubert[2], Jessica Golm[2], and the FAIR@GSI Beam Instrumentation R&D group

[1]Helmholtz Institute, Jena, Germany; [2]Institute of Solid State Physics, Jena, Germany

The FAIR project triggers the development of CCCs with larger diameters for the non-destructive, highly-sensitive measurement of charged particle beam intensities. Before the final acceptance test in May 2017 [Fig. 1] different types of current coupling were investigated.

Figure 1: CCC-XD in a wide neck cryostat in front of the magnetic shielded chamber in Jena (l. to r: R. Neubert, T. Sieber, F. Kurian, V. Tympel).

Different types of current coupling

Inside the so-called SQUID-Cartridge the low inductance of the SQUID (Superconducting Quantum Interference Device) has to be coupled with the high inductance of the pickup coil capturing the magnetic field of the charged particle beam. As shown in Fig. 2 three types of coupling were simulated: direct (black), balanced (red) and enhanced (blue). Using the measured inductance values from [1] the simulation shows that the parasitic capacity of the CCC meander shielding leads to resonance peaks above 100 kHz [Fig. 3]. Especially the direct version which is without any matching transformer has a strong peak. A transformer dimensioned with higher inductance values (balanced, enhanced) can generate an additional current magnification at the expense of the bandwidth.

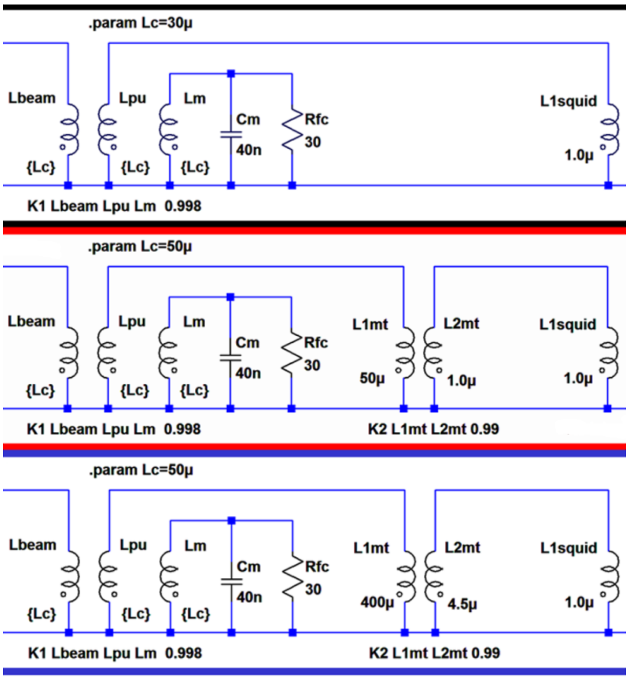

Figure 2: Circuit diagrams of the three coupling types.

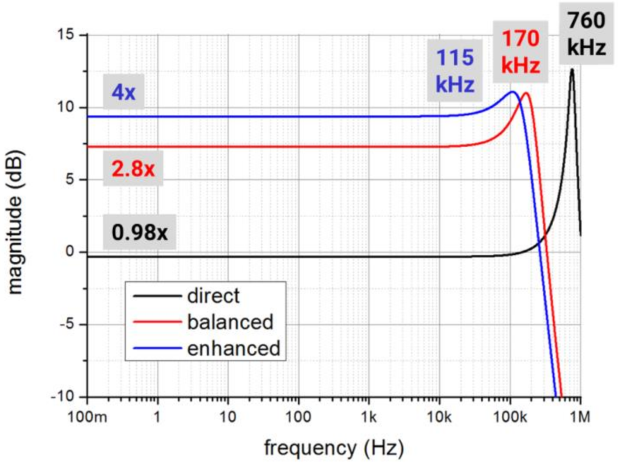

Figure 3: LTspice simulation of the coupling types [2].

Measurement results

The CCC-XD measurements, done in Jena, established that the flux concentrator core surrounded by the pickup coil is the dominant source of current noise. An additional current magnification in front of the SQUID is not necessary. The calculated bandwidths und resonances could be measured. To realize a stable flux-locked-loop working mode with the SQUID the high resonance peak of the direct version has to be damped. Therefor the balanced version was used at the end. This research is supported by the BMBF (project# 05P15SJRBA), the TU Darmstadt and the Leibniz Institute of Photonic Technology.

References

[1] V. Tympel et al., “The next generation of cryogenic current comparators for beam monitoring.”, proceedings of IBIC’16, Barcelona, Spain, pp. 441-444, ISBN 978-3-95450-177-9

[2] V. Tympel et al., “Cryogenic Current Comparators for 150 mm Beamline Diameter,” IBIC’17, Grand Rapids, MI, USA, Aug. 2017, paper WEPCF07, in press.

---

* also published in GSI-FAIR Scientific Report 2017

The XUV-comb project at HI Jena/DESY

P. Pfäfflein[1,2]*, Sarper Salman*[2]*, Chen Li*[2]*, Lutz Winkelmann*[2]*, I. Hartl*[2]*, C. M. Heyl*[1,] *and collaborators at DESY/University of Vienna/University of Neuchâtel*

[1]HI Jena, Germany; [2]DESY, Germany

This progress report outlines the initial phase of a new project at HI Jena/DESY, started in October 2017. The extreme ultraviolet (XUV) frequency comb project aims to strengthen the research profiles of both HI Jena/GSI and DESY on state-of-the-art photon sources and spectroscopy as well as the collaboration between the two institutes. In the current starting phase, an XUV frequency comb source is being set up. The source will provide new parameter regimes for both, ultrafast and ultra-high precision spectroscopy including new possibilities for the test of quantum electrodynamics via highly charged ion spectroscopy. We here give a very brief introduction into the underlying technology and the first implementation efforts at DESY.

Following the spectral extension of frequency comb technology via high-order harmonic generation (HHG) into the XUV in 2005 [1,2], a multitude of development steps have recently led to XUV-comb systems with up to mW-level generated average power per high harmonic order [3]. A central method of the underlying technology is the generation of high harmonics in gases, driven by a passively enhanced high-power femtosecond laser system. In contrast to traditional single-pass HHG schemes where intense laser pulses are simply focussed into a gas medium, the frequency conversion process takes place in a gas medium placed inside an optical resonator. This way, the driving laser pulses can be "recycled" as each pulse is superimposed with the next incoming pulse. Our efforts will employ the established intra-cavity generation method for XUV comb generation together with new concepts, aiming to push parameters essential for frequency comb spectroscopy such as repetition rate and average power into new regimes.

To enable the formation of XUV frequency comb lines, i.e. thousands of spectrally narrow CW-lasers lines inside each harmonic order, a stable operation of the driving laser system is of crucial importance [4]. Following this demand, we are currently setting up a highly stable Ytterbium-fiber based frequency comb oscillator, based on the so-called figure-of 9 design [5]. A work-in progress view of the oscillator is shown in Fig. 1, together with a first spectrum demonstrating mode-locked operation (Fg. 2). Stable operation of the oscillator will be ensured by employing a fiber-based loop-mirror design as well as new concepts for carrier-envelope frequency stabilization. The laser pulses will then be amplified in a multi-stage amplifier system to reach an average power of approximately 100 W and a pulse width below 200 fs. Possible post-compression and frequency conversion stages may be added and subsequently the laser pulses will be sent into a passive HHG cavity placed inside a vacuum system. In parallel to these laser development efforts, vacuum- and cavity system are currently being designed and built.

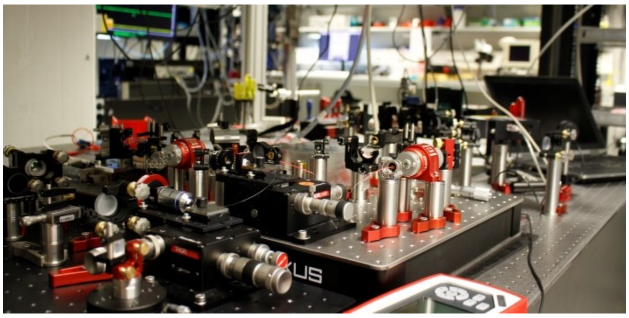

Figure 1: Work-in-progress view of the Ytterbium fiber oscillator setup and an f-2f interferometer for carrier-envelope frequency detection. A compact version of this oscillator will be used for a high-power frequency comb system.

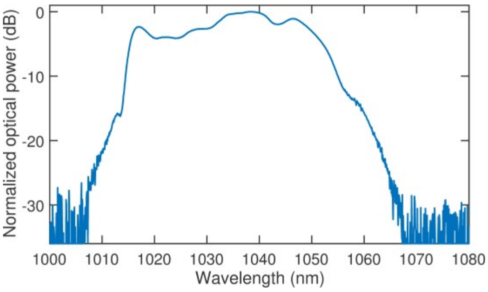

Figure 2: Oscillator spectrum demonstrating mode-locked operation of the test oscillator.

In conclusion, the XUV comb project at HI Jena/DESY is currently in its start phase in which a new high repetition rate XUV source is being set up, providing new possibilities for various experiments at the border between ultrafast and ultrahigh precision physics.

References

[1] R.J. Molls et al., "Phase-coherent frequency combs in the vacuum ultraviolet via high-harmonic generation inside a femtosecond enhancement cavity", Phys. Rev. Lett. 94, 193201 (2005).

[2] C. Gohle et al. "A frequency comb in the extreme ultraviolet", Nature 436, 234–237 (2005).

[3] G. Porat, C.M. Heyl, S.B. Schoun, C. Benko, N. Dörre, K.L. Corvin, J. Ye, “Phase-matched extreme-ultraviolet frequency-comb generation”, arXiv:1710.04314 (2017).

[4] C. Benko et al., “Extreme ultraviolet radiation with coherence times greater than 1 s”, Nature Phot. 8, 530 (2014).

[5] W. Hänsel et al., "All polarization-maintaining fiber laser architecture for robust femtosecond pulse generation", Appl. Phys. B. 123:41 (2017).

Theory

An efficient method to calculate the complex $\vec{k}$-space from simulation data

Alexander Blinne[1], *Stephan Kuschel*[1,2], *Stefan Tietze*[1], *and Matt Zepf*[1,2,3]
[1]Helmholtz Institute Jena, Fröbelstieg 3, 07743 Jena, Germany; [2]Institute for Optics- and Quantumelectronics, Friedrich Schiller University Jena, Max-Wien-Platz 1, 07743 Jena, Germany; [3]Department of Physics and Astronomy, Queen's University Belfast, Belfast, BT7 1NN, UK

A novel method for the analysis of real-valued electromagnetic field data from simulations is presented in this paper. Reconstructing the complex k-space is often deemed too complicated and not expected to give much insight. With the new method presented here this changes, as it is a simple and efficient method to gain access to the full physical information of the electromagnetic fields from a single data dump. This allows counterpropagating plane waves to be accurately distinguished and to compute their complex coefficients independently. From these amplitudes, the complex-valued electromagnetic fields can be calculated from which information about phase and amplitude is readily available. Additionally, the complex fields allow for efficient vacuum propagation allowing to calculate far field data or boundary input data from near field data. An implementation of the new method is available as part of PostPic [1], a data analysis toolkit written in the Python programming language.

In the one-dimensional case it is obvious, that the waves propagating in either direction can be separated using information from only a single dump by the linear combinations

$$E_y^+ = \frac{1}{2}\left(E_y + cB_z\right) \qquad E_y^- = \frac{1}{2}\left(E_y - cB_z\right) ,$$

which is true in both, spatial domain and frequency domain. We show, that it is possible to extend this method into the three dimensional frequency domain and separate the incident and outgoing waves in the data using just a single dump. This is different from a simple Fourier transform of the real data where the amplitudes for $\vec{k}$ and $-\vec{k}$ would be Hermitian conjugates making both propagation directions indistinguishable, which is not the case in the reconstructed, complex $\vec{k}$-space. Here, the amplitudes for $\vec{k}$ and $-\vec{k}$ are completely independent and refer directly to plane waves propagating in either direction with known amplitude and phase.

Starting from a spectral ansatz for the vector potential in radiation gauge $\nabla \cdot \vec{A} = \varphi = 0$

$$\vec{A}(\vec{r}, t) = \int \mathrm{d}^3k \sum_{i=1,2} \mathbf{a}_i(\vec{k})\hat{e}_i(\hat{k})e^{i\left(\vec{k}\cdot\vec{r} - \omega_0(\vec{k})t\right)} ,$$

we find the complex $\vec{k}$-space amplitudes

$$\vec{\mathbf{E}}_{\vec{k}} = \frac{1}{2}\left(\vec{\mathbf{E}}^{\mathrm{F}}_{\vec{k}} - c\hat{k} \times \vec{\mathbf{B}}^{\mathrm{F}}_{\vec{k}}\right)$$
$$\vec{\mathbf{B}}_{\vec{k}} = \frac{1}{2}\left(\vec{\mathbf{B}}^{\mathrm{F}}_{\vec{k}} + \frac{1}{c}\hat{k} \times \vec{\mathbf{E}}^{\mathrm{F}}_{\vec{k}}\right) ,$$

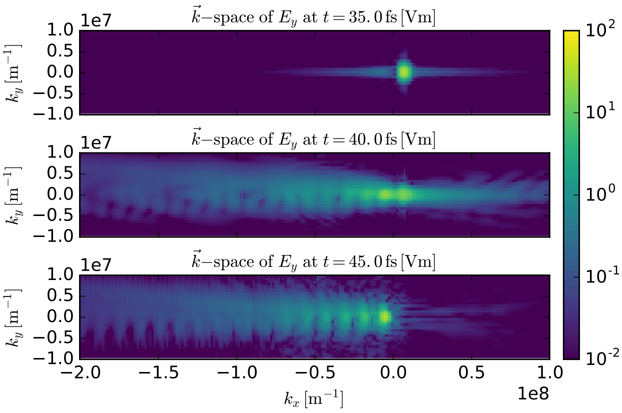

Figure 1: Data from a simulation of surface high harmonic generation. Magnitude of the reconstructed $\vec{k}$-space in the beginning, middle and at the end of the interaction, from top to bottom.

where $\vec{\mathbf{E}}^{\mathrm{F}}_{\vec{k}}$ and $\vec{\mathbf{B}}^{\mathrm{F}}_{\vec{k}}$ denote the hermitian output of a real-valued Fourier transform of the fields as taken from the simulation.

Using the above equations on their own yields results which suffer from numerical artifacts, that may need special care. For example the EPOCH code [2] uses a split-step method that produces a double leapfrog scheme, in order to output both fields at the same point in time. These half-step fields output by EPOCH are basically the result of a linear interpolation. This operation can be represented in frequency domain by multiplying with the discrete Fourier transform of a kernel and a linear phaseaccounting for the translation, resulting in

$$R(\omega) := \frac{FT\{\tilde{f}\}(\omega)}{FT\{f\}(\omega)} = \cos\left(\tfrac{1}{2}\omega\,\Delta t\right) ,$$

in case of an interpolation by one half step. This frequency response $R(\omega)$ is implicitly contained in any field that is produced by linear interpolating the Fields from neighbouring steps and it is necessary to remove it, in order to obtain an accurate $\vec{k}$-space.

References

[1] S. Kuschel, PostPic python package `http://www.github.com/skuschel/postpic`

[2] T. D. Arber, K. Bennett, C. S. Brady et al., Plasma Phys. Control. Fusion **57 (11)**, 113001 (2015)

Intense laser compression to a duration of ≤ 5fs by laser-gas interaction

Y. X. Zhang[1,2], *S. Rykovanov*[1], *M. Zepf*[1]

[1]Helmholtz Institute Jena, Germany; [2]Peking University, Beijing, 100871, China.

Spectrum broadening and self-compression processes realized by laser-gas interactions will be investigated through theoretical analysis and particle-in-cell simulations. By using two gas jets with different parameters, such as different density distributions, a tens of femtosecond laser pulse with relativistic intensity can be compressed to a one-cycle (or two) laser pulse.

Introduction about the work

Few-cycle laser pulses, especially one or two-cycle pulses, at relativistic intensities has been demonstrated particularly efficient to generate high-energy isolated attosecond pulses. Such intense single attosecond pulses will open the door to nonlinear processes in XUV or X-ray spectra region with attosecond resolution. Generation such pulses requires high energy ultra-short duration laser pulses with a high quality bean spatial profile. However, at kHz repetition rate, it has been proven difficult to obtain few-cycle laser pulses with more than a few millijoules. Although conventional Ti:sapphire based amplifier systems are currently able to generate laser pulses at joule level energies, the pulse duration is typically limited to 25fs or even greater by the gain-narrow effect in the amplifier medium and imperfect dispersion compensation . To obtain an isolated attosecond pulse, a laser pulse with duration ≤ 5 fs should be satisfied. Therefore, post-compression is necessary to broaden the spectrum of the laser field, further decreasing the duration of the intense laser down to at least 5fs, and we try to realize the processes by laser-gas interactions.

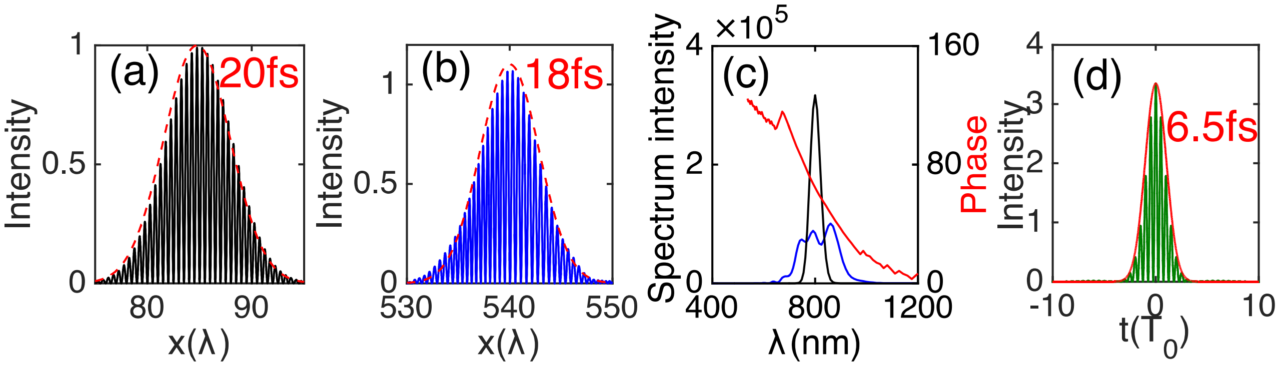

Figure 1: 1D simulation results for the first stage. (a) Initial laser pulse with a duration of 20fs and $a_0 = 1$ (normalized field). (b) Transmitted pulse which is almost not compressed. (c) The spectrum or the initial (black color) and transmitted (blue color) light and spectral phase for the transmitted one (red), which shows that the spectrum has been broadened and a chirped phase has been induced. d) The Fourier transform limited pulse is about 6.5fs with intensity being enhanced.

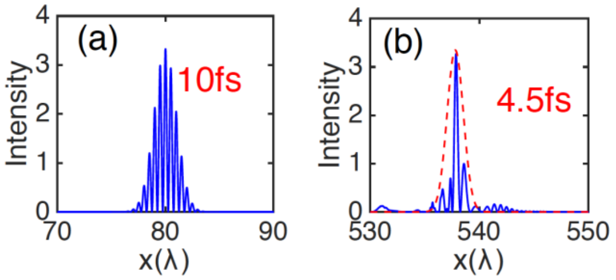

Figure 2: 1D simulation results for the second stage that a 10fs pulse has been self-compressed to 4.5fs.

In this program, we propose to compress a high-energy laser pulses with duration >20fs to about 5fs at hundreds of millijoules (or even several joules) by two steps. In the first step, a gas jet with a lower density is used to broaden the spectrum for post-compression, so that an intense pulse with duration of about 10fs can be obtained (See Fig. 1). In the second step, a secondary gas jet will be used to compress the ~10fs pulse to ~5fs by the temporal self-compression process (See Fig. 2). The influence of different laser and parameters (laser intensities, durations, focal positions, focal sizes, gas types, peak densities, spatial profiles and lengths) will also be discussed and the spatial inhomogeneous, spatio-temporal couplings and transverse instabilities of laser pulses will be addressed by simulation works.

References

[1] Z. H. He, J. A. Nees, B. Hou, K. Krushelnick, and A.G.R. Thomas, Phys. Rev. Lett. 113, 263904(2014).

[2] B. Beaurepaire, D. Guénot, et. al., Opt. Express 9(24), 9693-9705 (2016).

[3] J. Schreiber, C. Bellei, et. al., Phys. Rev. Lett. 105, 235003 (2010).

Influence of surface denting on the attosecond lighthouse effect

S. Tietze[1,2], *J. Bierbach*[1,2], *M. Zepf*[1,2,3], *and S. G. Rykovanov*[1]
[1]Helmholtz Institut Jena, Germany; [2]Friedrich-Schiller-Universität Jena, Germany; [3]Queen's University Belfast, UK

An intense laser pulse shining on a solid target generates high order harmonics of the central laser frequency. This process is called surface high harmonic generation (SHHG) and has been extensively studied in theory and experiment [1]. In general, this process generates a train of attosecond pulses in the XUV and X-ray regime. For many possible applications in biology and chemistry isolated attosecond pulses are preferable [2]. A novel method to spatially separate single attosecond pulses has been proposed as the attosecond lighthouse effect [3, 4]. The incident laser pulse exhibits spatio-temporal couplings, namely wave-front rotation, in focus (Fig. 1). Rotating wavefronts lead to the emission of attosecond pulses under an angle an thus to separate pulses far away from the target. With the EPOCH code [5], we performed two dimensional PIC simulations of this effect. The correct implementation of the laser pulse with wavefront rotation is crucial for this kind of simulations. We developed a way to include laser pulses with arbitrary spatio-temporal couplings using the Kostenbauder matrix formalism [6]. The PIC simulations were then used to study the influence of laser pressure induced surface denting on the lighthouse effect. By varying the scale length of the target, the amount of denting can be controlled. For SHHG, it has already been shown that surface denting introduces a chirp in the reflected XUV pulse. However, the influence on the lighthouse effect has not been investigated yet. Our simulations show that surface denting leads to a reduced spatial separation of the pulses in a pulse train (Fig. 2). The wave fronts of the single pulses are tilted in different directions, which indicates that the pulses become separated if propagated further. In the reflected pulse's spectrum, the influence of surface denting can be seen as well. The harmonic lines are tilted with respect to the propagation axis. For a single harmonic, this tilt is larger than one harmonic order and the tilt strength increases with the harmonic order. The reason for this effect is the interplay between the surface denting and the wave front rotation of the laser pulse. For higher harmonic orders, a double line structure appears. The origin of this feature is still not fully explained and is subject to ongoing research.

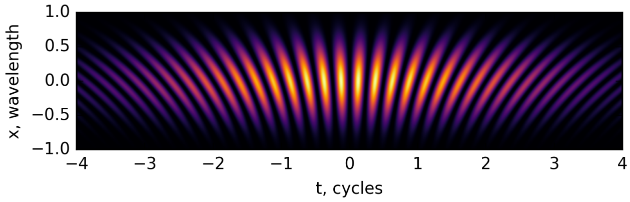

Figure 1: A gaussian laser pulse with wave-front rotation.

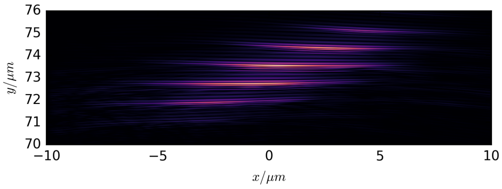

Figure 2: Snapshot of the XUV pulse generated by the attosecond lighthouse after propagation of 70 μm. Laser pulse is propagating in y-direction.

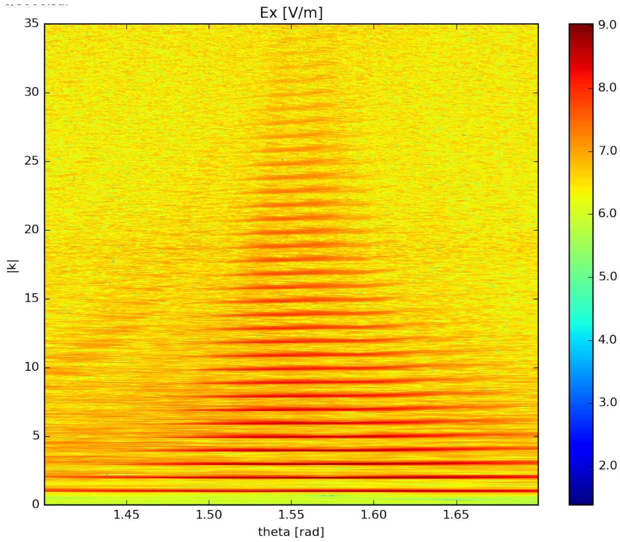

Figure 3: Spectrum of the reflected attosecond pulse.

References

[1] U. Teubner and P. Gibbon, Reviews of Modern Physics **81**, 445 (2009).

[2] R. Neutze *et al.*, Nature **406**, 752–757 (2000)

[3] J.A. Wheeler *et al.*, Nature Photonics **6**, 829-833 (2012)

[4] H. Vincenti and F. Quéré, Physical Review Letters **108**, 113904 (2012)

[5] T.D. Arber *et al.*, Plasma Physics and Controlled Fusion, **57**, 11, 1-26 (2015)

[6] A.G. Kostenbauder, IEEE Journal of Quantum Electronics, **26**, 1148 (1990)

Narrow bandwidth γ-comb from nonlinear Compton scattering using the polarization gating technique

S. G. Rykovanov, M. Ruijter, and V. Yu. Kharin
Helmholtz Institut Jena, Germany

Recently, there has been a revival of interest in the Compton photon sources based on scattering of intense laser pulses from relativistic electron beams. One possible way to increase the source brightness is to increase the intensity of the laser pulses used for scattering. However, due to the temporal shape of the laser pulses, ponderomotive effects (the "slow-down" of electrons due to the $\mathbf{v} \times \mathbf{B}$ force) start playing an important role in electron dynamics and lead to the spectral broadening. Recently, it was proposed to perfectly compensate the ponderomotive broadening by using properly chirped laser pulses, where pulse frequency is a nonlinear function of time exactly following the change of the laser pulse envelope [1]. Here, we propose to compensate the broadening in the harmonics of the fundamental Compton line by using a technique called polarization gating. In this technique the laser pulse is constructed by two circularly and oppositely polarized laser pulses overlapping with each other with some delay. The resulting laser pulse has circular polarization on the wings and linear polarization only in the middle of the pulse as can be seen on Figure 1 (left).

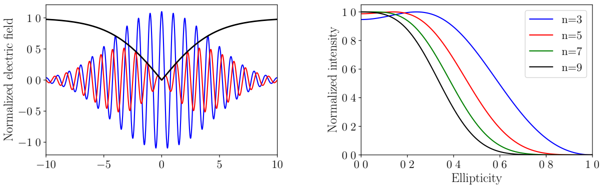

Figure 1: Left: Normalized mutually orthogonal transverse electric field components of the laser pulse (blue and red lines) and the time-dependent ellipticity (black curve, value of zero corresponds to the linear polarization). T_L is the laser pulse period. Right: Normalized on-axis intensity of different harmonic orders as a function of ellipticity for the laser pulse with $a_0 = 3$.

It is well known that intense circularly polarized light does not generate harmonics in the Compton backscattering from energetic electrons, whereas linearly polarized light produces harmonics of the fundamental Compton line [2]. Ellipticity dependence of different harmonic orders on the ellipticity of the scattering laser pulse for the normalized laser pulse amplitude $a_0 = 3$ is shown on Figure 1 (right).

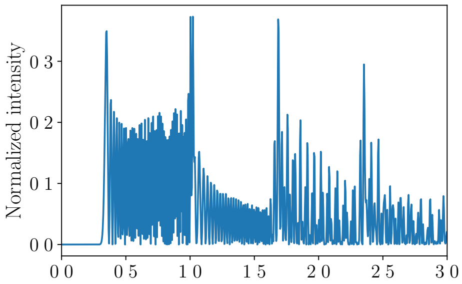

Figure 2: Normalized on-axis radiation spectrum for the case of the linearly polarized laser pulse with $a_0 = 2$ and FWHM duration of 30 laser cycles with no polarization gating technique applied. ω_L is the laser pulse frequency. Electron initially at rest is assumed for simplicity without losing the generality.

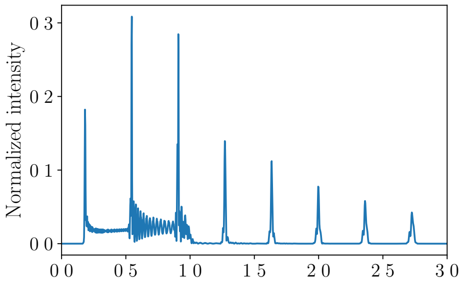

Figure 3: Same as on Figure 2, but with the polarization technique applied.

On-axis radiation spectrum for the linearly polarized gaussian laser pulse with the amplitude $a_0 = 2$ and FWHM duration of 30 laser cycles without the polarization gating technique applied is shown in Figure 2, where one can see the ponderomotive broadening of each harmonic and their overlap. On-axis radiation spectrum for the laser pulse with the same peak a_0 but with the polarization gating technique with the delay of 24 laser cycles is presented on Figure 3. Even though all frequencies below $\omega = \omega_L$ still suffer from ponderomotive broadening, higher harmonics show narrowband comb-like structure.

References

[1] S.G. Rykovanov, *et al.*, Phys. Rev. Accel. Beams, **19**, 030701 (2016)

[2] E.S. Sarachik and G.T. Schappert, Phys. Rev. D, **1**, 2738 (1970)

Analytical solutions for nonlinear Thomson scattering including radiation reaction

M. Ruijter, V. Yu. Kharin, and S. G. Rykovanov
Helmholtz Institut Jena, Germany

Nonlinear Thomson scattering may be used in generating bright high energy photon sources. In the relativistic classical regime, the process can be solved analytically by calculating the trajectory of an electron, and the radiation it emits using classical electrodynamics (CED) [1]. The area of applicability is determined by the parameter $\chi \ll 1$, see Figure 1 for the dependency of χ on the electron's initial energy (γ) and the normalized laser pulse amplitude (a_0).

The emission process is well understood when the motion of the electron is described by the Lorentz force (LF). When the laser intensity increases the emitted radiation affects the motion of the charged particle. This is called Radiation Reaction (RR). Several equations of motion can be found in the literature, but we use the Landau-Lifshitz equation (LL) to calculate the motion of the particle. Exact analytical solutions of the motion when RR is included exist [4, 5]. The exact solutions can be simplified when the incident laser pulse is described as a quasi monochromatic plane wave, with a sufficiently long laser pulse duration[2]. The emitted radiation is calculated by the well known formula for the energy radiated per unit solid angle per unit frequency. Numerical results of the emitted radiation (in the frame where the electron is initially at rest) for a flat top laser pulse envelope are shown in Figure 2. When the motion is described by the LF the electron moves with a constant speed and all the emitted radiation is centered around a single frequency. But when the motion is described with the LL, the electron's velocity increases due to the RR. Therefore the emitted radiation is Doppler shifted differently for specific times and we see a larger bandwidth.

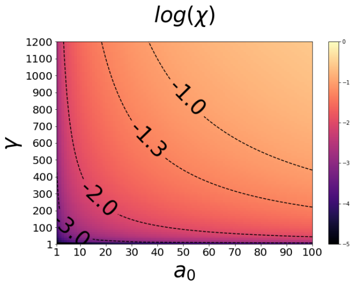

Figure 1: The behavior of the parameter χ on the electron energy (γ) and the normalized laser pulse amplitude (a_0). The emitted radiation can be calculated using CED underneath the -1.3 line.

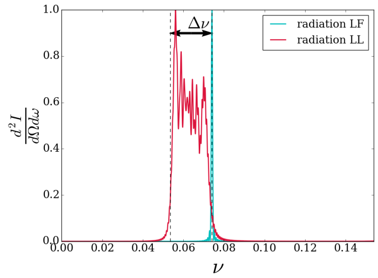

Figure 2: Normalized on-axis radiation for a linearly polarized laser pulse with a rectangular envelope function for the LF and LL case with $a_0 = 5$ and $N_c = 90$, where N_c is the laser pulse duration in laser cycles.

The laser pulse can be chirped in order to compensate the down shift of the frequency as described by [6] in the case of the LF. When the LF chirp condition is used for the LL motion, we find a big difference in the spectra, see Figure 3. This is due to the fact that the velocity depends on the derivative of the vector potential in the case of the LL solution [2]. The chirp condition in case of the LL is a nonlinear implicit equation.

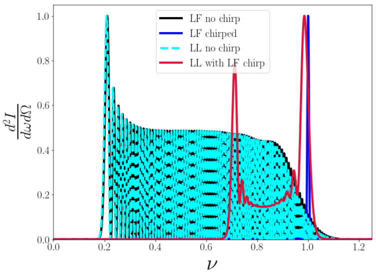

Figure 3: The on-axis radiation spectra for the unchirped and chirped plane wave laser pulses with $a_0 = 2$ and $N_c = 30$ with a sine squared envelope.

References

[1] A. I. Nikishov and V. I. Ritus, Sov. Phys. JETP, **19**, 529-541 (1964)

[2] M. Ruijter, *Relativistic Nonlinear Compton Scattering*, Friedrich-Schiller University, Jena, Germany (2017)

[3] D. Seipt, *et al.*, Journal of Plasma Physics, **82**, 655820203 (2016)

[4] Y. Hadad, *et al.*, Phys. Rev. D, **82**, 096012 (2010)

[5] A. Di Piazza, Letters in Mathematical Physics, **83**, 305–313 (2008)

[6] S.G. Rykovanov, *et al.*, Phys. Rev. Accel. Beams, **19**, 030701 (2016)

Explicit methods for simulation of laser wake generation in tenuous plasma

N. Elkina, V. Yu. Kharin, and S. G. Rykovanov
Helmholtz Institut Jena, Germany

Laser wake field acceleration (LWFA) [1] requires excitation of a stable longitudinal plasma wave behind propagating laser pulse. The state-of-the-art in experimental and theoretical investigations of LWFA strongly suggests long distance and/or multi-stage acceleration scenarios for delivery of a reliable GeV source of electrons. One-to-one simulation of such LWFA requires to apply reduced models like slowly varying envelope approximation (SVEA) [2]. In particular the laser pulse is represented as a product of a fast term varying on laser wavelength scale and a slow component acting on longer plasma scale. $\vec{A}(t,\vec{r}) = (\vec{e}_x \pm i\vec{e}_y)\left[\hat{A}_\perp(t,z,\vec{r}_\perp)e^{-i(\omega_0 t - k_0 z)} + c.c.\right]$ where $A_\perp^*$ denotes complex conjugated amplitude. The laser pulse propagation can be then described by the following wave equation for a slowly varying complex amplitude $\hat{A}_\perp$

$$\left[2ik_0\left(\frac{\partial}{\partial z} + \frac{1}{c}\frac{\partial}{\partial t}\right) + \Delta_\perp - \frac{1}{c^2}\frac{\partial}{\partial t^2}\right]\hat{A}_\perp = \frac{4\pi}{c}\left\langle\frac{n}{\gamma}\right\rangle\hat{A}_\perp, \tag{1}$$

where $\Delta_\perp = \nabla_\perp^2$ denotes the transverse Laplace operator. We retain a higher order second time derivative term which is responsible for backward Raman scattering effect. The resulting equation can be classified as a nonlinear Schödinger equation perturbed with wave operator. The enhanced hyperbolicity of (1) makes it possible to eliminate a severe time step restriction known for explicit integration of parabolic equations. We proceed in a spirit of Method-of-Lines (MOL) semi-discretization and cast the wave equation in a system of first order ODEs as following

$$\frac{d\vec{A}_i}{dt} = \vec{V}_i \tag{2}$$

$$\frac{\partial \vec{V}_i}{\partial t} = 2i\frac{k_0}{k_p}\vec{V}_i - 2\frac{\vec{V}_{i+1} - \vec{V}_{i-1}}{2\Delta\xi} - \left\langle\frac{n_e}{\gamma}\right\rangle\Bigg|_i \vec{A}_i, \tag{3}$$

which can be integrated in time by any suitable time stepping routine, e.g. Runge-Kutta type methods. Thus the advantage of our approach is twofold. First, the explicit discretization is local and therefore the parallelization for multiple CPU computers is a rather straightforward task. Second, the semi-discretization in time makes a choice of time stepping very flexible and allows seamless connection with any plasma simulation code. To illustrate the last statement we apply the wave envelope solver together with our fluid-Maxwell code for simulation of a nonlinear regime of plasma wake field excitation in a cold plasma [3]. A snapshot of laser amplitude and corresponding plasma density perturbation at time step $t\omega_p = 31$, where ω_p is the laser frequency are presented in Figure 1. Unlike particle-in-cell method the fluid-Maxwell-Wave (FMW) code produces smooth distributions even with modest grid resolution 256 × 128. Thanks to the unified time stepping implementation fluid and particle-in-cell solvers can be used in hybrid fashion simultaneously. Our approach opens a new route to develop flexible and simple scalable codes with customized numerical methods. We also have implemented a built-in error control into our numerical codes which will allow to introduce adaptivity in a next code development round.

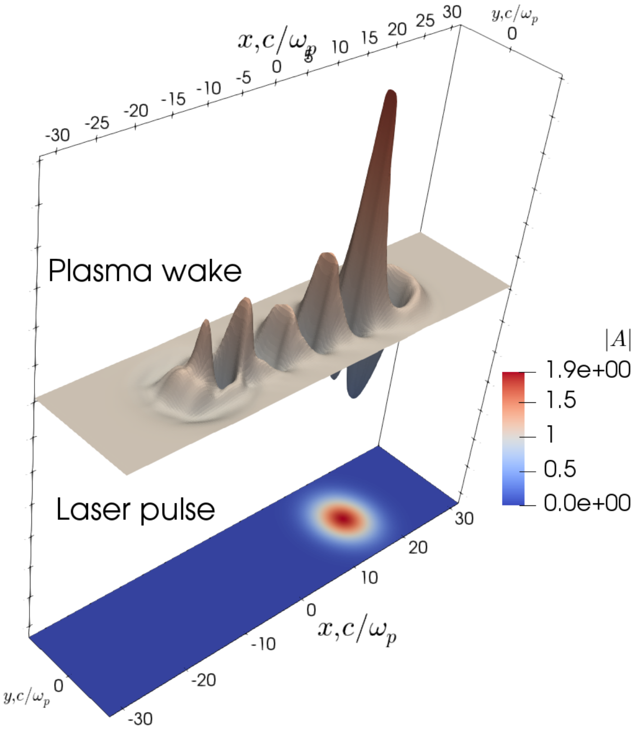

Figure 1: The plasma number density (upper) perturbed by laser pulse (lower) at $t\omega_p = 31$ for $a_0 = 2$ and $\omega_0/\omega_p = 100$, see [3]

References

[1] T. Tajima and J.M. Dawson, Phys. Rev. Lett., **43**, 267 (1979)

[2] P. Mora, *et al.*, Journal of Plasma Physics, **4**, 217-229 (1997)

[3] N. Elkina, V. Yu. Kharin, and S. G. Rykovanov, *in preparation* (2018)

Ponderomotive effects in multiphoton pair production [*]

C. Kohlfürst[†][1,2] *and R. Alkofer*[3]
[1]HI-Jena, Germany; [2]University of Jena, Germany; [3]NAWI Graz, University of Graz, Austria

Electron-positron pair production [1] in strong electric fields via multiphoton absorption has been already observed in laboratory. Due to fact, that upcoming laser facilities, e.g., ELI and XFEL operate at even higher intensities pair production holds as a promising effect capable of deepening our knowledge of vacuum nonlinearities and matter creation in general.

We have devoted a recent work [2] with focus on multiphoton pair production in the nonperturbative threshold regime to explore the particle dynamics in high-intensity laser fields. In this work, we have employed the DHW formalism, a relativistic phase-space approach. Hereby the electron is treated as a quantum field but the laser pulse is approximated by its mean-field. Given the magnitudes of the electric field needed in pair production this is a justified approximation.

In order to study pair production in the nonperturbative regime we employ an electric field of the form

$$\begin{aligned} E\left(z,t\right) &= \varepsilon m^2/e\, \mathcal{E}\left(z\right)\ F\left(t\right) \\ &= \varepsilon m^2/e\, \mathcal{E}\left(z\right)\ \cos^4\left(\frac{t}{\tau}\right)\ \cos\left(\omega t\right), \qquad (1) \end{aligned}$$

for $t \in [-\pi\tau/2,\ \pi\tau/2]$, and $E = 0$ otherwise. Nonperturbative multiphoton pair production is probed if one choses the product $\omega\tau > 1$ and a Keldysh parameter of $\gamma = \omega/m\varepsilon > 1$.

Due to the shape of the field any "classical" charged particle in an inhomogeneous oscillating electromagnetic field experiences ponderomotive forces. In short, due to the inhomogeneity of the field the particles drift away from strong field regions. The relativistic ponderomotive force then yields, see ref. [3],

$$\begin{aligned} F_p = -\Bigg(&\mathbf{v}_0 \cdot \boldsymbol{\nabla}_x m_*, \\ &\boldsymbol{\nabla}_x m_* + \frac{\gamma_0 - 1}{v_0^2}\left(\mathbf{v}_0 \cdot \boldsymbol{\nabla}_x m_*\right)\mathbf{v}_0 \Bigg), \qquad (2) \end{aligned}$$

where γ_0 is the Lorentz factor and $\mathbf{v}_0$ the particle's velocity.

Going beyond spatially quasi-homogeneous fields ($\lambda = 1000\ m^{-1}$) reveals that a decrease of the pulse's spot size leads to dramatic changes in the distribution function. In case of, e.g. $\lambda = 10\ m^{-1}$, the dominant peak in the particle momentum spectrum takes on a much wider form which can be related to quantum interferences.

At an even smaller focus size, $\lambda = 2.5\ m^{-1}$, we observe so-called peak splitting. Concentrating on the dominant peak, particles are created with close to vanishing momentum p_z and subsequently follow the oscillations of the background field. However, the force the field exerts on the particle depends on the particle's location in the field. As a result the particle obtains a net momentum per cycle of the field and therefore drifts to low-intensity regions in space. As the applied electric field is symmetric in z there are, however, two equally likely options: either the particles are accelerated in z or in $-z$ direction.

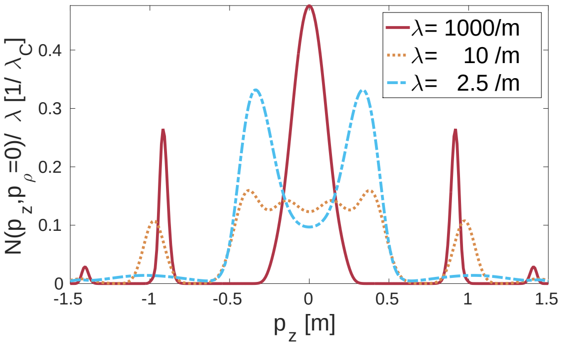

Figure 1: Reduced particle distribution function for a field of strength $e\varepsilon = 0.5\mathrm{m}^2$, length $\tau = 100\mathrm{m}^{-1}$, frequency $\omega = 0.7\mathrm{m}$ and various spatial extent λ. The peaks can be related to n-photon pair production.

We have demonstrated that the peaks split due to strong ponderomotive forces altering the particle momentum spectrum. Line broadening happens because the particle spectra properties which are characteristic for multiphoton pair production erode and instead of sharp lines one obtains broad bunches. In summary, we presented here further evidence how important it is to take spatial inhomogeneities of the fields underlying pair production processes into account.

References

[1] F. Sauter, Z. Phys. **69**, 742 (1931); W. Heisenberg and H. Euler, Z. Phys. **98**, 714 (1936); J. S. Schwinger, Phys. Rev. **82**, 664 (1951).

[2] C. Kohlfürst and R. Alkofer, Phys. Rev. D **97** (2018) no.3, 036026.

[3] D. Bauer, P. Mulser and W. H. Steeb, Phys. Rev. Lett. **75** (1995) 4622.

---

[*] Work supported by HI Jena in cooperation with Friedrich Schiller University Jena. Funded by the Helmholtz Association through the Impuls- und Vernetzungsfonds, Helmholtz Postdoc Programme (PD-316).

[†] C.Kohlfuerst@gsi.de

Nonabelian Higgs models: paving the way for asymptotic freedom

H. Gies[1,2] *and L. Zambelli*[2]
[1]Helmholtz Institute Jena, Germany; [2]Theoretisch-Physikalisches Institut, FSU Jena, Germany

Quantum electrodynamics (QED) is the world's best tested theory. Still, it cannot be extended to arbitrarily high energies or intensities as is indicated in perturbation theory by the occurrence of a Landau-pole singularity. This problem can be circumvented if QED is part of a larger unifying gauge group which is coupled to a suitable matter content such that the system becomes asymptotically free at high energies. We have demonstrated that new asymptotically free renormalization group (RG) trajectories can be constructed already in nonabelian Higgs models with the aid of generalized boundary conditions imposed on the renormalized action. We have constructed a family of explicit scaling solutions using a controlled weak-coupling expansion in the ultraviolet, and obtain a standard Wilsonian RG relevance classification of perturbations about scaling solutions. We obtain global information about the quasi-fixed function for the Higgs potential by means of analytic asymptotic expansions and numerical shooting methods. The long-range properties of these theories give rise to a conventional Higgs phase.

A fascinating aspect of quantum field theories is the fact that they can represent truly fundamental theories valid on all energy or length scales as a matter of principle (such as QCD, the theory of the strong interactions) – or predict their own failure such as QED. Embedding QED as a U(1) gauge theory into a non-abelian gauge group requires a suitable breaking mechanism, e.g., by a Higgs field. Rather generically, such non-abelian Higgs models also seem to be plagued by a similar Landau-pole problem as QED.

A mechanism that guarantees validity on all scales is asymptotic freedom, i.e., a controlled approach to the Gaußian fixed point towards higher energies. In this case, scalar fields are special as their full interaction potential has to approach asymptotic flatness. If so, large amplitude fluctuations can occur, the quantitative description of which requires technical control over the global form of the Higgs potential. This goes beyond conventional perturbative techniques – despite the fact that the system is weakly coupled.

Using effective-field-theory methods, large-N techniques, and more comprehensively functional RG methods, we have been able to identify new asymptotically free RG trajectories for nonabelian Higgs models that approach asymptotic flatness for the Higgs interaction potential [3, 4]. Figure 1 shows a series of such quasi-fixed-point potentials for decreasing gauge coupling g^2 approaching flatness asymptotically. As an interesting feature, the Higgs potential exhibits a nontrivial minimum at all scales that runs to infinity $\sim 1/g^2$. This invalidates the assumption of "asymptotic symmetry" and the use of the deep Euclidean region as is conventional in naive perturbation theory. Most importantly, the property of asymptotic flatness near the Planck scale is compatible with – if not even suggested by – the present data for the mass of the Higgs boson and the top quark as well as the strong gauge coupling.

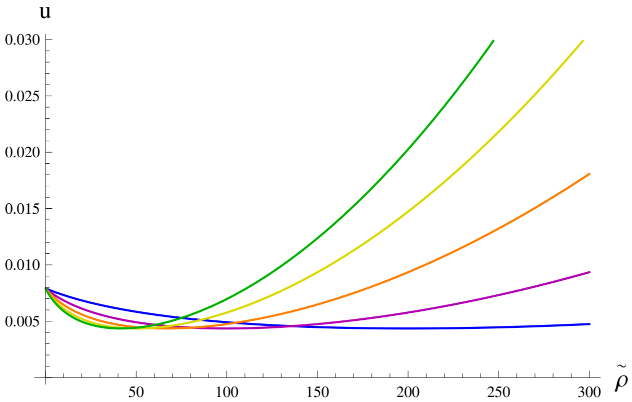

Figure 1: Effective renormalized Higgs potential for decreasing values of the gauge coupling g^2 from green to blue (larger to smaller) ($g^2 \in \{0.048, 0.04, 0.03, 0.02, 0.01\}$). The potential approaches asymptotic flatness with a minimum running to infinity.

In summary, our work demonstrates the construction of asymptotically free RG trajectories in nonabelian Higgs models. For a suitable embedding, this result has the potential to solve the decades old problem of a high-energy completion of QED. We emphasize that we have identified these trajectories also for those models, where low-order perturbation theory does not exhibit asymptotic freedom. Whereas most of our analysis is performed at weak coupling, the essential difference to standard perturbation theory arises from the fact that we carefully pay attention to the global properties of the Higgs interaction potential. Preliminary studies of the RG flow towards low energies exhibit compatibility with measured features of the standard model of particle physics.

References

[1] L. D. Landau, in *Niels Bohr and the Development of Physics*, ed. W. Pauli (Pergamon Press, London, 1955).

[2] M. Gockeler, et al., Phys. Rev. Lett. **80**, 4119 (1998).

[3] H. Gies and L. Zambelli, Phys. Rev. D **92**, 025016 (2015).

[4] H. Gies and L. Zambelli, Phys. Rev. D **96**, 025003 (2017).

An Addendum to the Heisenberg-Euler effective action beyond one loop

F. Karbstein[1,2] *and H. Gies*[1,2]

[1]Helmholtz-Institut Jena, Germany; [2]Theoretisch-Physikalisches Institut, FSU Jena, Germany

We study the effective interactions of external electromagnetic fields induced by fluctuations of virtual particles in the vacuum of quantum electrodynamics. Our main focus is on these interactions at two-loop order. We discuss in detail the emergence of the renowned Heisenberg-Euler effective action from the underlying microscopic theory of quantum electrodynamics (QED), emphasizing its distinction from a standard one-particle irreducible effective action. In our explicit calculations we limit ourselves to constant and slowly varying external fields, allowing us to adopt a locally constant field approximation. One of our main findings is that at two-loop order there is a finite one-particle reducible contribution to the Heisenberg-Euler effective action in constant fields, which was previously assumed to vanish. In addition to their conceptual significance, our results are relevant for high-precision probes of quantum vacuum nonlinearity in strong electromagnetic fields.

One of the striking predictions of quantum field theory is that virtual charged particle-antiparticle fluctuations in the quantum vacuum can induce nonlinear interactions among electromagnetic fields [1]. Aiming at probing the vacuum of the Standard Model of particle physics with classical electromagnetic fields and low energy photons, the dominant effective interactions are governed by quantum electrodynamics. For the macroscopic electromagnetic fields presently attainable in the laboratory, the effects of QED vacuum nonlinearities are rather small, making their experimental detection challenging. These effective interactions have no tree-level analogue, but are mediated by at least one electron-positron loop.

It is a fascinating aspect of this plethora of phenomena that they manifest the effective interactions of electromagnetic fields beyond Maxwell's linear theory, which can be summarized elegantly by an effective action that dates back to the early days of quantum field theory [1, 2]: the Heisenberg-Euler effective action. Its matured embedding into the modern language of field theory is due to Schwinger [3], who gave a nonperturbative definition of this action by means of the vacuum persistence amplitude, i.e., the Schwinger functional. Nowadays, QFT is often defined in terms of generating functionals for correlation functions, with the concept of the effective action being identified with the generating functions of one-particle irreducible (1PI) correlators (proper vertices).

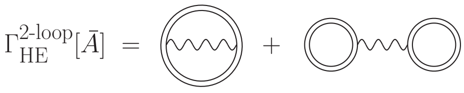

Figure 1: Diagrams constituting the two-loop Heisenberg-Euler effective action. The double line denotes the dressed fermion propagator accounting for arbitrarily many couplings to the external field $\bar{A}$.

In this work, we emphasize that the Heisenberg-Euler effective action is different from – though related to – the 1PI effective action. This fact has, of course, been well known in the specialized literature [4, 5] but is sometimes confused in textbooks. We detail the construction of the Heisenberg-Euler effective action from the standard definition of QED in terms of the partition function in the present work. The difference between the two effective actions is manifested by one-particle reducible (1PR) contributions to the Heisenberg-Euler action. In a perturbative loop expansion, such 1PR contributions occur at and beyond the two-loop order. At two-loop order, we find that there is a finite 1PR contribution to the Heisenberg-Euler effective action in constant electromagnetic fields, which was previously believed to vanish; cf. Fig. 1 (right).

As higher-loop diagrams are typically suppressed in comparison to the one-loop diagram, a proper inclusion of the previously neglected 1PR diagrams is expected to impact the proposed experimental signatures of quantum vacuum nonlinearities only at subleading order.

One of our main findings is that the coupling of two one-loop vacuum currents via a photon propagator gives rise to a nonvanishing 1PR contribution to the Heisenberg-Euler effective action at two loops even in the limit of constant electromagnetic fields; see also Ref. [7]. This contribution was previously believed to vanish. To clarify the importance of this newly evaluated 1PR contribution relatively to the well-known 1PI one, we have investigated the limits of perturbatively weak and strong fields. Whereas the 1PR contribution at two loops is generically suppressed for weak fields, it can even surpass its 1PI counter part in magnitude for strong fields.

References

[1] W. Heisenberg and H. Euler, Z. Phys. **98**, 714 (1936).

[2] V. Weisskopf, Kong. Dans. Vid. Selsk., Mat.-fys. Medd. **XIV**, 6 (1936).

[3] J. S. Schwinger, Phys. Rev. **82**, 664 (1951).

[4] V. I. Ritus, Sov. Phys. JETP **42**, 774 (1975) [Zh. Eksp. Teor. Fiz. **69**, 1517 (1975)].

[5] W. Dittrich and M. Reuter, Lect. Notes Phys. **220**, 1 (1985).

[6] H. Gies and F. Karbstein, JHEP **1703**, 108 (2017).

[7] F. Karbstein, JHEP **1710**, 075 (2017).

Photon polarization tensor in Hermite- and Laguerre-Gaussian beams

F. Karbstein[1,2] *and E. A. Mosman*[3,4]

[1]Helmholtz-Institut Jena, Germany; [2]Theoretisch-Physikalisches Institut, FSU Jena, Germany; [3]National Research Tomsk Polytechnic University, Russia; [4]Physics Faculty, Tomsk State University, Russia

We derive analytical expressions for the one-loop photon polarization tensor in linearly polarized pulsed Hermite- and Laguerre-Gaussian laser beams. Our findings will, e.g., be relevant for the study of vacuum birefringence experienced by probe photons brought into collision with a high-intensity laser pulse which can be represented as a superposition of either Hermite- or Laguerre-Gaussian modes.

The vacuum of quantum field theory is characterized by the omnipresence of fluctuations of the theory's particle degrees of freedom in virtual processes, describing their spontaneous creation and annihilation. In the language of Feynman diagrams, these processes correspond to diagrams without any external lines. As they do not couple to in- and outgoing real particles by definition, vacuum fluctuations are *per se* not observable. The situation, however, changes in the presence of an external electromagnetic field. Due to the fact that electromagnetic fields couple to charges, vacuum fluctuations of charged particles generically give rise to effective self-couplings of the prescribed electromagnetic field [1].

A central object in the study of such effects is the photon polarization tensor (see Fig. 1), which encodes information about non-trivial modifications of the dispersion relation for probe photons propagating in the electromagnetized QED vacuum, and is the fundamental quantity in the theoretical analysis of vacuum birefringence [2]. The one-loop photon polarization tensor is known analytically for both homogeneous electromagnetic fields [3], and generic plane wave backgrounds [4]. Besides, analytical results for low-energy photons in slowly varying inhomogeneous electromagnetic fields were obtained in Ref. [5]. The latter results are based on a locally constant field approximation (LCFA) of the one-loop Heisenberg-Euler effective Lagrangian[1]. Hence, by construction they are limited to slowly varying electromagnetic fields, varying on spatial and temporal scales significantly larger than the Compton wavelength/time of the electron, a criterion which is fulfilled by all laser beams currently available in the laboratory.

In Ref. [7], we use the LCFA to obtain analytical insights into the photon polarization tensor for low-energy probe photons in linearly polarized, pulsed Hermite- and Laguerre-Gaussian laser beams of optical frequencies and arbitrary mode composition. As any paraxial beam can be expanded into either Laguerre- or Hermite-Gaussian modes, our results will allow for an analytical study of signatures of vacuum nonlinearities in experimentally realistic field configurations provided by high-intensity lasers in unprecedented detail. While a decomposition into Laguerre-Gaussian modes is particularly adequate for beam profiles exhibiting a circular symmetry about the beam's propagation direction, a decomposition into Hermite-Gaussian modes is suited for beams with Cartesian symmetry.

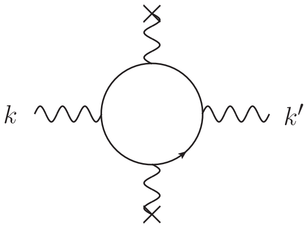

Figure 1: Representative Feynman diagram for the photon polarization tensor featuring two couplings to the external field, depicted by wiggly lines ending at crosses. As inhomogeneous fields can transfer energy and momentum to the fermion loop, the outgoing photon momentum k' generically differs from the incident one k.

As an immediate application, our results will facilitate the study of vacuum birefringence and photon diffraction effects in high-intensity laser beams prepared in a distinct higher Laguerre- or Hermite-Gaussian mode. So far, theoretical studies of these effects typically assumed the high-intensity laser beams to be prepared in the fundamental Gaussian mode. The spatially inhomogeneous transverse intensity patterns of higher modes in the beam focus might potentially be employed to induce interference patterns in the signal photon distribution in the far field, as already theoretically analyzed and proposed as signature of vacuum nonlinearity in multi-beam configurations; cf., e.g., Ref. [6].

References

[1] W. Heisenberg and H. Euler, Z. Phys. **98**, 714 (1936).

[2] J. S. Toll, Ph.D. thesis, Princeton Univ., 1952 (unpublished).

[3] I. A. Batalin and A. E. Shabad, Zh. Eksp. Teor. Fiz. **60**, 894 (1971) [Sov. Phys. JETP **33**, 483 (1971)].

[4] V. N. Baier, A. I. Milshtein and V. M. Strakhovenko, Zh. Eksp. Teor. Fiz. **69**, 1893 (1975) [Sov. Phys. JETP **42**, 961 (1976)]; W. Becker and H. Mitter, J. Phys. A: Math. Gen. **8** 1638 (1975).

[5] F. Karbstein and R. Shaisultanov, Phys. Rev. D **91**, 085027 (2015).

[6] B. King, A. Di Piazza and C. H. Keitel, Nature Photon. **4**, 92 (2010).

[7] F. Karbstein and E. A. Mosman, Phys. Rev. D **96**, 116004 (2017).

Attosecond streaking with twisted X waves and intense NIR pulses

B. Böning[1], W. Paufler[1], and S. Fritzsche[1,2]

[1]Theoretisch-Physikalisches Institut, University of Jena, Germany; [2]Helmholtz-Institut, Jena, Germany

In recent years, the dynamics of electrons on ultrashort timescales have become experimentally accessible due to the ability to generate and precisely control laser pulses of sub-femtosecond duration. A widely used experimental tool is the attosecond streaking technique that is based on the photoionization of atoms by single attosecond XUV laser pulses in the presence of a moderately strong near-infrared (NIR) pulse [1]. In the ionization process, the temporal structure of the XUV pulse as well as the bound-state wavefunction are imprinted on the photoelectron wavepacket. The NIR pulse subsequently accelerates the photoelectron in the continuum. This second step is called streaking. Variation of the time delay τ between the ionizing XUV and the NIR pulse then allows to extract temporal information about the photoelectron wavepacket. The resulting streaking spectra display the ionization probability as function of time delay and photoelectron energy. They contain temporal information about the initial bound state and the ionizing pulse.

Besides manipulating the temporal shape of the ionizing pulse, its spatial wave form can be tailored. Twisted Bessel beams, for example, have a helical phase structure due to a non-zero orbital angular momentum (OAM). This property offers novel ways of manipulating light-matter interactions, including modified selection rules in the photoionization of atoms [2]. Twisted pulses of finite duration can theoretically be described by X waves, which are superpositions of Bessel beams.

We theoretically investigated how the spatial structure of the ionizing X wave modifies the attosecond streaking process [3]. The ionization by the high-energetic XUV pulse can be treated using first-order perturbation theory. For the subsequent streaking, we need to take the rather high intensity of the NIR pulse into account in the continuum states available to the photoelectron. This was done in the framework of the strong-field approximation.

The details of the streaking spectra are expected to depend on the properties of the X wave (central frequency ω_{XUV}, helicity Λ_{XUV}, opening angle θ_k, projection of total angular momentum m) and the properties of the NIR pulse (wavelength λ_{NIR}, intensity I_{NIR}, polarization), the impact parameter **b** as well as the size of the target. However, for single-atomic targets, we found that the characteristic features of the spectra can be controlled by the opening angle of the X wave and the impact parameter of the atom. We observed that the OAM of the X wave only has a minor influence on the spectra. Fig. 1 shows an example of a streaking spectrum computed for the single-atomic case. The spectrum shows two streaking traces, which result from the split of the X wave into two pulses separated in time at the chosen impact parameter. The temporal separation of these two pulses is half a cycle length (T_{NIR}=2.6 fs) of the NIR pulse. This yields interferences in the spectrum at τ = 0 fs, 1.3 fs and 2.6 fs. When the localized target is replaced by an inifinitely extended atomic target, our computations show that the streaking spectra no longer depend on the opening angle nor the OAM of the X wave.

Recent advances in the generation of twisted pulses promise a variety of experimental applications in the strong-field and ultrafast regime [4]. Two-color experiments like the attosecond streaking presented above might provide insights into the dynamics of excited states that are not accessible via the interaction with plane-wave pulses due to different selection rules. In this regard, an important future task is to investigate the influence of finite target sizes on the interaction with ultrashort pulses.

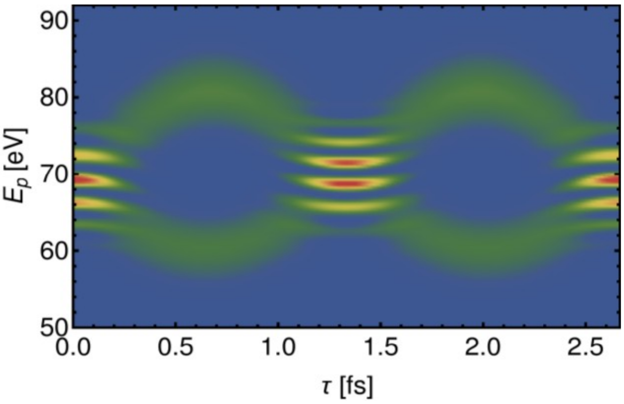

Figure 1: Streaking spectrum resulting from the ionization by a twisted X wave pulse in the presence of a lin. polarized NIR pulse. Atomic parameters: b=600 nm, 1s initial state, binding energy E_B=11.7 eV; NIR parameters: λ_{NIR}=800nm, I_{NIR}=3.5x10^{12} W/cm^2; X wave parameters: ω_{XUV}=81.6 eV, Λ_{XUV}=1, θ_k=20°, m=4.

References

[1] J. Itatani et al., Phys. Rev. Lett. **88**, 173903 (2002)

[2] M. Scholz-Marggraf et al., Phys. Rev. A **90**, 013425 (2014)

[3] B. Böning, W. Paufler and S. Fritzsche, Phys. Rev. A. **96,** 043423 (2017)

[4] G. Gariepy et al., Phys. Rev. Lett. **113**, 153901 (2014)

Grants: DFG Priority Program 1840, “QUTIF” under Contract FR 1251/17-1

Strong-field ionization with Bessel pulses

W. Paufler[1], *B. Böning*[1], *S. Fritzsche*[1,2]

[1]TPI, Jena, Germany; [2]HI, Jena, Germany

During recent years, the interaction of intense pulses with matter became an attractive field of research. At intensities of about 10^{14} W/cm^2, light matter interactions are dominated by non-perturbatve procresses such as tunneling or multiphoton ionization. Strong-field ionization can be described by a semiclassical two-step model [1]. If an atom or molecule is exposed to a strong laser field, the atomic potential is suppressed by the external field. The suppression of the atomic potential forms a barrier, through which an electron can tunnel (Step I). In the second step, the liberated electron is considered as a free particle in the external laser field. We solve the classical equations of motion for an electron, which is driven by the external field and the potential of the parent ion in order to explore the asymptotic momentum of the released electron. The structure of the obtained photoelectron momentum distributions (PEMD) is affected by the interacting field as well as by the ground state of the particle. The PEMD can therefore be used to probe the chiraly of molecules.

We theoretically investigated the strong-field ionization of hydrogen by Bessel pulses [2]. We calculated the PEMD and analyzed especially the emission of electrons perpendicular to the beam axis as well as in the direction of the beam axis. In addition we studied how different impact parameters of localized atoms modify the PEMD. Since Bessel pulses can be considered as infinitely superpositions of circularly polarized plane waves with the same helicities, whose wavevectors lie on a cone, we compared the PEMD from Bessel pulses with those of a strong circularly polarized plane wave pulses.

For single atom simulations we found that the PEMD projected on the plane perpendicular to the beam axis are indistiguishable from those of circularly polarized plane waves. The propagated distance of the released electron is to small to be affected by the spatial structure of the Bessel pulse. Therefore the electron is locally exposed to a circularly polarized plane wave.

If an atom is ionized by a strong circularly polarized pulse, most of the electrons are emitted and accelerated in the polarization plane which is perpendicular to the propagation direction. In contrast to plane waves, the electric field Bessel pulse can be nonzero in propagation direction. Thus the released electrons can have a much higher momentum in direction of the beam axis, which is equivalent to the propagation direction for a plane wave (z-direction). Fig 1 shows an example for a PEMD projected on two different planes (x-z and y-z).

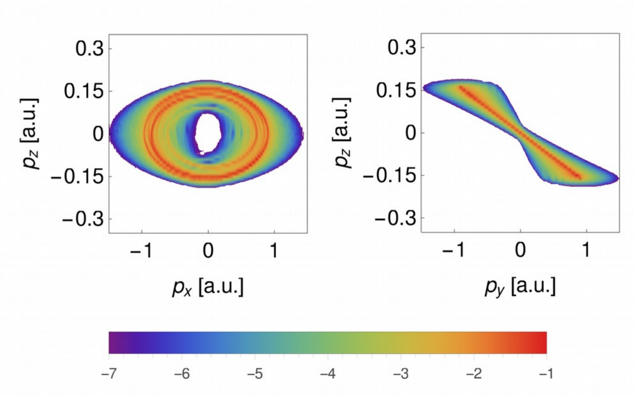

Figure 1: The momentum distributions of photoelectrons released by a 10 cycle Bessel pulse with wavelength λ=800 nm, projection of the TAM $m_\gamma=2$, helicity $\Lambda=1$ and opening angle $\theta_k=25°$.

The shape of the momentum distributions can be explained with the conservation of canonical momentum of the electron after its release.

The localized single atomic target can be replaced by a cloud of atoms. If the size of the target down not exceed the size of the wavelength of the interacting field, it is still possible to resolve the shape of the PEMD as shown in Fig. 1.

Recent studies have shown the generation of linearly polarized XUV radiation with controlled TAM projection [3], which result from High Harmonic Generation of twisted light. The knowledge about the PEMD in Bessel pulses can be used to tailor these pulses and use them as a source of circularly polarized harmonics with well defined TAM.

References

[1] N. I. Shvetsov-Shilovski, et al., “Semiclassical two step model for strong field ionization”, Phys. Rev. A 94, 013415 (2016)

[2] W. Paufler, B. Böning, S. Fritzsche, submitted to Phys Rev A, (2018)

[3] C. Hernandez-Garcia, et al., “Attosecond extreme Ultraviolet Vortices from High-Order Harmonic Generation”, Phys. Rev. Lett. 111, 083602 (2013)

Grants: DFG Priority Program 1840, “QUTIF” under the contract FR 1251/17-1

Rayleigh scattering of twisted Bessel beam by hydrogenlike ions*

A. A. Peshkov[1]*, A. V. Volotka*[1]*, A. Surzhykov*[2,3]*, and S. Fritzsche*[1,4]

[1]Helmholtz-Institut Jena, Germany; [2]Physikalisch-Technische Bundesanstalt, Braunschweig, Germany; [3]Technische Universität Braunschweig, Germany; [4]Friedrich-Schiller-Universität Jena, Germany

The elastic scattering of photons at the bound electrons of atoms or ions, commonly known as Rayleigh scattering, has been intensively explored over the past decades. From a theoretical viewpoint, the Rayleigh scattering has attracted much interest as one of the simplest second-order quantum electrodynamical (QED) process. In the past, a large number of experimental and theoretical studies have been performed in order to understand how the electronic structure of atoms affects the polarization of the Rayleigh-scattered photons. In particular, the linear polarization of the elastically scattered light has been measured directly by Blumenhagen et al. at the PETRA III synchrotron at DESY [1]. This experiment was performed for a gold target with a highly linearly polarized incident plane-wave radiation. Until the present, however, very little has been known about the Rayleigh scattering of twisted (or vortex) light beams. When compared to plane-wave radiation, such twisted photons have a helical wave front and carry a well-defined projection of the orbital angular momentum upon their propagation direction. In addition, the transverse intensity profile of the twisted beams exhibits a ringlike pattern with a dark spot (vortex) at the center. In experiments, twisted (Bessel) beams can nowadays be readily produced by means of spatial light modulators or axicons.

In the present work, we analyze theoretically the behavior of the polarization Stokes parameters of scattered photons for the elastic scattering of twisted Bessel light. Here we restrict ourselves to the nonresonant Rayleigh scattering of light by hydrogenlike ions in their ground state, and especially by hydrogenlike carbon. We consider and derive the Stokes parameters within the framework of second-order perturbation theory and the density-matrix approach. Three different possible experimental scenarios are considered here for the scattering of the incident Bessel beam at a single atom, a mesoscopic (atoms in a trap), or a macroscopic (foil) atomic target, and which are all assumed to be centered on the beam axis. We show that the linear and circular polarization of scattered light depends generally on the helicity and the opening angle of Bessel beams, leading to Stokes parameters that differ quite significantly from the scattering of incident plane-wave photons. Moreover, results of our calculations indicate that the polarization of the scattered photons is very sensitive to the projection of the total angular momentum (TAM) of twisted light for single atoms and mesoscopic atomic targets of a few tens of nm in size, while it remains unaffected by the TAM in the case of a larger macroscopic target. In particular, Figure 1 illustrates the first Stokes parameter, which characterizes the degree of linear polarization of outgoing photons, as a function of the emission angle. As seen from this figure, the outgoing photons are completely linearly polarized at the scattering angle 90 degrees for incoming plane waves. However, the scattering of a Bessel beam by mesoscopic target with width 10 nm, for example, leads to a significant decrease of the polarization at this angle, depending on the TAM projection of twisted light.

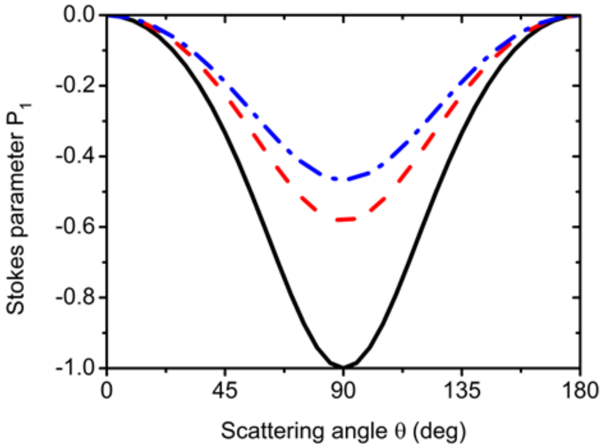

Figure 1: Stokes parameter of Rayleigh scattered light on hydrogenlike carbon ions in their ground state as a function of the emission angle. Results for incident plane waves (black solid lines) are compared with those for Bessel beams with TAM +1 (red dashed lines) and -1 (blue dash-dotted lines), respectively. Relativistic calculations were performed for mesoscopic atomic target of size 10 nm. Results are shown for the helicity +1, opening angle 30 degrees, and photon energy 100 eV of a Bessel beam.

Although our study was restricted to the scattering by hydrogenlike ions in their ground 1s state, similar polarization properties can also be observed in the scattering of twisted light by electrons in other s shells. In view of this, Rayleigh scattering may serve as an accurate technique for measuring the properties of twisted beams in a wide range of photon energies, and in particular at rather high energies.

References

[1] K.-H. Blumenhagen S. Fritzsche, T. Gassner, A. Gumberidze, R. Märtin, N. Schell, D. Seipt, U. Spillmann, A. Surzhykov, S. Trotsenko, G. Weber, V. A. Yerokhin, and T. Stöhlker, New J. Phys. 18 (2016) 103034.

[2] A. A. Peshkov A. V. Volotka, A. Surzhykov, and S. Fritzsche, Phys. Rev. A 97 (2018) 023802.

*Also part of the GSI Scientific Report 2017 / GSI Report 2018-1.

Controlling quantum random walk with step dependent coins

S. Panahiyan[1] *and S. Fritzsche*[1,2]

[1]Helmholtz-Institut Jena, Fröbelstieg 3, D-07743 Jena, Germany

[2]Theoretisch-Physikalisches Institut, Friedrich-Schiller-University Jena, D-07743 Jena, Germany

Quantum random walk is an advanced tool for simulating and programming other quantum systems such as neutral atoms, highly charged ions and photons [1]. It is also used for implementing quantum algorithms [2].

In order to use quantum random walk for simulation, controllability over walker's behaviour is required. This is for obtaining desired probability density distribution for the walker. To achieve this, we have considered step dependency as a characteristic property for the coin operator used for performing the walk.

Quantum random walk with a step-dependent coin

Quantum random walk (QRW) is counterpart of classical random walk [2]. The walker is realized as a quantum system and both, the coin and the movement (shift) of the walker are represented by two operators that are applied to the walker iteratively: While the shift operator moves the walker simply to the left or right on a mesh, the (so-called) coin operator just acts on the internal degrees of freedom of the walker. Many features of QRW arise from the interplay of the coin and walker, i.e. from the walker's internal degrees of freedom. Due to this interplay, QRW may exhibit a much richer behaviour of its probability distribution than classical random walk. This freedom in choosing the coin and state of the walker can be employed also to find novel probability density distributions for the walker after a given number of steps which is one of central motivations of this investigation. We here consider a step-dependent coin to perform the Walk.

Walk setup and results

The walker is a quantum system (photons, ions and neutral atoms) walking on a linear mesh. The walker lives in a Hilbert space of the $H = H_C \otimes H_P$, in which H_C is the coin space depicting internal degrees of freedom of walker. It is spanned by $\{|0\rangle_C, |1\rangle_C\}$. H_P is the position space spanned by $\{|\mathrm{i}\rangle_\mathrm{P} : \mathrm{i} \in \mathbb{Z}\}$. The overall operator of the (quantum) walk consists out of two parts: i) the coin operator that just acts upon the internal degrees of freedom and ii) the shift operator that moves the walker along the mesh, in dependence on the internal state of the walker. Here, we consider the (standard) conditional shift operator

$$\hat{S} = |0\rangle_C\langle 0| \otimes \sum |i+1\rangle_P\langle i| + |1\rangle_C\langle 1| \otimes \sum |i-1\rangle_P\langle i| \qquad (1)$$

and the step-dependent coin of our proposal is given by

$$\begin{aligned} \hat{C} = {} & cos\,T\theta\, |0\rangle_C\langle 0| + sin\,T\theta\, |0\rangle_C\langle 1| \\ & + sin\,T\theta\, |1\rangle_C\langle 0| - cos\,T\theta\, |1\rangle_C\langle 1| \end{aligned} \qquad (2)$$

in which T refers to the number of step and where the rotation angle θ is characteristic for the given walk. Such a step-dependent coin can be realized, for example, with photons if their polarization are rotated by the (step-dependent) angle $T\theta$ [3]. Such a step-dependent 'rotation' can be achieved also with trapped ions if proper (resonant) radio-frequency pulses are applied to the internal state of the ions [4]. The quantum random walk is done by applying successively the evolution operator, $\hat{S}\hat{C} = \hat{U}$ upon the initial state $|\phi\rangle_{fin} = \hat{U}^T |\phi\rangle_{ini}$. The initial state could be $|\phi\rangle_{initial} = |0\rangle_C \otimes |0\rangle_P$. It is worthwhile to mention that such initial state could be generalized to superposition for the walker. Simulation of the walk shows that this QRW enjoys diverse probability density distribution depending on choices for θ. Different classes of distributions are summarized in table I and plotted for $T = 30$ in Fig.1.

Classes	θ
Localized: free	0
Localized: bounded	$\pi/2$
Localized: bounded with periodic splitting	$\pi/4$
Compact classical like	$\pi/12$
Classical like	$1.524\pi/12$
Semi-classical/quantum like	$\pi/5$
Quantum like	$\pi/3$

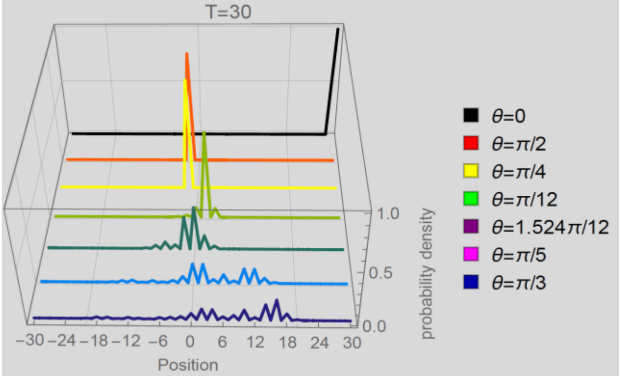

Table I and Fig1: Classification of observed probability density distribution for walk with step-dependent coin.

The existence of diverse probability density distribution confirms the possibility of the controlling walker's behaviour on high level for this walk. This enables one to employ this walk for simulating other quantum systems and provide the systems in desired states that are not easily feasible. Due to these different classes of the probability density distribution, one can develop a more adaptable quantum walk-based search algorithm [2].

References

[1] M. Mohseni et al, J. Chem. Phys. 129 (2008) 174106.
[2] N. Shenvi et al, Phys. Rev. A 67 (2003) 052307.
[3] A. Schreiber et al, Phys. Rev. Lett. 104 (2010) 050502.
[4] H. Schmitz et al, Phys. Rev. Lett. 103 (2009) 090504.

Atomic computations of hyperfine coupling constants *

R. Beerwerth[1,2] *and S. Fritzsche*[1,2]

[1]Helmholtz Institute Jena, Germany; [2]Theoretisch-Physikalisches Institut, Friedrich Schiller University Jena, Germany

Precise spectroscopic measurements of hyperfine structures and isotope shifts allow to extract information about the nucleus under investigation, such as mean squared charge radii, deformation, nuclear spin and nuclear moments [1]. With the help of isotope separator online facilities that allow the production of atomic beams for large chains of isotopes one can probe these quantities for many short-lived nuclei. Recent advances [2] now open the perspective to extend these studies also into the region of superheavy elements, such as nobelium and in the near future lawrencium in order to probe possible regions of increased stability.

The hyperfine coupling constants A and B relate the nuclear magnetic dipole μ and electric quadrupole moments Q to the magnetic field and electric field gradients generated by the electrons at the site of the nucleus, respectively. Both of these quantities can be determined experimentally by measuring the same transition in different isotopes, if the nuclear moments are known for one of these isotopes. Alternatively, both hyperfine coupling constants can be computed from atomic many-body theory such as the multi-configuration Dirac-Fock (MCDF) method [3]. For iron, the only stable odd mass isotope ^{57}Fe with nuclear spin ½ does not have a quadrupole interaction, and consequently no quadrupole moment was known so far. In order to extract the nuclear quadrupole moment of ^{53}Fe, we performed extensive MCDF calculations of the hyperfine constants for the $3d^6 4s^2\ {}^5D_4$ ground level and the $4s4p\ {}^5F_5$ excited level [4]. Since the nuclear dipole moment and its coupling constants are well known, the A values for both levels were used as a benchmark to test the computations. Our result for B was subsequently used to extract Q .

Several independent model calculations were performed to provide an estimate of the theoretical uncertainty. Each model computation was performed in a systematically enlarged configuration space, which was generated by virtual single and double excitations of the valence electrons. Especially the magnetic dipole interaction of the ground level was strongly influenced by core effects. To account for these effects, single excitations from the core orbitals had to be incorporated into the generation of the atomic basis and lead to an agreement between experiment and theory at the 10% level.

Our computed results are shown in Fig. 1, where every circle marks the result of one model calculation of the hyperfine coupling constants for the ground or excited level. The results clearly show that the A-factor for the ground level deviates significantly from experiment when no core effects are considered. This effect does not happen for the excited level, since here the main contribution to the hyperfine interaction comes from the uncoupled *s*-electron and hence core effects are much less significant. The *B*-factors for both levels scatter much less, which, together with the good agreement of the *A*-factors with the experimental values, leads to the conclusion that an uncertainty of 15%, shown as coloured bar, for the computed values seems reasonable. The black lines denote the experimentally determined coupling constants with additional input from nuclear theory, whose error bars are not shown here.

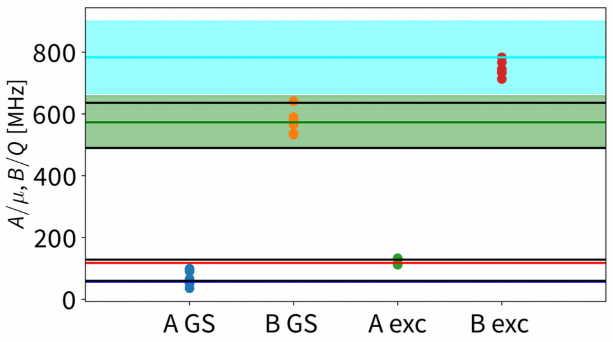

Figure 1: Computed hyperfine coupling constants A and B for the $^5D_4$ ground (GS) and $^5F_5$ excited Level of neutral ^{53}Fe from different model computations (circles). The black lines denote experimental values, the coloured lines the adopted values from our computations and the coloured bars the computational uncertainty.

In summary, atomic computations can provide valuable input in interpreting experimental data and in this case helped to extract nuclear properties. The combination of independent model calculations and systematically enlarged configuration spaces can provide estimates of theoretical uncertainties.

References

[1] M. Block, Hyperfine Interact. 238 (2017), 40
[2] M. Laatiaoui et al., Nature 538 (2016), 495-498
[3] P. Jönsson et al., Comput. Phys. Commun. 177 (2007), 597622
[4] A. J. Miller et al., Phys. Rev. C 96 (2017), 054314

---

* Also part of the GSI Scientific Report 2017 / GSI Report 2018-1

Auger cascade calculations in krypton supporting pump–probe experiments[*]

S. O. Stock[1,2], *R. Beerwerth*[1,2], *and S. Fritzsche*[1,2]

[1]Helmholtz Institute Jena, Germany; [2]Theoretisch-Physikalisches Institut, Friedrich Schiller University Jena, Germany

Recent advances in experimental techniques such as ultrafast time-resolved spectroscopy and modern UV and X-ray sources have enabled detailed studies of ionization processes. In order to interpret the results of these experiments, large-scale atomic structure computations are an important tool. Here, we report our theoretical results in support of a recent experimental study of the ionization dynamics in inner-shell excited krypton [1].

The experiment employs a pump–probe scheme and for the first time combines absorption spectroscopy and photoion spectroscopy to give a detailed picture of the ionization dynamics. The pump pulse, an attosecond XUV beam centered around 90 eV, excites the $3d^{-1}np$ resonances in neutral krypton while an intense few-cycle near-infrared (NIR) pulse acts as probe by (doubly) ionizing different groups of Kr^{+} ions to Kr^{3+}. Through variation of the NIR intensity, different groups of levels can be “reached” by the probe pulse which allows a detailed view into the ionization dynamics (see Ref. [1] for details). By varying the delay between XUV and NIR pulse, one gains access to the lifetimes of the levels which are ionized by the NIR pulse.

In order to support the experiment, we performed extensive multiconfiguration Dirac–Fock calculations using the GRASP [2] and RATIP [3] packages. After excitation by the XUV pulse, the $3d^{-1}np$ excited atoms decay predominantly by a two-step Auger cascade. We model this decay cascade by considering all possible normal Auger decays as well as shake processes of the *np* valence electron, in an approach similar to our recent theoretical studies [4,5]. All calculations are performed at a fine-structure level in order to obtain a comprehensive view of the autoionization paths.

An overview of the Auger cascade following the resonant $3d^{-1}np$ excitation is given in Fig. 1. In the first step of the cascade, the inner-shell excited krypton atoms decay predominantly via spectator Auger decays to the $4p^{-2}np$, $4s^{-1}4p^{-1}np$, $4p^{-3}4dnp$, and $4s^{-2}np$ levels, while participator processes can be neglected. In the second step of the cascade, the $4s^{-1}4p^{-1}np/4p^{-3}4dnp$ levels autoionize further to the ground configuration of Kr^{2+} while the $4s^{-2}np$ levels autoionize to the Kr^{2+} $4s^{-1}4p^{-1}$ and $4p^{-3}4d$ configurations.

Even though only a few of the autoionizing Kr^{+} levels (marked with the numbers 1–12 in Fig. 1) are predominantly populated during the first step of the cascade, their lifetimes range from a few femtoseconds to several hundred femtoseconds. Since the experiment cannot access the decay curves of individual levels, but instead rather large groups of levels within an energy range, we calculate *effective* lifetimes, as a weighted average of the individual lifetimes, for different level groups. While the $4s^{-2}np$ levels have an effective lifetime of only 6 fs, the $4s^{-1}4p^{-1}np/4p^{-3}4dnp$ levels decay considerably slower, with an effective lifetime of 49 fs. This difference in effective lifetimes is consistent with the experimental findings where a higher NIR intensity leads to a longer apparent lifetime, since lower-lying levels are being addressed by the probe pulse.

In conclusion, comprehensive theoretical studies of Auger cascades are important to support new kinds of experiments with modern UV and X-ray sources.

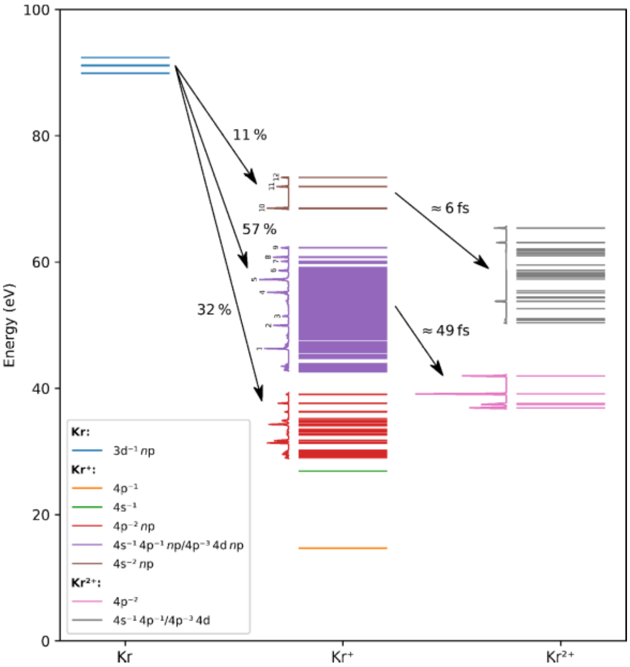

Figure 1: Diagram of the levels involved in the two-step Auger cascade after resonant $3d^{-1}np$ excitation of Kr. The spectra to the left of each group of levels show the relative population of the respective levels. Energies are given relative to the ground level of neutral krypton. The $4s^{-1}4p^{-1}np$ and $4p^{-3}4dnp$ configurations of Kr^{+} as well as the $4s^{-1}4p^{-1}$ and $4p^{-3}4d$ configurations of Kr^{2+} are mixing heavily and are therefore not clearly distinguishable.

References

[1] K. Hütten et al., Nat. Commun. 9 (2018), 719

[2] P. Jönsson et al., Comput. Phys. Commun. 177 (2007), 597–622

[3] S. Fritzsche, Comput. Phys. Commun. 183 (2012), 1525–1559

[4] S. Schippers et al., Phys. Rev. A 94 (2016), 41401

[5] S. Stock, R. Beerwerth, and S. Fritzsche, Phys. Rev. A 95 (2017), 53407

---

[*] Also part of the GSI Scientific Report 2017/GSI Report 2018-1

QED sensitive lifetimes in B-like, F-like, Al-like and Cl-like ions

M. Bilal[1,2], *A. V. Volotka*[2], *R. Beerwerth*[1,2], *S. Fritzsche*[1,2]

[1]TPI, Jena, Germany; [2]HI, Jena, Germany

Transition energies and transition rates are two fundamental properties of atomic states. Therefore, a detailed analysis and comparison of theoretical predictions with experimental observations may provide crucial insight into our basic understanding of the atomic structure. For level energies, there exists a number of cases where very high accuracy has been achieved from both theory and experiment, and helped to make quantum electrodynamic (QED) and many-body relativistic effects visible. For the transition rates and line strengths, in contrast, the accuracy level is often not yet sufficient to test QED and many body relativistic effects. This is partially due to theory and partially due to experiment. We know that transition rates depend on higher power of transition energy and non-diagonal matrix elements of the multipolar electromagnetic operators. In contrast to transition energies, there is no variational principle available that defines a minimum condition for the optimization of non-diagonal matrix elements.

In the case of an M1 transition between the fine-structure levels of the same configuration the non-diagonal matrix element i.e., the line strength, is less sensitive than for E1 allowed transitions. This is because in the nonrelativistic limit, the M1 line strength is insensitive to the description of the many-electron wave functions. In other words, (almost) all correlation corrections are of relativistic origin and, therefore, suppressed by a factor αZ (Z is the nuclear charge). For such transitions the line strengths are especially sensitive to the QED contributions. For instance, the leading QED effect of an order α, so called electron anomalous magnetic moment (EAMM) correction, contributes to 0.46%. Therefore, such M1 transition rates can be calculated very precisely and may be used as a benchmark for comparison with the experiment.

We have calculated the line strengths of QED-sensitive forbidden transitions by utilizing the multiconfiguration Dirac-Hartree-Fock and relativistic configuration interaction methods. We have extended the high precision evaluations previously performed for the middle Z B-like ions to higher Z as well as to different systems such as F-, Al-, and Cl-like ions. In our systematically enlarged wave functions, we incorporated all important electron correlations and the effects of relativity by taking the Coulomb and Breit interactions into account. The wave functions are systematically improved by performing MCDHF calculations for each new layer of correlation orbitals and keeping the previous calculated orbitals fixed. For each new layer of correlation orbitals the basis of CSFs is expanded by including further single (S) and double (D) virtual excitations from the configurations defining the multi reference set to the active set of orbitals. The active set of orbitals is spanned by the orbitals with a principal quantum number $n \leq 7$ and with azimuthal quantum number $l \leq 6$. The obtained line strengths are further improved by rigorous calculations of the QED correction within an extended Furry picture approach. We used up-to-date accurate transition energies for the calculations of the M1 transition rates and reported lifetimes in the millisecond to picoseconds range .

Table 1: Lifetimes (in seconds) calculated for the $2s^2 2p^5\ ^2P_{1/2}$ level in F-like ions and the $3s^2 3p^5\ ^2P_{1/2}$ level in Cl-like ions compared with experimental lifetimes. A_{M1} is the present transition rate in (s^{-1}) from the M1 channel and A_{E2} is the transition rate in (s^{-1}) from the E2 channel.

Ions	A_{M1}	A_{E2}	τ_{pres}	τ_{exp}
F-like				
Ar^{9+}	1.0639(04)[+02]	2.11[-03]	9.3994(33)[-03]	9.32(12)[-03][1]
Fe^{17+}	1.9428(10)[+04]	1.94[+00]	5.1466(26)[-05]	
Mo^{33+}	1.2432(12)[+07]	9.77[+03]	8.0372(79)[-08]	
W^{65+}	2.4097(57)[+10]	2.16[+08]	4.1131(98)[-11]	
Cl-like				
Fe^{9+}	6.9615(93)[+01]	1.52[-02]	1.4362(19)[-02]	1.42(2)[-02][2] 1.441(14)[-02][3] 1.364(25)[-02][4]
Mo^{25+}	1.1746(13)[+05]	2.41[+02]	8.4959(96)[-06]	
W^{57+}	3.8190(94)[+08]	1.05[+07]	2.5485(65)[-09]	

For the sake of brevity, we present result only for F-like and Cl-like ions. As seen from the Table 1, the comparison of our predicted lifetime for F-like Ar with the experiment at the LLNL-EBIT [1] and for the lifetime of Cl-like Fe with the experiment at the HD-EBIT [2] show a very good agreement. These experiments with an uncertainty larger than 0.5% are however not sensitive enough to test the underlying relativistic correlations and the leading QED effects. New experiments with the soft x-ray free electron laser (FLASH) and a new EBIT along with the pump probe x-ray laser experiments are hopeful to provide experimental data for the transitions with short lifetimes in so far inaccessible energy ranges. We believe that our calculations will support such future experiments for transitions with different frequencies and lifetimes.

References

[1] E. Träbert et al., Astrophys. J. 541 (2000) 506.
[2] G. Brenner et al., Astrophys. J. 703 (2009) 68.
[3] E. Träbert, G. Saathoff and A Wolf, J. Phys. B 37 (2004) 945.
[4] D. P. Moehs and D. A. Church, Astrophys. J. 516 (1999) L111.
[5] M. Bilal, A. V. Volotka, R. Beerwerth, S. Fritzsche, submitted to Phys. Rev. A (2018).

Elliptical dichroism in non-linear ionization of atoms

J. Hofbrucker[1,2]*, A. V. Volotka*[1]*, S. Fritzsche*[1,2]

[1] Helmholtz Institute Jena [2]Friedrich-Schiller Universität Jena

Dichroic behavior is usually associated with an interaction of polarized atomic or chiral molecular target and circularly polarized light. Since the observations of asymmetries in above-threshold ionization of nobel gases by elliptically polarized light [1], it became apparent that a dichroic behavior is not a unique characteristic of a chiral target, but can also arise from a non-linear light-matter interaction. In contrast to circular dichroism, it arises from the interference of the dominant ionization channels. It is solely the interference between the different ionization channels which carries the information about the sign of the elliptical polarization. Since the elliptical dichroism is system specific, it gives us an opportunity to study many-electron effects as well as fundamentals of non-linear light-matter interaction.

In our recent work, we studied the intriguing phenomenon of elliptical dichroism in two-photon ionization of a *K*-shell electron of neutral atoms by elliptically polarized light [2, 3]. It was found that a strong effect can be found at threshold energies for two-photon ionization of light elements. However, for inner-shell ionization, high energy photons are required, but the polarization control at current free-electron laser facilities is scarce. In cooperation with our experimental colleagues from the European XFEL project, we decided to find an experimental system for verification of inner-shell elliptical dichroism within the limits of current technologies (proposal 20174073 at FERMI). Out of rare gas atoms, electrons from the krypton *3p* shell were chosen as the most convenient showcase to detect a strong two-photon ionization elliptical dichroism (see Figure 1). Since the cross section for a direct two-photon ionization of Kr *3p* is relatively low and two-photon absorption requires comparably long acquisition times for obtaining statistically valid spectra, we proposed to study the elliptical dichroism in the vicinity of the Kr *3p-3d* resonance in order to facilitate the feasibility of the experiment. The photoelectron spectra will be measured for five photon energies, covering the dynamical energy dependence of the elliptical dichroism, including measurements of both strong and zero dichroism. The proposed experiment of two-photon ionization of Kr will be the first confirmation of elliptical dichroism in inner-shell ionization and it will give us the opportunity to accurately extract atomic parameters relevant for the ionization process.

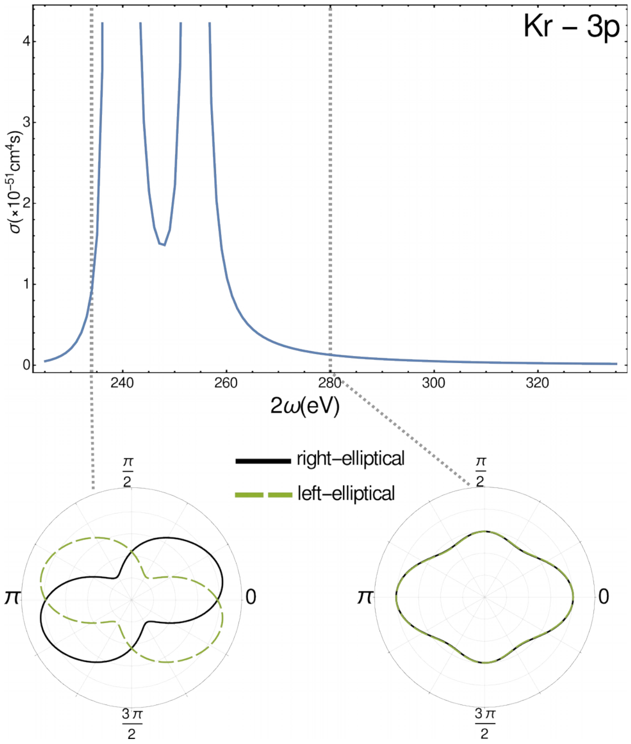

Figure 1: (Upper): Total two-photon cross section in the range of the Kr *3p-3d* resonance as a function of two-photon energy (energy transferred to the initially bound electron). (Lower): Electron distributions in the plane perpendicular to the photon propagation (dipole plane) are shown for two energy points. These distributions represent the maximal and minimal elliptical dichroism for the two-photon ionization of Kr *3p*. From the figures, it is apparent that the dichroism is highly sensitive to the photon (or photoelectron) energy. It is worth noting that the resonance itself only plays a secondary role in the process.

References

[1] M. Bashkansky, P. H. Bucksbaum, and D. W. Schumacher, Phys. Rev. Lett. 60, 2458 (1988).

[2] J. Hofbrucker, A. V. Volotka, and S. Fritzsche, Phys. Rev. A 94, 063412 (2016).

[3] J. Hofbrucker, A. V. Volotka, and S. Fritzsche, Phys. Rev. A 96, 013409 (2017).

Also part of the GSI Scientific Report 2017 / GSI Report 2018-1

Publications

D. Adolph, M. Moller, J. Bierbach, M. Schwab, A. Savert, M. Yeung, A.M. Sayler, M. Zepf, M.C. Kaluza, G.G. Paulus
Real-time, single-shot, carrier-envelope-phase measurement of a multi-terawatt laser
Applied Physics Letters **110**, 081105 (2017).

V.A. Agababaev, A.M. Volchkova, A.S. Varentsova, D.A. Glazov, A.V. Volotka, V.M. Shabaev, G. Plunien
Quadratic Zeeman effect in boronlike argon
Nuclear Instruments & Methods in Physics Research Section B-Beam Interactions with Materials and Atoms **408**, 70 (2017).

V. Bagnoud, J. Hornung, T. Schlegel, B. Zielbauer, C. Brabetz, M. Roth, P. Hilz, M. Haug, J. Schreiber, F. Wagner
Studying the Dynamics of Relativistic Laser-Plasma Interaction on Thin Foils by Means of Fourier-Transform Spectral Interferometry
Physical Review Letters **118**, 255003 (2017).

R. Beerwerth, S. Fritzsche
MCDF calculations of Auger cascade processes
European Physical Journal D **71**, 253 (2017).

M. Bilal, R. Beerwerth, A.V. Volotka, S. Fritzsche
Ab initio calculations of energy levels, transition rates and lifetimes in Ni XII
Monthly Notices of the Royal Astronomical Society **469**, 4620 (2017).

B. Boning, W. Paufler, S. Fritzsche
Attosecond streaking with twisted X waves and intense infrared pulses
Physical Review A **96**, 043423 (2017).

S.S. Bulanov, S.V. Bulanov, T.Z. Esirkepov, M. Kando, S. Rykovanov, F. Pegoraro, C.B. Schroeder, E. Esarey, W.P. Leemans
Strong Field Electrodynamics of a Thin Foil
AIP Conference Proceedings **1812**, 090001 (2017).

S.S. Bulanov, D. Seipt, T. Heinzl, M. Marklund
Depletion of Intense Fields
AIP Conference Proceedings **1812**, 100006 (2017).

J. Buldt, M. Muller, R. Klas, T. Eidam, J. Limpert, A. Tunnermann
Temporal contrast enhancement of energetic laser pulses by filtered self-phase-modulation-broadened spectra
Optics Letters **42**, 3761 (2017).

W. Cayzac, A. Frank, A. Ortner, V. Bagnoud, M.M. Basko, S. Bedacht, C. Blaser, A. Blazevic, S. Busold, O. Deppert, J. Ding, M. Ehret, P. Fiala, S. Frydrych, D.O. Gericke, L. Hallo, J. Helfrich, D. Jahn, E. Kjartansson, A. Knetsch, D. Kraus, G. Malka, N.W. Neumann, K. Pepitone, D. Pepler, S. Sander, G. Schaumann, T. Schlegel, N. Schroeter, D. Schumacher, M. Seibert, A. Tauschwitz, J. Vorberger, F. Wagner, S. Weih, Y. Zobus, M. Roth
Experimental discrimination of ion stopping models near the Bragg peak in highly ionized matter
Nature Communications **8**, 15693 (2017).

M. Chemnitz, M. Gebhardt, C. Gaida, F. Stutzki, J. Kobelke, J. Limpert, A. Tunnermann, M.A. Schmidt
Hybrid soliton dynamics in liquid-core fibres
Nature Communications **8**, 42 (2017).

L. Deak, L. Bottyan, T. Fulop, D.G. Merkel, D.L. Nagy, S. Sajti, K.S. Schulze, H. Spiering, I. Uschmann, H.C. Wille
Realizing total reciprocity violation in the phase for photon scattering
Scientific Reports **7**, 43114 (2017).

J. Deprince, S. Fritzsche, T.R. Kallman, P. Palmeri, P. Quinet
Influence of plasma environment on K-line emission in highly ionized iron atoms evaluated using a Debye-Huckel model
Canadian Journal of Physics **95**, 858 (2017).

J. Deprince, S. Fritzsche, T. Kallman, P. Palmeri, P. Quinet
Plasma Effects On Atomic Data For The K-Vacancy States Of Highly Charged Iron Ions
AIP Conference Proceedings **1811**, 040002 (2017).

M. Fernandes, R. Geithner, J. Golm, R. Neubert, M. Schwickert, T. Stohlker, J. Tan, C.P. Welsch
Non-perturbative measurement of low-intensity charged particle beams
Superconductor Science & Technology **30**, 015001 (2017).

R. Ferrer, A. Barzakh, B. Bastin, R. Beerwerth, M. Block, P. Creemers, H. Grawe, R. de Groote, P. Delahaye, X. Flechard, S. Franchoo, S. Fritzsche, L.P. Gaffney, L. Ghys, W. Gins, C. Granados, R. Heinke, L. Hijazi, M. Huyse, T. Kron, Y. Kudryavtsev, M. Laatiaoui, N. Lecesne, M. Loiselet, F. Lutton, I.D. Moore, Y. Martinez, E. Mogilevskiy, P. Naubereit, J. Piot, S. Raeder, S. Rothe, H. Savajols, S. Sels, V. Sonnenschein, J.C. Thomas, E. Traykov, C. Van Beveren, P. Van den Bergh, P. Van Duppen, K. Wendt, A. Zadvornaya
Towards high-resolution laser ionization spectroscopy of the heaviest elements in supersonic gas jet expansion
Nature Communications **8**, 14520 (2017).

P. Finetti, H. Hoppner, E. Allaria, C. Callegari, F. Capotondi, P. Cinquegrana, M. Coreno, R. Cucini, M.B. Danailov, A. Demidovich, G. De Ninno, M. Di Fraia, R. Feifel, E. Ferrari, L. Frohlich, D. Gauthier, T. Golz, C. Grazioli, Y. Kai, G. Kurdi, N. Mahne, M. Manfredda, N. Medvedev, I.P. Nikolov, E. Pedersoli, G. Penco, O. Plekan, M.J. Prandolini, K.C. Prince, L. Raimondi, P. Rebernik, R. Riedel, E. Roussel, P. Sigalotti, R. Squibb, N. Stojanovic, S. Stranges, C. Svetina, T. Tanikawa, U. Teubner, V. Tkachenko, S. Toleikis, M. Zangrando, B. Ziaja, F. Tavella, L. Giannessi
Pulse Duration of Seeded Free-Electron Lasers
Physical Review X **7**, 021043 (2017).

S. Fuchs, M. Wusnsche, J. Nathanael, J.J. Abel, C. Rodel, J. Biedermann, J. Reinhard, U. Hubner, G.G. Paulus
Optical coherence tomography with nanoscale axial resolution using a laser-driven high-harmonic source
Optica **4**, 903 (2017).

C. Gaida, M. Gebhardt, F. Stutzki, C. Jauregui, J. Limpert, A. Tunnermann
Towards sub-100 fs multi-GW pulses directly emitted from a Thulium-doped fiber CPA system
Proceedings of SPIE **10083**, 100830C (2017).

S.N. Galyamin, A.V. Tyukhtin, A.A. Peshkov
Transition radiation at the boundary of a chiral isotropic medium
Physical Review E **95**, 032142 (2017).

M. Gebhardt, C. Gaida, T. Heuermann, F. Stutzki, C. Jauregui, J. Antonio-Lopez, A. Schulzgen, R. Amezcua-Correa, J. Limpert, A. Tunnermann
Nonlinear pulse compression to 43 W GW-class few-cycle pulses at 2μm wavelength
Optics Letters **42**, 4179 (2017).

M. Gebhardt, C. Gaida, F. Stutzki, S. Hadrich, C. Jauregui, J. Limpert, A. Tunnermann
High average power nonlinear compression to 4 GW, sub-50 fs pulses at 2μm wavelength
Optics Letters **42**, 747 (2017).

M. Gebhardt, C. Gaida, F. Stutzki, S. Hadrich, C. Jauregui, J. Limpert, A. Tunnermann
High-average power, 4 GW pulses with sub-8 optical cycles from a Tm-doped fiber laser driven nonlinear pulse compression stage
Proceedings of SPIE **10083**, 100830B (2017).

H. Gies, F. Karbstein
An addendum to the Heisenberg-Euler effective action beyond one loop
Journal of High Energy Physics **3**, 108 (2017).

H. Gies, R. Sondenheimer, M. Warschinke
Impact of generalized Yukawa interactions on the lower Higgs-mass bound
European Physical Journal C **77**, 743 (2017).

H. Gies, G. Torgrimsson
Critical Schwinger pair production. II. Universality in the deeply critical regime
Physical Review D **95**, 025003 (2017).

H. Gies, L. Zambelli
Non-Abelian Higgs models: Paving the way for asymptotic freedom
Physical Review D **96**, 016001 (2017).

J.S.M. Ginges, A.V. Volotka, S. Fritzsche
Ground-state hyperfine splitting for Rb, Cs, Fr, Ba$^+$, and Ra$^+$
Physical Review A **96**, 062502 (2017).

D.A. Glazov, A.V. Malyshev, A.V. Volotka, V.M. Shabaev, I.I. Tupitsyn, G. Plunien
Higher-order perturbative relativistic calculations for few-electron atoms and ions
Nuclear Instruments & Methods in Physics Research Section B-Beam Interactions with Materials and Atoms **408**, 46 (2017).

B. Goswami, B. Antony, S. Fritzsche
Electron impact scattering and calculated ionization cross sections for SFx (x=1-5) radicals
International Journal of Mass Spectrometry **417**, 8 (2017).

C. Granados, P. Creemers, R. Ferrer, L.P. Gaffney, W. Gins, R. de Groote, M. Huyse, Y. Kudryavtsev, Y. Martinez, S. Raeder, S. Sels, C. Van Beveren, P. Van den Bergh, P. Van Duppen, K. Wrzosek-Lipska, A. Zadvornaya, A.E. Barzakh, B. Bastin, P. Delahaye, L. Hijazi, N. Lecesne, F. Luton, J. Piot, H. Savajols, J.C. Thomas, E. Traykov, R. Beerwerth, S. Fritzsche, M. Block, X. Flechard, S. Franchoo, L. Ghys, H. Grawe, R. Heinke, T. Kron, P. Naubereit, K. Wendt, M. Laatiaoui, I. Moore, V. Sonnenschein, M. Loiselet, E. Mogilevskiy, S. Rothe
In-gas laser ionization and spectroscopy of actinium isotopes near the N = 126 closed shell
Physical Review C **96**, 054331 (2017).

A. Gumberidze, C. Kozhuharov, R.T. Zhang, S. Trotsenko, Y.S. Kozhedub, R.D. DuBois, H.F. Beyer, K.H. Blumenhagen, C. Brandau, A. Brauning-Demian, W. Chen, O. Forstner, B. Gao, T. Gassner, R.E. Grisenti, S. Hagmann, P.M. Hillenbrand, P. Indelicato, A. Kumar, M. Lestinsky, Y.A. Litvinov, N. Petridis, D. Schury, U. Spillmann, C. Trageser, M. Trassinelli, X. Tu, T. Stohlker
Impact parameter sensitive study of inner-shell atomic processes in the experimental storage ring
Nuclear Instruments & Methods in Physics Research Section B-Beam Interactions with Materials and Atoms **408**, 27 (2017).

M. Gunther, M. Jentschel, A.J. Pollitt, P.G. Thirolf, M. Zepf
Refractive-index measurement of Si at gamma-ray energies up to 2 MeV
Physical Review A **95**, 053864 (2017).

P. Hansinger, P. Topfer, N. Dimitrov, D. Adolph, D. Hoff, T. Rathje, A.M. Sayler, A. Dreischuh, G.G. Paulus
Refractive index dispersion measurement using carrier-envelope phasemeters
New Journal of Physics **19**, 023040 (2017).

S.H. Hendi, B.E. Panah, S. Panahiyan, M. Momennia
Dilatonic black holes in gravity's rainbow with a nonlinear source: the effects of thermal fluctuations
European Physical Journal C **77**, 647 (2017).

S.H. Hendi, B.E. Panah, S. Panahiyan, M. Momennia
Three dimensional magnetic solutions in massive gravity with (non)linear field
Physics Letters B **775**, 251 (2017).

S.H. Hendi, B.E. Panaha, S. Panahiyan, M. Momennia
Magnetic brane solutions in Gauss-Bonnet-Maxwell massive gravity
Physics Letters B **772**, 43 (2017).

M.O. Herdrich, G. Weber, A. Gumberidze, Z.W. Wu, T. Stohlker
Fast calculator for X-ray emission due to Radiative Recombination and Radiative Electron Capture in relativistic heavy-ion atom collisions
Nuclear Instruments & Methods in Physics Research Section B-Beam Interactions with Materials and Atoms **408**, 294 (2017).

J. Hofbrucker, A.V. Volotka, S. Fritzsche
Photoelectron distribution of nonresonant two-photon ionization of neutral atoms
Physical Review A **96**, 013409 (2017).

J. Hofbrucker, A.V. Volotka, S. Fritzsche
Relativistic effects in the non-resonant two-photon K-shell ionization of neutral atoms
Nuclear Instruments & Methods in Physics Research Section B-Beam Interactions with Materials and Atoms **408**, 125 (2017).

D. Hoff, M. Kruger, L. Maisenbacher, G.G. Paulus, P. Hommelhoff, A.M. Sayler
Using the focal phase to control attosecond processes
Journal of Optics **19**, 124007 (2017).

D. Hoff, M. Kruger, L. Maisenbacher, A.M. Sayler, G.G. Paulus, P. Hommelhoff
Tracing the phase of focused broadband laser pulses
Nature Physics **13**, 947 (2017).

A. Hoffmann, C. Egelkamp, D. Winters, T. Kuhl, C. Spielmann
Online Monitoring of Laser-Generated XUV Radiation Spectra by Surface Reflectivity Measurements with Particle Detectors
Applied Sciences-Basel **7**, 70 (2017).

R. Hollinger, Z. Samsonova, D. Gupta, C. Spielmann, R. Roder, L. Trefflich, C. Ronning, D. Kartashov
Enhanced absorption and cavity effects of three-photon pumped ZnO nanowires
Applied Physics Letters **111**, 21306 (2017).

C. Jauregui, M. Muller, M. Kienel, F. Emaury, C.J. Saraceno, J. Limpert, U. Keller, A. Tunnermann
Optimizing the noise characteristics of high-power fiber laser systems
Proceedings of SPIE **10083**, 100830W (2017).

C. Jauregui, H.J. Otto, C. Stihler, J. Limpert, A. Tunnermann
The impact of core co-dopants on the mode instability threshold of high-power fiber laser systems
Proceedings of SPIE **10083**, 100830N (2017).

M. Kahle, J. Korner, J. Hein, M.C. Kaluza
Performance of a quantum defect minimized disk laser based on cryogenically cooled Yb:CaF$_2$
Optics and Laser Technology **92**, 19 (2017).

F. Karbstein
Heisenberg-Euler effective action in slowly varying electric field inhomogeneities of Lorentzian shape
Physical Review D **95**, 076015 (2017).

F. Karbstein
Photon propagation in slowly varying electromagnetic fields
Russian Physics Journal **59**, 1761 (2017).

F. Karbstein
Tadpole diagrams in constant electromagnetic fields
Journal of High Energy Physics **10**, 075 (2017).

F. Karbstein, E.A. Mosman
Photon polarization tensor in pulsed Hermite- and Laguerre-Gaussian beams
Physical Review D **96**, 116004 (2017).

M.F. Kasim, L. Ceurvorst, N. Ratan, J. Sadler, N. Chen, A. Savert, R. Trines, R. Bingham, P.N. Burrows, M.C. Kaluza, P. Norreys
Quantitative shadowgraphy and proton radiography for large intensity modulations
Physical Review E **95**, 023306 (2017).

S. Keppler, I. Tamer, M. Hornung, J. Korner, H. Liebetrau, J. Hein, M.C. Kaluza
Pump-induced phase aberrations in Yb^{3+}-doped materials
Proceedings od SPIE **10238**, 102380N (2017).

D. Khaghani, M. Lobet, B. Borm, L. Burr, F. Gartner, L. Gremillet, L. Movsesyan, O. Rosmej, M.E. Toimil-Molares, F. Wagner, P. Neumayer
Enhancing laser-driven proton acceleration by using micro-pillar arrays at high drive energy
Scientific Reports **7**, 11366 (2017).

J. Korner, J. Reiter, T. Luhder, J. Hein, V. Jambunathan, A. Lucianetti, T. Mocek, M.C. Kaluza
Temperature dependent spectroscopic characterization of Tm:YAG crystals as potential laser medium for pulsed high energy laser amplifiers
Proceedings of SPIE **10238**, 102380M (2017).

M. Kozak, P. Beck, H. Deng, J. McNeur, N. Schonenberger, C. Gaida, F. Stutzki, M. Gebhardt, J. Limpert, A. Ruehl, I. Hartl, O. Solgaard, J.S. Harris, R.L. Byer, P. Hommelhoff
Acceleration of sub-relativistic electrons with an evanescent optical wave at a planar interface
Optics Express **25**, 19195 (2017).

Y.S. Kozhedub, A.I. Bondarev, X. Cai, A. Gumberidze, S. Hagmann, C. Kozhuharov, I.A. Maltsev, G. Plunien, V.M. Shabaev, C. Shao, T. Stohlker, I.I. Tupitsyn, B. Yang, D. Yu
Intensities of K-X-ray satellite and hypersatellite target radiation in Bi^{83+}-Xe @70 MeV/u collisions
Nuclear Instruments & Methods in Physics Research Section B-Beam Interactions with Materials and Atoms **408**, 31 (2017).

M. Kubel, Z. Dube, A.Y. Naumov, M. Spanner, G.G. Paulus, M.F. Kling, D.M. Villeneuve, P.B. Corkum, A. Staudte
Streak Camera for Strong-Field Ionization
Physical Review Letters **119**, 183201 (2017).

C. Leithold, J. Reislohner, H. Gies, A.N. Pfeiffer
Characterization of two ultrashort laser pulses using interferometric imaging of self-diffraction
Optics Letters **42**, 5246 (2017).

H. Liebetrau, M. Hornung, S. Keppler, M. Hellwing, A. Kessler, F. Schorcht, J. Hein, M.C. Kaluza
Intracavity stretcher for chirped- pulse amplification in high-power laser systems
Optics Letters **42**, 326 (2017).

I.A. Maltsev, V.M. Shabaev, I.I. Tupitsyn, Y.S. Kozhedub, G. Plunien, T. Stohlker
Pair production in low-energy collisions of uranium nuclei beyond the monopole approximation
Nuclear Instruments & Methods in Physics Research Section B-Beam Interactions with Materials and Atoms **408**, 97 (2017).

A.V. Malyshev, D.A. Glazov, A.V. Volotka, Tupitsyn, II, V.M. Shabaev, G. Plunien
Binding energies of the $1s^2 2s^2 2p_j$ states in boronlike argon
Nuclear Instruments & Methods in Physics Research Section B-Beam Interactions with Materials and Atoms **408**, 103 (2017).

A.V. Malyshev, D.A. Glazov, A.V. Volotka, Tupitsyn, II, V.M. Shabaev, G. Plunien, T. Stohlker
Ground-state ionization energies of boronlike ions
Physical Review A **96**, 022512 (2017).

K. Mecseki, H.T. Olgun, M. Windeler, M. Schulz, R. Riedel, F. Tavella, M.J. Prandolini
Investigation of the critical parameters for CEP stabilized high power 1.5 μm OPCPA
Proceedings of SPIE **10082**, 100821C (2017).

A.J. Miller, K. Minamisono, D.M. Rossi, R. Beerwerth, B.A. Brown, S. Fritzsche, D. Garand, A. Klose, Y. Liu, B. Maass, P.F. Mantica, P. Muller, W. Nortershauser, M.R. Pearson, C. Sumithrarachchi
First determination of ground state electromagnetic moments of ^{53}Fe
Physical Review C **96**, 054314 (2017).

M. Mueller, M. Kienel, A. Klenke, T. Gottschall, E. Shestaev, M. Plotner, J. Limpert, A. Tunnermann

12 mJ pulse energy 8-channel divided-pulse spatio-temporally combined ultrafast fiber-laser system

Proceedings of SPIE **10083**, 1008302 (2017).

M. Muller, A. Klenke, T. Gottschall, R. Klas, C. Rothhardt, S. Demmler, J. Rothhardt, J. Limpert, A. Tunnermann

High-average-power femtosecond laser at 258 nm

Optics Letters **42**, 2826 (2017).

R.A. Muller, A.V. Volotka, S. Fritzsche, A. Surzhykov

Theoretical analysis of the electron bridge process in ^{229}Th^{3+}

Nuclear Instruments & Methods in Physics Research Section B-Beam Interactions with Materials and Atoms **408**, 84 (2017).

T. Nousch, A. Otto, D. Seipt, B. Kampfer, A.I. Titov, D. Blaschke, A.D. Panferov, S.A. Smolyansky

Laser Assisted Breit-Wheeler and Schwinger Processes

in "New Horizons in Fundamental Physics", eds. S. Schramm and M. Schafer **Springer**, 253-262 (2017).

A.A. Peshkov, D. Seipt, A. Surzhykov, S. Fritzsche,

Photoexcitation of atoms by Laguerre-Gaussian beams

Physical Review A **96**, 023407 (2017).

J. Rothhardt, S. Hadrich, J.C. Delagnes, E. Cormier, J. Limpert

High Average Power Near-Infrared Few-Cycle Lasers

Laser & Photonics Reviews **11**, 1700043 (2017).

G.M. Samarin, M. Zepf, G. Sarri

Radiation reaction studies in an all-optical set-up: experimental limitations

Journal of Modern Optics **64**, 2281 (2017).

Z. Samsonova, S. Hofer, A. Hoffmann, B. Landgraf, M. Zurch, I. Uschmann, D. Khaghani, O. Rosmej, P. Neumayer, R. Roder, L. Trefflich, C. Ronning, E. Forster, C. Spielmann, D. Kartashov

X-Ray Emission Generated By Laser-Produced Plasmas From Dielectric Nanostructured Targets

AIP Conference Proceedings **1811**, 180001 (2017).

R. Sanchez, M. Lochmann, R. Johren, Z. Andelkovic, D. Anielski, B. Botermann, M. Bussmann, A. Dax, N. Frommgen, C. Geppert, M. Hammen, V. Hannen, T. Kuhl, Y.A. Litvinov, R. Lopez-Coto, T. Stohlker, R.C. Thompson, J. Vollbrecht, W. Wen, C. Weinheimer, E. Will, D. Winters, W. Nortershauser

Laser spectroscopy measurement of the $2s$-hyperfine splitting in lithium-like bismuth

Journal of Physics B-Atomic Molecular and Optical Physics **50**, 085004 (2017).

G. Sarri, J. Warwick, W. Schumaker, K. Poder, J. Cole, D. Doria, T. Dzelzainis, K. Krushelnick, S. Kuschel, S.P.D. Mangles, Z. Najmudin, L. Romagnani, G.M. Samarin, D. Symes, A.G.R. Thomas, M. Yeung, M. Zepf
Spectral and spatial characterisation of laser-driven positron beams
Plasma Physics and Controlled Fusion **59**, 014015 (2017).

T. Saule, S. Holzberger, O. De Vries, M. Plotner, J. Limpert, A. Tunnermann, I. Pupeza
Phase-stable, multi-μJ femtosecond pulses from a repetition-rate tunable Ti:Sa-oscillator-seeded Yb-fiber amplifier
Applied Physics B-Lasers and Optics **123**, 17 (2017).

V.A. Schanz, F. Wagner, M. Roth, V. Bagnoud
Noise reduction in third order cross-correlation by angle optimization of the interacting beams
Optics Express **25**, 9252 (2017).

S. Schippers, M. Martins, R. Beerwerth, S. Bari, K. Holste, K. Schubert, J. Viefhaus, D.W. Savin, S. Fritzsche, A. Muller
Near L-edge Single and Multiple Photoionization of Singly Charged Iron Ions
Astrophysical Journal **849**, 5 (2017).

C. Scullion, D. Doria, L. Romagnani, A. Sgattoni, K. Naughton, D.R. Symes, P. McKenna, A. Macchi, M. Zepf, S. Kar, M. Borghesi
Polarization Dependence of Bulk Ion Acceleration from Ultrathin Foils Irradiated by High-Intensity Ultrashort Laser Pulses
Physical Review Letters **119**, 054801 (2017).

D. Seipt, T. Heinzl, M. Marklund, S.S. Bulanov
Depletion of Intense Fields
Physical Review Letters **118**, 154803 (2017).

L. Senje, M. Coughlan, D. Jung, M. Taylor, G. Nersisyan, D. Riley, C.L.S. Lewis, O. Lundh, C.G. Wahlstrom, M. Zepf, B. Dromey
Experimental investigation of picosecond dynamics following interactions between laser accelerated protons and water
Applied Physics Letters **10**, 104102 (2017).

F. Siek, S. Neb, P. Bartz, M. Hensen, C. Struber, S. Fiechter, M. Torrent-Sucarrat, V.M. Silkin, E.E. Krasovskii, N.M. Kabachnik, S. Fritzsche, R.D. Muino, P.M. Echenique, A.K. Kazansky, N. Muller, W. Pfeiffer, U. Heinzmann
Angular momentum-induced delays in solid-state photoemission enhanced by intra-atomic interactions
Science **357**, 1274 (2017).

R. Sollapur, D. Kartashov, M. Zurch, A. Hoffmann, T. Grigorova, G. Sauer, A. Hartung, A. Schwuchow, J. Bierlich, J. Kobelke, M. Chemnitz, M.A. Schmidt, C. Spielmann
Resonance-enhanced multi-octave supercontinuum generation in antiresonant hollow-core fibers
Light-Science & Applications **6**, e17124 (2017).

H. Stark, M. Muller, M. Kienel, A. Klenke, J. Limpert, A. Tunnermann
Divided-pulse amplification with fiber-coupled electro-optic modulators
Proceedings of SPIE **10083**, 1008308 (2017).

H. Stark, M. Muller, M. Kienel, A. Klenke, J. Limpert, A. Tunnermann
Electro-optically controlled divided-pulse amplification
Optics Express **25**, 13494 (2017).

C. Stihler, C. Jauregui, H.J. Otto, J. Limpert, A. Tunnermann
Controlling mode instabilities at 628 W average output power in an Yb-doped rod-type fiber amplifier by active modulation of the pump power
Proceedings of SPIE **10083**, 100830P (2017).

C. Stihler, H.J. Otto, C. Jauregui, J. Limpert, A. Tunnermann
Experimental investigation of transverse mode instabilities in a double-pass Yb-doped rod-type fiber amplifier
Proceedings of SPIE **10083**, 100830R (2017).

S. Stock, R. Beerwerth, S. Fritzsche
Auger cascades in resonantly excited neon
Physical Review A **95**, 053407 (2017).

F. Stutzki, C. Gaida, M. Gebhardt, C. Jauregui, J. Limpert, A. Tunnermann, I. Pupeza
Self-protecting nonlinear compression in a solid fiber for long-term stable ultrafast lasers at 2μm wavelength
Proceedings of SPIE **10083**, 100830D (2017).

J. Thomas, M.M. Guenther, A. Pukhov
Beam load structures in a basic relativistic interaction model
Physics of Plasmas **24**, 013101 (2017).

J. Ullmann, Z. Andelkovic, C. Brandau, A. Dax, W. Geithner, C. Geppert, C. Gorges, M. Hammen, V. Hannen, S. Kaufmann, K. Konig, Y.A. Litvinov, M. Lochmann, B. Maass, J. Meisner, T. Murbock, R. Sanchez, M. Schmidt, S. Schmidt, M. Steck, T. Stohlker, R.C. Thompson, C. Trageser, J. Vollbrecht, C. Weinheimer, W. Nortershauser
High precision hyperfine measurements in Bismuth challenge bound-state strong-field QED
Nature Communications **8**, 15484 (2017).

A.S. Varentsova, V.A. Agababaev, A.M. Volchkova, D.A. Glazov, A.V. Volotka, V.M. Shabaev, G. Plunien
Third-order Zeeman effect in highly charged ions
Nuclear Instruments & Methods in Physics Research Section B-Beam Interactions with Materials and Atoms **408**, 80 (2017).

M. Vockert, G. Weber, U. Spillmann, T. Krings, M.O. Herdrich, T. Stohlker
Commissioning of a Si(Li) Compton polarimeter with improved energy resolution
Nuclear Instruments & Methods in Physics Research Section B-Beam Interactions with Materials and Atoms **408**, 313 (2017).

A.M. Volchkova, A.S. Varentsova, N.A. Zubova, V.A. Agababaev, D.A. Glazov, A.V. Volotka, V.M. Shabaev, G. Plunien
Nuclear magnetic shielding in boronlike ions
Nuclear Instruments & Methods in Physics Research Section B-Beam Interactions with Materials and Atoms **408**, 89 (2017).

F. Wagner, J. Hornung, C. Schmidt, M. Eckhardt, M. Roth, T. Stohlker, V. Bagnoud
Backreflection diagnostics for ultra-intense laser plasma experiments based on frequency resolved optical gating
Review of Scientific Instruments **88**, 023503 (2017).

P.A. Walker, P.D. Alesini, A.S. Alexandrova, M.P. Anania, N.E. Andreev, I. Andriyash, A. Aschikhin, R.W. Assmann, T. Audet, A. Bacci, I.F. Barna, A. Beaton, A. Beck, A. Beluze, A. Bernhard, S. Bielawski, F.G. Bisesto, J. Boedewadt, F. Brandi, O. Bringer, R. Brinkmann, E. Brundermann, M. Buscher, M. Bussmann, G.C. Bussolino, A. Chance, J.C. Chanteloup, M. Chen, E. Chiadroni, A. Cianchi, J. Clarke, J. Cole, M.E. Couprie, M. Croia, B. Cros, J. Dale, G. Dattoli, N. Delerue, O. Delferriere, P. Delinikolas, J. Dias, U. Dorda, K. Ertel, A.F. Pousa, M. Ferrario, F. Filippi, J. Fils, R. Fiorito, R.A. Fonseca, M. Galimberti, A. Gallo, D. Garzella, P. Gastinel, D. Giove, A. Giribono, L.A. Gizzi, F.J. Gurner, A.F. Habib, L.C. Haefner, T. Heinemann, B. Hidding, B.J. Holzer, S.M. Hooker, T. Hosokai, A. Irman, D.A. Jaroszynski, S. Jaster-Merz, C. Joshi, M.C. Kaluza, M. Kando, O.S. Karger, S. Karsch, E. Khazanov, D. Khikhlukha, A. Knetsch, D. Kocon, P. Koester, O. Kononenko, G. Korn, I. Kostyukov, L. Labate, C. Lechner, W.P. Leemans, A. Lehrach, F.Y. Li, X. Li, V. Libov, A. Lifschitz, V. Litvinenko, W. Lu, A.R. Maier, V. Malka, G.G. Manahan, S.P.D. Mangles, B. Marchetti, A. Marocchino, A.M. De la Ossa, J.L. Martins, F. Massimo, F. Mathieu, G. Maynard, T.J. Mehrling, A.Y. Molodozhentsev, A. Mosnier, A. Mostacci, A.S. Mueller, Z. Najmudin, P.A.P. Nghiem, F. Nguyen, P. Niknejadi, J. Osterhoff, D. Papadopoulos, B. Patrizi, R. Pattathil, V. Petrillo, M.A. Pocsai, K. Poder, R. Pompili, L. Pribyl, D. Pugacheva, S. Romeo, A.R. Rossi, E. Roussel, A.A. Sahai, P. Scherkl, U. Schramm, C.B. Schroeder, J. Schwindling, J. Scifo, L. Serafini, Z.M. Sheng, L.O. Silva, T. Silva, C. Simon, U. Sinha, A. Specka, M.J.V. Streeter, E.N. Svystun, D. Symes, C. Szwaj, G. Tauscher, A.G.R. Thomas, N. Thompson, G. Toci, P. Tomassini, C. Vaccarezza, M. Vannini, J.M. Vieira, F. Villa, C.G. Wahlstrom, R. Walczak, M.K. Weikum, C.P. Welsch, C. Wiemann, J. Wolfenden, G. Xia, M. Yabashi, L. Yu, J. Zhu, A. Zigler
Horizon 2020 EuPRAXIA design study
Journal of Physics Conference Series **874**, 012029 (2017).

J.W. Wang, C.B. Schroeder, R. Li, M. Zepf, S.G. Rykovanov
Plasma channel undulator excited by high-order laser modes
Scientific Reports **7**, 16884 (2017).

M. Wiesel, G. Birkl, M.S. Ebrahimi, A. Martin, W. Quint, N. Stallkamp, M. Vogel
Optically transparent solid electrodes for precision Penning traps
Review of Scientific Instruments **88**, 123101 (2017).

N. Winckler, A. Rybalchenko, V.P. Shevelko, M. Al-Turany, T. Kollegger, T. Stohlker
BREIT code: Analytical solution of the balance rate equations for charge-state evolutions of heavy-ion beams in matter
Nuclear Instruments & Methods in Physics Research Section B-Beam Interactions with Materials and Atoms **392**, 67 (2017).

D. Wu, X.T. He, W. Yu, S. Fritzsche
Monte Carlo approach to calculate ionization dynamics of hot solid-density plasmas within particle-in-cell simulations
Physical Review E **95**, 023208 (2017).

D. Wu, X.T. He, W. Yu, S. Fritzsche
Monte Carlo approach to calculate proton stopping in warm dense matter within particle-in-cell simulations
Physical Review E **95**, 023207 (2017).

D. Wu, J.W. Wang
Magetostatic amplifier with tunable maximum by twisted-light plasma interactions
Plasma Physics and Controlled Fusion **59**, 095010 (2017).

Z.W. Wu, A.V. Volotka, C.Z. Dong, S. Fritzsche
Dielectronic recombination of highly charged ions with spin-polarized electrons
Nuclear Instruments & Methods in Physics Research Section B-Beam Interactions with Materials and Atoms **408**, 130 (2017).

Z.W. Wu, A.V. Volotka, A. Surzhykov, S. Fritzsche
Angle-resolved x-ray spectroscopic scheme to determine overlapping hyperfine splittings in highly charged heliumlike ions
Physical Review A **96**, 012503 (2017).

M. Wusnsche, S. Fuchs, S. Aull, J. Nathanael, M. Moller, C. Rodel, G.G. Paulus
Quasi-supercontinuum source in the extreme ultraviolet using multiple frequency combs from high-harmonic generation
Optics Express **25**, 6936 (2017).

P. Wustelt, M. Moller, M.S. Schoffler, X.H. Xie, V. Hanus, A.M. Sayler, A. Baltuska, G.G. Paulus, M. Kitzler
Numerical investigation of the sequential-double-ionization dynamics of helium in different few-cycle-laser-field shapes
Physical Review A **95**, 023411 (2017).

J. Xu, A. Buck, S.W. Chou, K. Schmid, B. Shen, T. Tajima, M.C. Kaluza, L. Veisz
Dynamics of electron injection in a laser-wakefield accelerator
Physics of Plasmas **24**, 083106 (2017).

M. Yeung, S. Rykovanov, J. Bierbach, L. Li, E. Eckner, S. Kuschel, A. Woldegeorgis, C. Rodel, A. Savert, G.G. Paulus, M. Coughlan, B. Dromey, M. Zepf
Experimental observation of attosecond control over relativistic electron bunches with two-colour fields
Nature Photonics **11**, 32 (2017).

V.A. Zaytsev, S. Fritzsche, A. Surzhykov, V.M. Shabaev
Hyperfine induced effects on the angular distribution of the dielectronic hypersatellite line
Nuclear Instruments & Methods in Physics Research Section B-Beam Interactions with Materials and Atoms **408**, 93 (2017).

Y.Y. ZHANG, P. KELLNER, D. ADOLPH, D. ZILLE, P. WUSTELT, D. WURZLER, S. SKRUSZEWICZ, M. MOLLER, A.M. SAYLER, G.G. PAULUS

Single-shot, real-time carrier-envelope phase measurement and tagging based on stereographic above-threshold ionization at short-wave infrared wavelengths

Optics Letters **42**, 5150 (2017).

D. ZILLE, D. SEIPT, M. MOLLER, S. FRITZSCHE, S. GRAFE, C. MULLER, G.G. PAULUS

Spin-dependent rescattering in strong-field ionization of helium

Journal of Physics B-Atomic Molecular and Optical Physics **50**, 065001 (2017).

D. ZILLE, D. SEIPT, M. MOLLER, S. FRITZSCHE, G.G. PAULUS, D.B. MILOSEVIC

Spin-dependent quantum theory of high-order above-threshold ionization

Physical Review A **95**, 063408 (2017).

M. ZÜRCH, R. JUNG, C. SPATH, J. TUMMLER, A. GUGGENMOS, D. ATTWOOD, U. KLEINEBERG, H. STIEL, C. SPIELMANN

Transverse Coherence Limited Coherent Diffraction Imaging using a Molybdenum Soft X-ray Laser Pumped at Moderate Pump Energies

Scientific Reports **7**, 5314 (2017).

Theses

A. K. Arunchalam
Investigation of laser-plasma interactions at near-critical densities
Dissertation
Friedrich-Schiller-Universität Jena, Physikalisch-Astronomische Fakultät, (2017).

M. Kienel
Power Scaling of Ultrashort Pulses by Spatial and Temporal Coherent Combining
Dissertation
Friedrich-Schiller-Universität Jena, Physikalisch-Astronomische Fakultät, (2017).

M. Möller
Probing Strong-field Photoionization of Atoms and Diatomic Molecules with Short-wave Infrared Radiation
Dissertation
Friedrich-Schiller-Universität Jena, Physikalisch-Astronomische Fakultät, (2017).

J. Ullmann
Laserspektroskopie an hochgeladenen Bismutionen zum Test der Quantenelektrodynamik
Dissertation
Friedrich-Schiller-Universität Jena, Physikalisch-Astronomische Fakultät, (2017).

Z. Wu
Angular Correlation and Polarization of X-rays Emitted from Highly Charged Ions
Dissertation
Friedrich-Schiller-Universität Jena, Physikalisch-Astronomische Fakultät, (2017).

B. Marx-Glowna
Hochauflösende Röntgenpolarimetrie
Dissertation
Friedrich-Schiller-Universität Jena, Physikalisch-Astronomische Fakultät, (2017).

N. Seegert
Signatures of the quantum vacuum in inhomogeneous electromagentic fields
Dissertation
Friedrich-Schiller-Universität Jena, Physikalisch-Astronomische Fakultät, (2017).

P. Pfäfflein
Entwicklung und Aufbau eines Teilchendetektors für erste Experimente am Ionenspeicherring CRYRING
Master Thesis
Ruprecht-Karls-Universität, Fakultät für Physik und Astronomie, (2017).

S. Stock
Auger cascades in resonantly excited neon
Master Thesis
Friedrich-Schiller-Universität Jena, Physikalisch-Astronomische Fakultät, (2017).